Mechanical & Aerospace Engineering Theses & Dissertations

Mechanical & Aerospace Engineering

Winter 1999

Continuous Adjoint Sensitivity Analysis for Aerodynamic and Acoustic Optimization

Kaveh Ghayour
Old Dominion University

CONTINUOUS ADJOINT SENSITIVITY ANALYSIS FOR AERODYNAMIC AND ACOUSTIC OPTIMIZATION

by
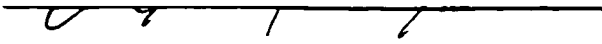
Kaveh Ghayour
MSc. October 1994, BEng. June 1993,
Imperial College of Science and Technology, London, UK.

A Dissertation Submitted to the Faculty of Old
Dominion University in Partial Fulfillment of the
Requirement for the Degree of

DOCTOR OF PHILOSOPHY
AEROSPACE ENGINEERING

Old Dominion University
December 1999

Approved by:

_____

Oktay Baysal (Director)

_____

Ponnampalam Balakumar (Member)

_____

Jeng-Jong Ro (Member)

_____

Manuel D. Salas (Member)

ABSTRACT

CONTINUOUS ADJOINT SENSITIVITY ANALYSIS FOR AERODYNAMIC AND ACOUSTIC OPTIMIZATION

Kaveh Ghayour
Old Dominion University, 1999
Director: Dr. Oktay Baysal
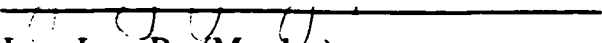
A gradient-based shape optimization methodology based on continuous adjoint sensitivities has been developed for two-dimensional steady Euler equations on unstructured meshes and the unsteady transonic small disturbance equation. The continuous adjoint sensitivities of the Helmholtz equation for acoustic applications have also been derived and discussed.

The highlights of the developments for the steady two-dimensional Euler equations are the generalization of the airfoil surface boundary condition of the adjoint system to allow a proper closure of the Lagrangian functional associated with a general cost functional and the results for an inverse problem with density as the prescribed target. Furthermore, it has been demonstrated that a transformation to the natural coordinate system, in conjunction with the reduction of the governing state equations to the control surface, results in sensitivity integrals that are only a function of the tangential derivatives of the state variables. This approach alleviates the need for directional derivative computations with components along the normal to the control surface, which can render erroneous results.

With regard to the unsteady transonic small disturbance equation (UTSD), the continuous adjoint methodology has been successfully extended to unsteady flows. It has been demonstrated that for periodic airfoil oscillations leading to limit-cycle behavior, the Lagrangian functional can be only closed if the time interval of interest spans one or more periods of the flow oscillations after the limit-cycle has been attained. The steady state and limit-cycle sensitivities are then validated by comparing with the brute-force derivatives. The importance of accounting for the flow circulation sensitivity, appearing in the form of a Dirac delta in the wall boundary condition at the trailing edge, has been stressed and demonstrated. Remarkably, the cost of an unsteady adjoint solution is about 0.2 times that of a UTSD solution.

Unlike the Euler equation sensitivities, the Helmholtz equation requires the Hessian of the acoustic field on the control surface. Obtaining accurate Hessian information on curved surfaces is not an easy task, if not impossible. It is been shown that in the natural coordinates, the only required derivative information are the first and second order tangential derivatives of the acoustic field that can be computed very accurately by fitting the boundary variables with a cubic-spline interpolating function. If it were to be attempted, the sensitivities of the Navier-Stokes equations would also require the Hessian of the state variables. Based on above experiences, it is contended that a transformation to the trihedral coordinate system may ease the problem associated with the acquisition of accurate boundary derivative information.

To my parents,
Mahin and Hossien
and my brothers,
Behzad, Bahman and Babak

ACKNOWLEDGMENTS

I would like to express gratitude and appreciation to my advisor Dr. Oktay Baysal for his invaluable guidance, encouragement, and advice throughout the entire course of this study. I wish to sincerely thank my guidance and dissertation committee members, Dr. Ponnampalam Balakumar, Dr. Jeng-Jong Ro, and Mr. Manuel D. Salas for their valuable time and suggestions.

Special thanks are due to Dr. Ponnampalam Balakumar for many helpful suggestions, discussions, critical comments, and in particular for letting me benefit from his in-depth knowledge of Fluid Dynamics.

I am grateful to all my family members, especially my brother Mr. Babak Ghayour, whose support and encouragement has always been a source of inspiration for me.

Finally, I would like to thank all of my colleagues, especially Mr. Amir S. Kazemi, Dr. Satish Boregoda, Jeyasingham Samarasingham, Ilhan Bayraktar, Jean-Michel Dhainaut, Juan Pelaez, and Bulent Imamoglu for their friendship and support.

Kaveh Ghayour

December 1999

TABLE OF CONTENTS

7   **RESULTS OF SHAPE OPTIMIZATION WITH 2D EULER EQUATIONS**

ON UNSTRUCTURED MESHES FOR GENERAL

COST FUNCTIONALS   **86**

8   **RESULTS OF STEADY AND LIMIT-CYCLE SHAPE OPTIMIZATION**

WITH TRANSONIC SMALL DISTURBANCE EQUATION   **97**

9   **DEMONSTRATION OF HELMHOLTZ EQUATION SENSITIVITIES**

112

LIST OF TABLES

LIST OF FIGURES

LIST OF SYMBOLS

a_0	speed of sound
A	Jacobian of x-flux
$\hat{b}$	unit bi-normal vector
B	Jacobian of y-flux
c	speed of sound
C_p	pressure coefficient
E	total energy
$\bar{F}$	flux vector in the x-direction
$\bar{G}$	flux vector in the y-direction
$\bar{G}_g$	geometric constraints
$\bar{G}_a$	aerodynamic constraints
H	total enthalpy
I	augmented functional
$\hat{i}, \hat{j}, \hat{k}$	unit vectors of Cartesian coordinate system
I_C	objective (cost) functional
I_R	complementary functional
J_0, J_1	Bessel functions of first kind and order 0 and 1
M, M_∞	freestream mach number
$\hat{n}$	unit normal vector
p	pressure
$\bar{q}$	velocity vector
q	speed
$\bar{Q}$	conserved flow variables
R	radius of curvature

$\hat{t}$	unit tangential vector
u^*	fundamental solution
$\bar{V}$	design velocity vector
u, v, w	Cartesian components of velocity
u_s, u_n, u_b	natural coordinate components of velocity
$\bar{x}$	position vector
$\bar{X}_D$	design variables
Y_0, Y_1	Bessel functions of second kind and order 0 and 1

Greek Symbols

δ	Dirac delta function
$\delta\bar{x}$	infinitesimal line element
$\delta\vartheta$	element of volume
$\delta\sigma$	element of surface area
ρ	density
$\bar{\lambda}$	adjoint variables
Ω	flow domain
τ	time-like parameter
μ	torsion
Γ	boundary
κ	curvature
θ	angle with the positive x-direction
ϕ	perturbation potential
ψ	wake adjoint variable

Other Symbols

$\mathfrak{R}$	Flow equations
∂	partial derivative

∇ gradient operator

$\in$ within a set of values

Overlines

$\sim$ approximately

Subscripts

∞ infinity

b component of a vector in bi-normal direction

LE leading edge

n component of a vector in normal direction

s component of a vector in tangential direction

TE trailing edge

Superscripts

$\cdot$ material or total derivative

n time level

$t, \sim$ target quantities

CHAPTER 1

INTRODUCTION[*]

Optimal shape design is an old problem in various scientific disciplines that has attracted the attention of many well-known applied mathematicians and physicists for centuries. Calculus of variations was the early research tool that was used extensively for finding the optimality conditions. However, very few problems allow purely analytical solutions, especially when the physical system under consideration is governed by a set of partial differential equations. Nonlinearity of the equations governing fluid flow and the geometric complexity of the domains on which these equations need to be solved render the task of aerodynamic shape design challenging and complicated. Apart from some oversimplified problems, optimality conditions cannot be found in general with purely analytical approaches and, as such, aerodynamicists have always been seeking for experimental, computational, or even different analytical tools to find solutions to their design or inverse problems.

In the last four decades, the emergence of Computational Fluid Dynamics (CFD) has made it possible to compute complicated flows with no previously known analytical closed form solutions. It has opened up the possibility for developing new hybrid analytical-computational techniques to address the problem of aerodynamic shape

---

[*] The format of this dissertation is based on the *Journal of Fluids Engineering*.

optimization. The researcher starts with defining a mathematical model for the problem in hand and tries to come up with equations for the optimality conditions using analytical techniques. Subsequently, a suitable computational method takes over and solves those equations iteratively, which at times may require numerous solutions of the flow field equations. Hence, it should be realized that the accomplishment of this task requires an efficient and robust computational analysis method that can navigate the design space with minimal interference by the researcher. Furthermore, considering the amazing rate of advancement in the field of CFD, the dependency of the computational method on a particular flow solver should be kept to a minimum to avoid obsolescence.

1.1 A Perspective on Aerodynamic Design Optimization

In all aerodynamic design methods, the ultimate goal is to come up with a shape that improves some desired aerodynamic measure of performance, while abiding with the imposed physical (for present arguments, aerodynamics) and geometrical constraints. As it has already been mentioned, analytical and computational techniques need to be combined to achieve the final goal of design improvement. However, the integration process of the various available tools is not unique and gives rise to different schools of thought in this field. If this task has to be done in an iterative manner, starting from an arbitrary shape, classical gradient-based approaches require knowledge of the value of the functional and its gradient with respect to the design parameters of the problem. Having obtained the functional value and its gradient, one can use various numerical optimization methods, such as, steepest descent, conjugate gradient, GMRES, etc., to move in the design space towards the local optimal point. Success of all gradient-based methods

pivots on the assumption of smoothness for the design space, implying that the gradient and higher order derivatives of the functional exist and are continuous.

Currently, CFD flow solvers are capable of producing highly accurate and reliable solutions to complex aerodynamic problems over complicated geometries and computation of the objective functional with a high degree of accuracy does not pose a major problem. Therefore, bulk of the work in an optimal shape design problem is geared towards obtaining accurate functional gradients with respect to the design variables. Gradients can be computed in two different ways:

(a) *Brute force method.* As the ith component of a gradient vector is merely the partial derivative of the objective functional with respect to that design variable, it can be obtained by means of finite-differencing the flow analysis code. In other words, to obtain an array of perturbed functionals, each design variable is perturbed by an array of small quantities, while all other design variables are kept constant. Subsequently, the partial derivative can be calculated by finite-difference formulas of varying accuracy. For instance, if the design variable is perturbed by ε and $-\varepsilon$ respectively, where ε is sufficiently small, central difference formula yields a value for the partial derivative with an error bound proportional to ε^2 ($O(\varepsilon^2)$). This error bound is valid if one assumes that the perturbed functional values are exact. However, in practice, the CFD flow solution differs from the exact solution due to the truncation error incurred in the discretization process and an additional error arising from the approximate resolution of the discretized equations. A simple error analysis shows that an upper bound for the error in a central difference formula is given by $2\Delta/\varepsilon + O(\varepsilon^2)$; Δ being the difference between the exact solution and the approximate solution obtained from

CFD analysis. For a choice of $\Delta=10^{-5}$ and $\varepsilon=10^{-4}$, the computed partial derivative will not even be accurate to the first decimal place! In other words, smaller step size translates into more accurate derivatives only if $\Delta \to 0$ for an infinitely fine mesh and a resolution scheme with zero tolerance. As Δ is not known *a priori*, it can be easily concluded that a suitable value for the step size ε for obtaining reliable derivatives is highly problem dependent. It has to be mentioned, however, that Newman *et al.* (1998) have developed a new method for computing single and multidisciplinary sensitivity derivatives using complex variables that avoids subtractive cancellation error and is not sensitive to step size selection.

Furthermore, the gradient can be computed within the cost of $2N$ flow analysis for N design variables; the cost of which becomes computationally formidable as the number of design variables are increased.

(b) Adjoint method. In this method, the governing equation and its boundary conditions are introduced as constraints on the optimization problem in such a way that the gradient of the objective functional can be found without resorting to multiple flow solutions. Some arbitrary variables, function of space and time in the most general form, are introduced in the analysis in a manner that an analytical expression for the gradient can be obtained. These arbitrary variables are also known as the *Lagrange multipliers* or *adjoint variables*. Adjoint variables satisfy an adjoint problem that at the continuous level is always a linear differential equation with constant or variable coefficients predetermined from the flow equations. The adjoint equation and its boundary/initial conditions are a function of the flow equations and the objective functional.

This dissertation is mostly concerned with the application of method *(b)* for obtaining reliable and efficient sensitivities of various state equations. Therefore, this method is outlined as follows. An optimization problem can be stated as:

$$\text{Minimize } I_C\left(\vec{Q}, \vec{X}_D\right)$$

Subject to:

$$\vec{\Re}\left(\vec{Q}, \vec{X}_D\right) = 0 \tag{1.1}$$

$$\vec{G}_g\left(\vec{X}_D\right) \leq 0$$

$$\vec{G}_a\left(\vec{Q}, \vec{X}_D\right) \leq 0$$

In Eq. (1.1), I_C is the objective (cost) functional, $\vec{Q}$ is the vector of flow variables, $\vec{X}_D$ is the design variables, and $\vec{\Re}$ is the vector of flow equations and its boundary/initial conditions through which $\vec{Q}$ and $\vec{X}_D$ are implicitly related. $\vec{G}_g$ is the array of geometric constraints, and $\vec{G}_a$ is the vector of aerodynamic constraints. An augmented objective functional is defined as:

$$I\left(\vec{Q}, \vec{X}_D, \vec{\lambda}\right) = I_C\left(\vec{Q}, \vec{X}_D\right) + \vec{\lambda} \cdot \vec{\Re}\left(\vec{Q}, \vec{X}_D\right) \tag{1.2}$$

In Eq. (1.2), $\vec{\lambda}$ is the vector of adjoint variables and the inner product operator is defined as integration over the flow domain. At the optimal condition, the derivative of the augmented cost functional with respect to $\vec{\lambda}$, $\vec{Q}$ and $\vec{X}_D$ must vanish:

$$\vec{\Re} = 0$$

$$\frac{\partial I_C}{\partial \vec{Q}} + \left(\frac{\partial \vec{\Re}}{\partial \vec{Q}}\right)^T \cdot \vec{\lambda} = 0 \tag{1.3a-c}$$

$$\frac{\partial I_C}{\partial \vec{X}_D} + \left(\frac{\partial \vec{\Re}}{\partial \vec{X}_D}\right)^T \cdot \vec{\lambda} = 0$$

For a given $\vec{X}_D$, the governing flow equations can be solved to provide the vector of flow variables, $\vec{Q}$. Inserting the known values of $\vec{X}_D$ and $\vec{Q}$ in Eq. (1.3b), one can solve for the adjoint variables. Eq. (1.3b) is known as the adjoint equation. The total derivative of the cost functional with respect to the design variables, $\vec{X}_D$, is hence given by:

$$\frac{dI_C}{d\vec{X}_D} = \frac{\partial I_C}{\partial \vec{X}_D} + \left(\frac{\partial \vec{\Re}}{\partial \vec{X}_D}\right)^T \cdot \vec{\lambda} \qquad (1.4)$$

Note that at the optimal design point, the RHS of the above equation is zero in agreement with the optimality condition of Eq. (1.3c).

Eqs. (1.3a-c) and (1.4) are the common starting point of *continuous* and *discrete* adjoint sensitivity analysis. By continuous adjoint method, it is implied that the variational method is applied directly to the partial differential equations of the governing state equations resulting in a corresponding set of partial differential equations as the adjoint set. The obtained adjoint system is then discretized and solved numerically. On the other hand, one can start from the discretized equations of state and derive a discrete set of adjoint equations directly. This method is known as the discrete adjoint sensitivity analysis.

Both of these methods have some advantages. The continuous method is more theoretically challenging, while the discrete approach is more systematic. The discrete approach, if applied carefully and correctly, provides derivatives which are consistent with the brute-force method derivatives irrespective of the mesh size, while the continuous derivatives only agree with the finite difference derivatives in the limit when the mesh spacing tends to zero. Continuous adjoint equations are usually very similar to

the governing state equations and the CFD solver can be modified accordingly to be used for resolving the adjoint equations. It is of utmost importance to make sure that the CFD solver module is robust, accurate and possesses a high rate of convergence, as an adjoint solver developed based on the discretization and resolution of the CFD module will possess similar characteristics. In the case of the discrete method, however, adaptation of the CFD module for the solution of the adjoint set is not very straightforward and depends strongly on the flow solution algorithm employed in the CFD module. Furthermore, as the number of mesh points increase, the direct solution of the large sparse system of Eq. (1.3b) becomes more impractical and even resorting to indirect solvers can result in modest improvements. The continuous method can primarily utilize the storage used by the CFD module and in this sense, the continuous method has a great advantage over the discrete approach. Competitive discrete solvers will have to develop the capability of solving the adjoint set with approximately the same computational resources as required for the CFD module.

1.2 Motivation and Objectives

In this research, the method of continuous adjoint sensitivity analysis is applied to a variety of state equations. A cursory glance at the publications on the subject regarding the steady Euler/Navier-Stokes equations on unstructured meshes reveals some shortcomings in the utilized analytical and computational treatments. There are numerous references in the literature to 'admissible' cost functionals, referring to cost functionals solely dependent on the pressure and/or wall shear stress on the control surface. Anderson and Venkatakrishnan (1997), Soemarwoto (1997), Jameson et al.

(1998), and Hiernaux and Essers (1999) report difficulties with the proper closure of the Lagrangian associated with the Euler equations and general functionals. Giles and Pierce (1997) conclude that only certain choices of objective functionals would lead to a well-posed adjoint problem. However, according to the theory of functional analysis adjoint variables exist for any cost functional and Arian and Salas (1997) are the first to find a remedy for this problem for the potential, Euler, and Navier-Stokes equations. They showed that the inclusion of additional terms in the Lagrangian functional, resulting from the restriction of the interior PDE to the control surface, could alleviate the difficulties encountered in the derivation of the boundary conditions for the adjoint problem.

The approach adopted in this research will use the material derivative approach with a subsequent switch to the natural coordinate system. The development is more or less in line with that of Anderson and Venkatakrishnan (1997) with the significant difference being that the method is extended to general objective functions. The extension to general cost functionals for the steady Euler equations is more direct and simpler compared to that discussed in Arian and Salas (1997). Salas and Arian propose an additional system of partial differential equations that need to be solved to obtain the transpiration boundary condition for the adjoint set. However, it can be shown by some lengthy but straightforward algebraic manipulations that the proposed additional system can be simplified to yield the same boundary condition that has been derived in this work for steady Euler equations. Also, the optimization results with density as the integrand of its objective functional are the first published result of its kind to the best of the author's knowledge.

Pironneau (1994) reports dissatisfaction with the accuracy of the sensitivity derivatives obtained by the continuous adjoint method and states that this inaccuracy emanates from the lack of accuracy in the normal derivative information on the control surface. He attributes these errors to the discretization errors of the numerical techniques used to solve the governing and the adjoint system of equations. In this research also, it is pointed out that accurate computation of normal derivatives of state and/or adjoint variables on the design surface is crucial for the calculation of shape design sensitivity information, often expressed as a surface or line integral over the design surface. However, Babuska paradox, as discussed in Strang and Fix (1973), states that when linear segments are used for representing a curved boundary, the solution for normal derivatives to the boundary may not be accurate. This poses a major problem for finite volume discretizations on first order triangular elements as the boundary is indeed represented with piece-wise linear segments. In this work, it will be demonstrated that a transformation to the body-fitted coordinates, s-n, along with the application of the governing state equations on the control surface can be used to eliminate normal derivatives from the sensitivity integrals.

Most of the research work in the field of aerodynamic optimization has been conducted for steady flows and the resulting steady aerodynamic loads. In numerous applications, however, the flow is unsteady, which necessitates the analysis equations to include the time dependent terms. The motivation for research on optimization involving unsteady flows resides in at least three application areas: flow control, aeroelasticity, and shape design. To establish this point, some examples of research in these areas will be given next. Among the objectives for flow control are optimal placement of sensors by

Loncaric (1998), drag reduction in turbulent flows in the works of Bewley and Moin (1994), suppression of boundary layer instability by Joslin *et al.* (1997), and adaptive airfoil to control unsteady flow separation in the experimental work of Chandrasekhara *et al.* (1998). As for the examples in aeroelasticity, there are applications for turbomachinery as in Murthy and Kaza (1991) and Lorence and Hall (1994). Li and Livne (1995) and Kolonay (1996) report results for aeroelastic optimization of wings with analytical sensitivities and approximate methods in supersonic and subsonic wing aerodynamics. Of great interest to this research are the two examples for shape optimization in unsteady, incompressible flows given by Beichang *et al.* (1997). It should be noted that Beichang *et al.* (1997) use the discrete adjoint sensitivity method for their work. In the present work, the continuous adjoint methodology is extended successfully to unsteady flow equations and the limit-cycle sensitivities of the unsteady transonic small-disturbance equation (UTSD) are derived and implemented computationally (Ghayour and Baysal (1999)). It has also been shown that the adjoint equation exists if and only if the time period of concern spans one or more periods of the flow oscillations after the limit cycle has been attained. The demonstrated case designing for the limit-cycle C_N-α distribution is the first of its kind in the current literature on shape optimization.

In the last part of this dissertation, it is intended to obtain the shape sensitivity derivatives of an acoustic pressure field (Ghayour and Baysal (2000)). This problem is not only very interesting mathematically but has practical applications as well, for instance, in the reduction of noise pollution in populated urban areas. Bonnet (1992) has

embarked on addressing a shape identification problem using the boundary integral method and shape differentiation, but the analysis is not conclusive because of the author's mishandling of a non-analytical complex function.

1.3 Organization of the Dissertation

This dissertation is organized in ten chapters. The background, brief description of the methodology, motivations and objectives have been presented in this chapter. Chapter 2 is devoted to literature survey, a detailed review of the research work conducted in the field. Chapter 3 discusses the mathematical tools a researcher needs to be familiar with for the proper implementation of the continuous adjoint methodology. Chapter 4, 5, and 6 include the detailed derivations of the method as applied to the Euler, the UTSD, and the wave equation respectively. Chapter 7, 8, and 9 present the optimization and other relevant results for the above-mentioned class of state equations. Finally, conclusions of the present investigation and recommendations for future enhancement of the work are given in Chapter 10.

Chapter 2

Literature Survey

In this chapter, the current literature on adjoint methods pertaining to the field of fluid dynamics is reviewed and underlying concepts highlighted. In general, adjoint methods have been used extensively in the following areas:

- Shape optimization in aerodynamics and acoustics

- Flow Control

- Error estimation for CFD analysis

- Aeroelasticity

As the primary concern of this dissertation is shape optimization, the survey of the literature found in this particular area has been covered more extensively than the other areas mentioned above. Nevertheless, it is also intended to provide the reader with an informative review of the work conducted in the other areas, where the present method will be the key enabling technology.

2.1 Shape Optimization

In the gradient-based optimization environment, which is the focus of this work, most of the analytical and computational effort is geared towards acquirement of accurate gradient information. The existing literature in aerodynamic optimization draws heavily from the theory of control of systems governed by partial differential equations as outlined by Lions (1971). Marrocco and Pironneau (1978) may be credited for being the

first researcher applying the control theory to the design of an electromagnet. They lay the foundation for *discrete adjoint analysis* by computing the optimality condition of the discretized Maxwell's equation for magnetostatics. Taking advantage of the variational formulation of the full potential equation, Angrand (1983) combines the techniques of optimal control, finite element method, and numerical optimization to solve both for inverse and direct optimization of incompressible and compressible flow in nozzles and around airfoils. He, too, finds the optimality conditions directly from the discretized state equations, referring to the discrete approach as the safe approach.

Jameson (1988) provides a theoretical framework to extend control theory to airfoil and wing design based on the full potential and Euler equations. The control is the shape of the boundary that upon using conformal mapping becomes the mapping function. The problem is solved in the mapped domain, which is stationary, avoiding the complications of moving boundaries in the physical plane. In a later publication, Jameson (1990) applies his theoretical development to the reduction of shock induced pressure drag on airfoils in two-dimensional transonic flow using the full potential equation. Later, Jameson (1994), Reuther and Jameson (1994), Jameson *et al.* (1998) use an alternative formulation, which does not depend on conformal mapping and can be easily extended to treat general configurations in three dimensions. It should be noted that all these investigations are carried out on structured meshes and deal with the so-called *admissible* cost functionals, functionals solely dependent on one flow variable on the control surface, that is, pressure. Pironneau (1994) demonstrates results for drag minimization in Stokes flow and analysis for drag minimization in laminar Navier-Stokes flow. Discouraged by the lack of accuracy of gradients obtained by the continuous

adjoint method, discussed earlier in Chapter 1, Pironneau resorts to the discrete adjoint method and computes the optimality condition of the discretized incompressible potential flow in a duct.

Frank and Shubin (1992) apply the *implicit function theorem* to the discretized equations of a one-dimensional Eulerian duct flow. They also introduce the *all-at-once* method, where the optimization simultaneously varies the flow and design variables and the discretized flow equations are viewed as equality constraints on the optimization.

It is noteworthy that the discrete approach for the computations of sensitivities is also known as the *implicit gradient* method, *discrete sensitivity* analysis, or *quasi-analytical* approach. Elbanna and Carlson (1990) use this method first to optimize airfoil shapes using the transonic small disturbance theory, and later in Elbanna and Carlson (1992) the discrete sensitivities are used for wing optimization in three dimensions using the full potential equation.

Baysal and Eleshaky (1991, 1992) and Baysal *et al.* (1993) apply the discrete method to 2D compressible Euler equations with first and third-order accurate spatial discretizations to design the nozzle and after-body of a hypersonic plane. In these works, the finite-difference, direct differentiation, and the adjoint variable methods have been discussed and the relative merits of each with regard to computational efficiency and accuracy have been explained thoroughly. In a later work of Eleshaky and Baysal (1993), the method has been extended to the thin-layer Navier-Stokes equation to account for viscous effects in the transonic regime. Furthermore, several methods for solving the adjoint system of linear algebraic equations have been discussed and compared with regard to the computational time and storage requirements. Burgreen and Baysal (1994)

use a preconditioned conjugate gradient (PCG)-like method, GMRES, as explained in Saad and Schultz (1986), to reduce the computational time and storage considerably compared to that of a direct inversion technique. In Eleshaky and Baysal (1994a, 1994b) a preconditioned domain decomposition technique is used to compute three-dimensional aerodynamic sensitivities. Automatic differentiation of CFD codes for practical design purposes has also received attention in the recent years (e.g. Baysal *et al.* (1997)).

To mitigate the computer memory and CPU time problem associated with large two- and three-dimensional problems, Pandya and Baysal (1997a) have used the ADI based solution methodology for a large-scale arrow-wing optimization study in inviscid flow. Later in Pandya and Baysal (1997b) the solution method is extended to viscous flows in order to study the effect of viscous terms, mesh size, and various problem formulation strategies on the optimized shape.

Of great importance is the work of Burkardt and Gunzburger (1995) in comparing the relative accuracy of discrete and continuous sensitivities. The relationship between discrete adjoint variable and continuous adjoint variable has been examined and it has been concluded that the continuous sensitivities with respect to the boundary shape are significantly inaccurate. The primary source of the error is reported to lie in the boundary conditions, which are affected by errors in approximate spatial derivatives.

Although the decoupling of the state equation solver from the adjoint module and surface modification routines reduces the programming effort needed to integrate different components of an optimization code, such decoupling may prove to be computationally expensive. Decoupling requires numerous time-consuming fully converged flow and adjoint analyses, which can be avoided by relaxing the state and the

adjoint equations simultaneously. The methods reported by Frank and Shubin (1992), Ta'asan *et al.* (1992), Arian and Ta'asan (1994), Shenoy *et al.* (1997), and Marco and Beux (1993) are examples of the effort geared towards tight coupling of the components of an optimization code. In particular, Kuruvila *et al.* (1994) present an efficient numerical approach for design of optimal aerodynamic shapes with the full potential equation reducing the computational cost of the whole optimization problem to approximately two to three times the cost of the analysis problem. High efficiency in reaching the optimum solution is achieved by using a multigrid technique that updates the shape in a hierarchical manner such that smooth changes are done separately from high frequency changes.

Application of a *fully* continuous adjoint method to the two-dimensional Euler equations on a psuedo-unstructured meshes appears in the work of Beux and Dervieux (1992). The *'concertina mesh'*, used in this work, is a triangular mesh where the abscissae of the nodes are fixed and the ordinates change only for a portion of the domain. By using such a mesh, the complications of mesh adjustment and boundary conformity, essential in the course of an optimization process, are avoided as the mesh parameterization almost relies on *i-j* as in a structrued mesh.

Anderson and Venkatakrishnan (1997) present the very first application of the continuous adjoint approach for obtaining sensitivity derivatives of admissible cost functionals on unstructured grids for Euler/Navier-Stokes equations. With regard to the Navier-Stokes equations, the authors contend that the shape sensitivity derivatives of viscous flows require accurate second order derivatives of the velocity on the control surface. They further argue that consistent second derivatives cannot be obtained with

spatially second-order accurate schemes. They propose that only using a higher order discretization of the flow equations can circumvent this problem which obviously requires a considerable amount of effort. Their solution for alleviating this problem is to essentially abandon the purely continuous adjoint approach in favor of the discrete approach. Consequently, Anderson and Bonhaus (1997) and Neilsen and Anderson (1998), completely shift to the discrete approach. Three-dimensional Euler/Navier-Stokes computations on unstructured grids can also be seen in the works of Elliot and Peraire (1996, 1997).

Coming back to the continuous adjoint approach, a major concern is the requirement of smooth functionals in variational techniques. The presence of a shock in the flowfield causes numerical difficulties; even good shock-capturing schemes with low continuity properties cannot be often combined successfully with efficient optimization methods requiring smooth functionals. Iollo and Salas (1995) split the domain by means of a curve coinciding with the shock and then apply the methodology on each of the sub-domains. The supersonic outlet boundary condition is applied before the shock while subsonic inlet boundary condition is applied after the shock. Cliff *et al.* (1995) introduce the shock location as an explicit variable in the design problem of a duct flow with a shock and prove the existence of optimal solutions, differentiability, and the existence of Lagrange multipliers. Giles and Pierce (1997) show that for the quasi one-dimensional and two-dimensional Euler equations, adjoint variables have a logarithmic singularity at the sonic line in the quasi one-dimensional case, and a weak inverse-square-root singularity at the upstream stagnation streamline in the two-dimensional case. However, the adjoint variables are continuous at shocks in both cases. Their conclusion with regard

to restrictions on the permissible choice of operators in the linearized functionals is not correct as shown in Arian and Salas (1997) and Baysal and Ghayour (1998).

2.2 Flow Control

In this section, it is intended to review the important advances in the field of flow control that has taken place in the past few years. It is of great practical importance to have the ability to manipulate wall-bounded and free shear flows to prevent or provoke separation, delay or advance transition and suppress or enhance turbulence. Gad-el-Hak (1996) presents a thorough survey of the recent developments in the control of turbulent flows spurred by chaos control theory, microfabrication and neural network techniques. In this section, an outline of the theoretical and computational research in this field that has used the adjoint method or optimization techniques is presented.

Bewley and Moin (1994) have utilized the concept of adjoint equations to find optimal wall-normal blowing and suction distribution to efficiently reduce drag in a turbulent channel flow. The cost functional is constructed to represent some balance of the drag integrated over the walls and the net control effort. Subsequently, an adjoint approach is used to find the flow sensitivity to the applied control and the control is updated using a gradient algorithm subsequently. Numerical simulations indicate an approximate 17% drag reduction with small levels of output. A later work of Bewley *et al.* (1997) lays the mathematical framework for the application of the robust control theory, which is a generalization of optimal control theory, to the field of fluid mechanics. The goal of the work is to obtain effective control algorithms that are

insensitive to a broad class of disturbances for a wide variety of infinite-dimensional linear and nonlinear problems in fluid mechanics.

Ravindran (1995) establishes the existence of an optimal state and derives the first-order optimality conditions for optimal control in magneto-hydrodynamics. Ito and Ravindran (1996) present a reduced order method for simulations and control of viscous incompressible flow. The feasibility of the method has been demonstrated with two boundary control problems: velocity tracking in a cavity flow and vorticity control in a channel flow.

Balakumar and Hall (1996) present results for optimum suction distribution resulting in the longest laminar region for a given total suction. The problem is formulated using Lagrange multipliers and the resulting nonlinear system is solved by the Newton-Raphson technique. The computations are performed for a Blasius boundary layer on a flat plate and cross-flow cases. It is shown that for the Blasius boundary layer, the optimal distribution of suction peaks upstream of the maximum growth rate region and is flat in the middle before it decreases to zero at the end of the transition point. For the stationary and travelling cross-flow instability, the optimal distribution peaks upstream of the maximum growth rate region and decreases gradually to zero. Tang *et al.* (1996) use low order models to minimize wake unsteadiness behind a circular cylinder in an incompressible flow regime at $Re=100$ through the rotation of the cylinder about its axis.

Joslin *et al.* (1997) present a self-contained automated methodology for active flow control by combining the time-dependent Navier-Stokes equations with an adjoint system to determine optimality conditions. To validate the proposed methodolgy, the

problem of boundary layer instability suppression through wave cancellation is studied and it is reported that instability suppression can be achieved without any *a priori* knowledge of the disturbance. This is very significant in the light of the fact that other control techniques require some knowledge of the flow unsteadiness, such as, frequencies or instability type.

From the experimental perspective, the recent reviews of Ho and Tai (1996, 1998), and McMicheal (1996) offer well-organized compilation of the research conducted in this field. From the mathematical perspective, the recent dedicated volumes compiled by Banks (1992), Gunzburger (1995), Lagnese *et al.* (1995), and Sritharan (1998) are valuable sources of information.

2.3 Aeroelasticity

In many modern engineering applications, it is desirable to find the effects of design parameter changes on the dynamic response of a system. Integration of the structural and aerodynamic design processes for developing better aerospace structures in an automated manner is the essential step. In turbomachinery blade design, aeroacoustic and aeroelastic considerations play an important role due to governmental regulations and community standards demanding reduced levels of noise on the one hand, and competitive pressures requiring increased efficiency and mechanical reliability on the other hand. The common practice is a loose coupling of the aerodynamic and structural design processes. First, the blade is designed primarily to maximize steady aerodynamic performance and then detailed aeroelastic studies are performed to determine whether the blades satisfy the requirements for flutter stability and flutter. The blade is redesigned if

it fails to meet these requirements and the process is repeated. This process increases the time and expense required for designing a blade and highlights the importance of tight coupling between the underlying unsteady aerodynamics and structural sensitivities.

Murthy and Kaza (1991) develop a semi-analytical approach for the sensitivity analysis of linear unsteady aerodynamic loads, reporting considerable gain in execution time and accuracy over the finite difference approach although only sensitivity coefficients with respect to non-shape design variables are addressed in their work. Arslan and Carlson (1994) investigate the static aeroelastic behavior of transonic flow about an unswept and twisted rectangular wing. The incremental iterative technique is used to couple the structure and flow modules and obtain sensitivity derivatives of the fully coupled system. They show that the sensitivities of the coupled system often exhibit significant differences in magnitude and sometimes sign from the discipline derivatives.

Lorence and Hall (1994) use the full potential equation to compute the effect of perturbations in the shape of the airfoils in a cascade on the steady and unsteady flow through the cascade. They proceed to show that the derived coupled sensitivities can be used to redesign an aeroelastically unstable cascade in torsion to be aeroelastically stable.

Sorenson and Drela (1995) use a time-harmonic formulation of the full potential equation to model a transonic unsteady flow. Due to the highly nonlinear behavior of transonic flows, this restricts their analysis to very small amplitude unsteady oscillations about a mean steady flow. However, this limitation is acceptable because, for flutter calculations, the flutter condition is defined as the point at which infinitesimal oscillations grow unboundedly. They show that a single Newton system can be used to solve three seemingly disparate problems: *1.)* steady analysis module for mean flow

calculations, 2.) harmonic-unsteady module, and 3.) design sensitivity calculations.

Kolonay (1995,1996) develops an indicial response method to approximate unsteady transonic aerodynamics and the resulting transfer functions are used in linear unsteady aeroelastic analyses to allow for multidisciplinary structural optimization in the transonic regime.

2.4 Error Estimation

The adjoint solution can also play a critical role in numerical error analysis. It can be used to analyze the error of computed functionals, such as, lift and drag. As well as offering useful bounds on the accuracy of CFD predictions, the adjoint solution can be also be used as the basis for optimal grid adaptation, giving the most accurate predictions for a given level of computational cost. Literature on the subject is quite limited and until recently, the pioneering works of Johnson and Rannacher (1994) and Becker and Rannacher (1996) were the only available literature in the CFD community for incompressible flows. Giles and Pierce (1999) show that, when solving for the Poisson equation or the quasi-1D Euler equations using second order accurate finite element solutions, fourth order accuracy can be achieved for functional computations in the presence of both curved boundaries and singularities. The additional accuracy is achieved at the cost of a linear adjoint calculation similar to those performed for design optimization. Venditti and Darmofal (1999) also use the method as indictors in a grid-adaptive strategy designed to produce specially tuned grids for accurately estimating the error in functional computations. They present results for quasi-1D Euler equations for both isentropic and shocked flows.

Chapter 3

Continuum Approach for Shape Design Sensitivity Analysis

In shape optimization problems, where the physics of the problem is governed by a set of partial differential equations, one often encounters the problem of relating the variation of a functional to a small variation in the shape of the domain Ω. As it is often assumed that the domain deformations in response to small changes in the design parameters are smooth and regular, Ω can be thought of as a continuous medium and the shape design process can be viewed as a dynamic process of continuous deformation in a continuum. In the light of this similarity, one can borrow extensively from the principles of continuum mechanics to build a framework for shape design sensitivity analysis. A time-like parameter τ may be introduced into the domain deformation process to trace the motion of a point within the domain and a *design velocity* vector field can be defined as the counterpart of the Eulerian velocity in continuum mechanics. The Eulerian velocity measures the velocity of a fluid particle as it passes through a fixed point in space. Similarly, the design velocity field measures the velocity of a point in Ω as it moves under the action of the design transformation. In this section, the building blocks of continuous shape sensitivity analysis are introduced and several relations that will be used in later sections are derived in details.

3.1 Design Velocity Field and Material Derivative

Consider a domain Ω undergoing deformation, shown schematically in Figure 3.1.

The new position of any point in Ω can be written as a function of its original position $\bar{x}$

and the time-like parameter, τ, as:

$$\bar{x}_\tau = \bar{x}_\tau(\bar{x},\tau)$$

<div style="text-align:right">(3.1)</div>
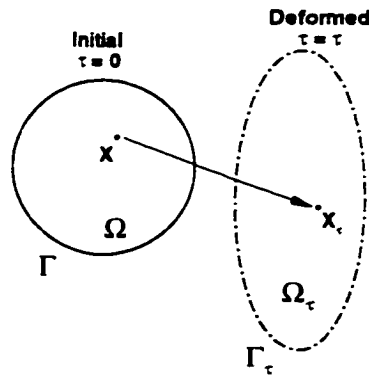
Figure 3.1 Domain deformation in the design process

A design velocity field at the initial configuration of $\tau = 0$ can be defined as

$$\bar{V}(\bar{x}) \equiv \frac{d\bar{x}_\tau}{d\tau}\bigg|_{\tau=0}.$$

<div style="text-align:right">(3.2)</div>

Under certain regularity hypothesis such as existence and boundedness of higher-order

derivatives of $\bar{x}_\tau$, a first-order accurate approximation of $\bar{x}_\tau$ can be written as:

$$\bar{x}_\tau = \bar{x} + \tau \bar{V}(\bar{x}) + O(\tau^2)$$

<div style="text-align:right">(3.3)</div>

With the notion of design velocity in hand, one can proceed and find expressions for the total variation of a state variable, say $z[x_\tau(\bar{x},\tau),\tau]$. The first-order *material derivative* of the state variable z at the undeformed state, i.e., at $\tau = 0$, is denoted by $\overset{\bullet}{z}$ and defined as

$$\overset{\bullet}{z}(\bar{x}) = \lim_{\tau \to 0}\left[\frac{z_\tau(\bar{x}+\tau\bar{V},\tau)-z(\bar{x})}{\tau}\right] = z'(\bar{x}) + \nabla z \cdot \bar{V} . \tag{3.4}$$

In Eq. (3.4), z' is the *local derivative* while the position is held fixed and is defined as:

$$z'(\bar{x}) = \frac{\partial z_\tau(\bar{x},\tau)}{\partial \tau}\bigg|_{\tau=0} \tag{3.5}$$

The design parameter τ and the spatial coordinates $\bar{x}$ are independent variables and assuming that all second order partial derivatives of z with respect to $\bar{x}$ and τ exist and are continuous, the local derivative operator commutes with all spatial derivative operators; e.g., $(\nabla z)' = \nabla z'$.

3.2 Material Derivative Formulas

In this section, the changes in size and orientation of material arc, surface, and volume elements due to the action of the design velocity field are discussed. Subsequently a number of technical material derivative formulae are derived which will serve as the starting points for most of the material presented in this thesis.

3.2.1 Directional Line Differential

Consider an infinitesimally small line element, $\delta\bar{x}$, representing a material line element that remains approximately straight in the course of deformation (Figure 3.2).
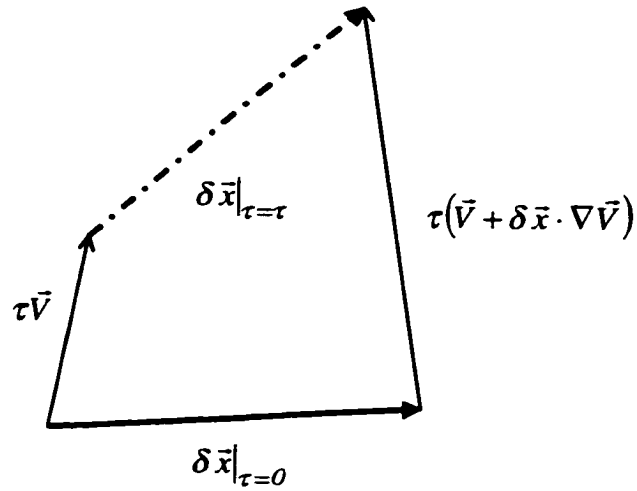
Figure 3.2 Transformation of a line element

It can be readily seen from Figure 3.2 that the material derivative of a line element is related to the gradient of the design velocity as

$$\dot{\delta\vec{x}} \equiv \frac{d\delta\vec{x}}{d\tau}\bigg|_{\tau=0} = \delta\vec{x}\cdot\nabla\vec{V}.$$ (3.6)

Now, Eq. (3.6) is specialized to the *moving trihedral* or *natural* coordinate system (Figure 3.3). $\hat{t}$, $\hat{n}$, and $\hat{b}$ are the unit vectors in the tangential, normal, and bi-normal directions respectively, and their derivatives with respect to the distance traversed along the curve are known collectively as the *Frenet-Serret formulae*, given by:

$$\frac{d\hat{t}}{ds} = \frac{1}{R}\hat{n}, \quad \frac{d\hat{n}}{ds} = \mu\hat{b} - \frac{1}{R}\hat{t}, \quad \frac{d\hat{b}}{ds} = -\mu\hat{n}$$ (3.7)

$R \in (0,+\infty)$ is the radius of curvature and μ is a scalar called the *torsion*.
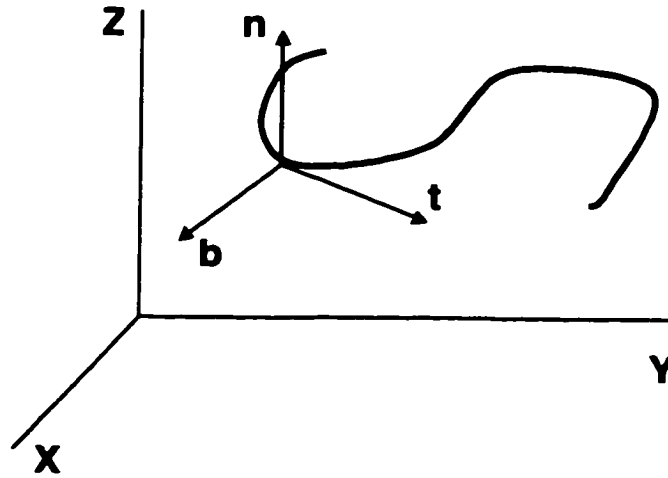
Figure 3.3   Moving trihedral coordinate system

Eq. (3.6) can now be written in terms of the components of the design vector field in the new coordinate system as such:

$$\dot{\delta x} = \left[\left(\frac{\partial v_t}{\partial s} - \frac{v_n}{R}\right)\hat{t} + \left(\frac{\partial v_n}{\partial s} + \frac{v_t}{R} - \mu v_b\right)\hat{n} + \left(\frac{\partial v_b}{\partial s} + \mu v_n\right)\hat{b}\right]|\delta x| \qquad (3.8)$$

The material derivative of the arc length $|\delta \bar{x}|$ simply becomes

$$|\dot{\delta x}| = \frac{\dot{\delta \bar{x}} \cdot \delta \bar{x}}{|\delta \bar{x}|} = \left(\frac{\partial v_t}{\partial s} - \frac{v_n}{R}\right)|\delta \bar{x}| . \qquad (3.9)$$

3.2.2 Volume Differential

An element of volume $\delta \vartheta$ changes its volume owing to the movement of each element $\delta \sigma \hat{n}$ of its bounding surface by $\tau \vec{V}$; $\hat{n}$ being the outward unit normal vector. Using the Gauss' theorem, it can be shown that:

$$\overset{\bullet}{\delta\vartheta} \equiv \frac{d\delta\vartheta}{d\tau}\bigg|_{\tau=0} = \nabla \cdot \vec{V}\delta\vartheta \tag{3.10}$$

3.2.3 Unit Normal

The material derivative of the unit normal to a three dimensional surface is given by the following expression:

$$\overset{\bullet}{\hat{n}} = \left[\hat{n} \cdot \left(\hat{n} \cdot \nabla\vec{V}^T\right)\right]\hat{n} - \hat{n} \cdot \nabla\vec{V}^T \tag{3.11}$$

The derivation of Eq. (3.11) is quite involved and the reader is referred to Haug *et al.* (1986).

3.2.4 Surface Differential

Arbitrary infinitesimal line, surface, and volume elements are related by the following first-order relation:

$$\delta\vartheta = \delta\vec{x} \cdot \delta\sigma\hat{n} \tag{3.12}$$

Material differentitation of Eq. (3.12) with the help of Eqs. (3.6) and (3.10) renders the following expression involving the total derivative of the surface element of area $\delta\sigma$:

$$\delta\vec{x} \cdot \left(\frac{d\delta\sigma}{d\tau}\bigg|_{\tau=0} \cdot \hat{n} + \delta\sigma\frac{d\hat{n}}{d\tau}\bigg|_{\tau=0}\right) = -\left(\delta\vec{x} \cdot \nabla\vec{V}\right) \cdot \delta\sigma\hat{n} + \nabla \cdot \vec{V}\delta\vartheta \tag{3.13}$$

As $\delta\vec{x}$ is arbitrary, it can be set equal to the unit normal $\hat{n}$ and Eq. (3.13) simplifies to

$$\frac{1}{\delta\sigma}\frac{d\delta\sigma}{d\tau}\bigg|_{\tau=0} = -\hat{n} \cdot \frac{d\hat{n}}{d\tau}\bigg|_{\tau=0} - \left(\hat{n} \cdot \nabla\vec{V}\right) \cdot \hat{n} + \nabla \cdot \vec{V} . \tag{3.14}$$

Substituting for $\overset{\bullet}{\hat{n}}$ from Eq. (3.11) in Eq. (3.14), the following expression for the design

derivative of a surface differential is obtained.

$$\overset{\bullet}{\delta\sigma} \equiv \frac{d\delta\sigma}{d\tau}\bigg|_{\tau=0} = [\nabla \cdot \vec{V} - (\hat{n} \cdot \nabla\vec{V}) \cdot \hat{n}]\delta\sigma \qquad (3.15)$$

3.2.5 Domain, Surface and Line Functionals

Let Ψ be a domain functional defined as an integral over Ω,

$$\Psi = \int_\Omega f(\bar{x}) d\vartheta \qquad (3.16)$$

where f is a regular function defined on Ω. This integral is only a function of τ and there

will be contributions to its material derivative due to both changes in the value of the

functional and changes in the shape and size of the domain as it deforms under the action

of the design velocity field. At any instant, the integral functional can be viewed as the

limiting sum of the contributions from an infinite number of infinitesimal volume

elements. Therefore, the design derivative of the domain functional Ψ can be written as

$$\begin{aligned}
\overset{\bullet}{\Psi} &= \int_\Omega \overset{\bullet}{f} d\vartheta + \int_\Omega f \overset{\bullet}{d\vartheta} \\
&= \int_\Omega (f' + \nabla f \cdot \vec{V}) d\vartheta + \int_\Omega f\nabla \cdot \vec{V} d\vartheta \qquad (3.17) \\
&= \int_\Omega f' d\vartheta + \int_\Gamma f\vec{V} \cdot \hat{n} d\sigma
\end{aligned}$$

where Γ is the boundary of the domain. Eqs. (3.4) and (3.10) in conjunction with the

Gauss' divergence theorem have been used to render the final form of Eq. (3.17).

In a similar fashion, the design derivative of a surface functional of the form

$$\Theta = \int_\Gamma f(\bar{x}) d\sigma \qquad (3.18)$$

can be written as:

$$\dot{\Theta} = \int_\Gamma \left[\dot{f} + f\left(\nabla \cdot \vec{V} - \left(\nabla \vec{V} \cdot \hat{n}\right) \cdot \hat{n}\right) \right] d\sigma \tag{3.19}$$

Consider the following line functional:

$$\Lambda = \int_C f(\vec{x})|d\vec{x}| \tag{3.20}$$

Upon using Eqs. (3.4) and (3.9), and performing integration by parts, the following expression is obtained for the derivative of the line functional Λ:

$$\dot{\Lambda} = \int_C \left[\dot{f} + v_n\left(\frac{\partial f}{\partial n} - \frac{f}{R}\right) \right] |d\vec{x}| + f v_t \big|_{\vec{x}_A}^{\vec{x}_B} \tag{3.21}$$

$\vec{x}_A$ and $\vec{x}_B$ are the end points of the curve C and obviously for a closed contour the last term on the right hand side of Eq. (3.21) will be identically zero.

In two dimensions, the orthogonal curvilinear coordinates s-n differs from the natural coordinate system, used so far in this chapter, in a subtle manner. In the natural coordinate system, the curvature, κ, is always a positive quantity with the unit normal always pointing towards the center of curvature. In the s-n system, the unit normal is conventionally chosen to point consistently towards the interior or the exterior of the domain irrespective of the curvature of the path. Consequently, κ changes sign depending on the local convexity of the path. Figure 3.4 illustrates the difference between the two systems and the sign convention used for κ in this dissertation. The s-n coordinates will be used extensively in this thesis from this point onwards and it should be noted that a negative sign needs to be inserted in front of the curvature terms present in Eqs. (3.8), (3.9), (3.21) to render the aforementioned equations applicable to the s-n coordinate system.

To conclude this chapter, it is sought after the design derivative of a functional defined on a 2-D space with the tangential component of the state vector field as its integrand. Such functional can be written formally as

$$\aleph = \int_C f(\vec{q} \cdot \hat{t})|d\vec{x}|.$$

(3.22)

(a)

Natural Coordinates
κ > 0

(b)
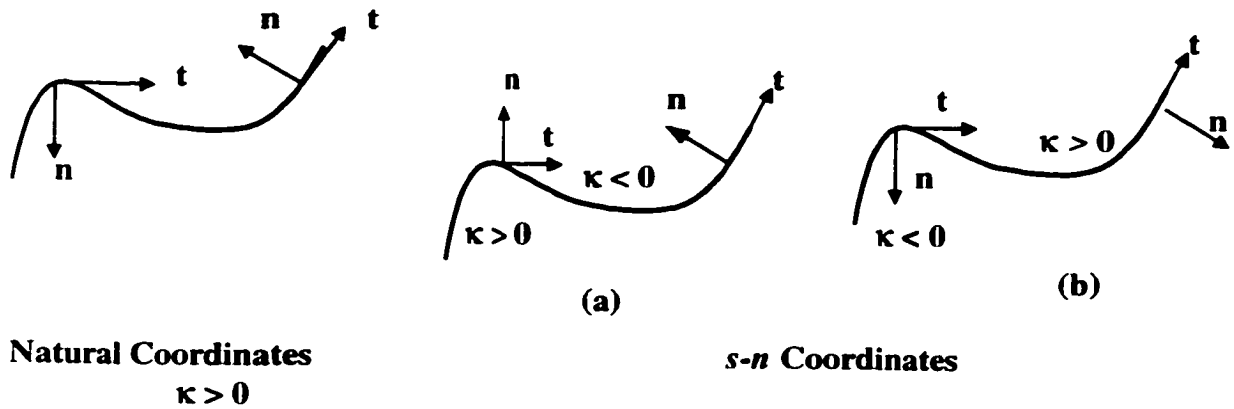
s-n Coordinates

Figure 3.4 Natural coordinates vs s-n coordinates

This functional is different from Λ in Eq. (3.22) due to the integrand containing an element of geometry, $\hat{t}$, embedded within. Denoting the tangential component of $\vec{q}$ with q_s, the design derivative of Eq. (3.22) can be written as:

$$\overset{\bullet}{\aleph} = \int_C \left[\frac{\partial f}{\partial q_s} \overset{\bullet}{q_s} + \left(\frac{\partial v_s}{\partial s} + \frac{v_n}{R} \right) f \right] |d\vec{x}|$$

(3.23)

If $\vec{q}$ is resolved into its components in the s-n coordinate system, the material derivative of q_s takes the form

$$\overset{\bullet}{q_s} = \vec{q}' \cdot \hat{t} + (\vec{V} \cdot \nabla \vec{q}) \cdot \hat{t} + q_s \hat{t} \cdot \overset{\bullet}{\hat{t}} + q_n \hat{n} \cdot \overset{\bullet}{\hat{t}}.$$

(3.24)

The gradient of a vector field is a second order tensor which for an arbitrary vector $\vec{a} = a_s \hat{t} + a_n \hat{n}$ takes the following form in the s-n orthogonal curvilinear coordinate system:

$$\nabla \vec{a} = \begin{bmatrix} \dfrac{1}{1+n\kappa}\left(\dfrac{\partial a_s}{\partial s} + a_n \kappa\right) & \dfrac{1}{1+n\kappa}\left(\dfrac{\partial a_n}{\partial s} - a_s \kappa\right) \\ \dfrac{\partial a_s}{\partial n} & \dfrac{\partial a_n}{\partial n} \end{bmatrix} \tag{3.25}$$

The convective derivative term of Eq. (3.24) can now be simplified as:

$$\left(\vec{V} \cdot \nabla \vec{q}\right) \cdot \hat{t} = v_s \left(\frac{\partial q_s}{\partial s} + \frac{q_n}{R}\right) + v_n \frac{\partial q_s}{\partial n} \tag{3.26}$$

Since $\hat{t}$ and $\hat{n}$ are unit vectors,

$$\begin{cases} \overset{\bullet}{\hat{t}} \cdot \hat{t} = 0 \\ \hat{n} \cdot \overset{\bullet}{\hat{t}} = -\overset{\bullet}{\hat{n}} \cdot \hat{t} \end{cases}, \tag{3.27}$$

it can be easily shown with the aid of the Eq. (3.11) that

$$\hat{n} \cdot \overset{\bullet}{\hat{t}} = \hat{n} \cdot \left(\nabla \vec{V}^T \cdot \hat{t}\right) = \hat{n} \cdot \frac{\partial \vec{V}}{\partial s} = \frac{\partial v_n}{\partial s} - \frac{v_s}{R}. \tag{3.28}$$

Upon substitution of Eqs. (3.26), (3.27) and (3.28) in Eq. (3.24), the material derivative of the tangential component of a vector field can be written as:

$$\begin{aligned} \overset{\bullet}{q_s} &= \vec{q}' \cdot \hat{t} + v_s \left(\frac{\partial q_s}{\partial s} + \frac{q_n}{R}\right) + v_n \frac{\partial q_s}{\partial n} + q_n \left(\frac{\partial v_n}{\partial s} - \frac{v_s}{R}\right) \\ &= q_s' + v_s \frac{\partial q_s}{\partial s} + v_n \frac{\partial q_s}{\partial n} + q_n \frac{\partial v_n}{\partial s} \end{aligned} \tag{3.29}$$

Substitution of Eq. (3.29) in Eq. (3.23) and integration by parts renders the material derivative of the functional as:

$$\dot{\aleph} = \int_{C} \left[f' + v_n \left(\frac{\partial f}{\partial n} + \frac{f}{R} \right) + \frac{\partial f}{\partial q_s} \frac{\partial v_n}{\partial s} q_n \right] |d\vec{x}| + f v_t \Big|_{\vec{x}_A}^{\vec{x}_B} \tag{3.30}$$

Note that the third term in Eq.(3.30) does not exist in Eq. (3.21).

Chapter 4

Continuous Adjoint Sensitivities of the 2D Euler Equations

Chapter 3 presented the essential material derivative formulae needed for obtaining the first variation of line, surface, and volume functionals. This chapter explores the application of the continuous adjoint methodology to the optimization of general aerodynamic cost functionals in the context of the steady two-dimensional Euler equations discretized on an unstructured grid. In the following, a summary of the motivation for the work presented in this chapter is given.

The term 'general cost functional' refers to cost functionals not solely dependent on pressure on the control surface. Anderson and Venkatakrishnan (1997) and Jameson *et al.* (1998) reported difficulties with the proper closure of a Lagrangian associated with the Euler equations and general functionals while Giles and Pierce (1997) concluded that only certain choices of objective functionals would lead to a well-posed problem. However, according to the theory of functional analysis adjoint variables exist for any cost functional and Arian and Salas (1997) were the first to find a remedy for this problem for the potential, Euler, and Navier-Stokes equations. They showed that the inclusion of additional terms in the Lagrangian functional, resulting from the restriction of the interior PDE to the control surface, could alleviate the difficulties in the derivation of the boundary conditions for the adjoint problem. The development here is in line with that of Anderson and Venkatakrishnan (1997) with the significant difference being that the method is extended to general objective functions for the steady 2-D Euler equations in a more direct manner compared to that discussed in Arian and Salas (1997).

In the course of this chapter, it is also pointed out that accurate computation of normal derivatives of state and/or adjoint variables on the design surface is crucial for calculation of accurate shape design sensitivity information, often expressed as a surface or line integral over the design surface. However, Babuska paradox, as discussed in Strang and Fix (1973), states that when linear segments are used for representing a curved boundary, the solution for normal derivatives to the boundary may not be accurate. This poses a major problem for finite volume discretizations on first order triangular elements as the boundary is indeed represented with piece-wise linear segments. In this work, it will be demonstrated that a transformation to the body-fitted coordinates, s-n, along with the application of the governing state equations on the control surface can be used to eliminate normal derivatives from the sensitivity integrals resulting in accurate sensitivity information.

It should also be noted that the mathematical relations of Chapter 3 and the formulation of this chapter are only valid if the state variables of interest vary smoothly in the domain. Therefore, the formulation is not strictly valid for a flow with a shock discontinuity. From the numerical point of view, however, the numerical damping present in CFD solvers transforms a shock discontinuity into a thin region of finite width where the flow experiences a very sharp gradient in flow quantities. This is the premise of the 'shock capturing' methods that are widely used in CFD practice. An alternative approach can be derived based on the 'shock fitting' approach where the shock location is determined iteratively by imposing the Rankine-Hugoniot relations across the shock. Hence, one can actually get away with the following formulation, which does not take the shock discontinuity into account.

4.1 Optimal Design Problem

The state equations considered in the present method are the Euler equations of fluid flow:

$$\frac{\partial \bar{Q}}{\partial t} + \frac{\partial \bar{F}}{\partial x} + \frac{\partial \bar{G}}{\partial y} = 0 \tag{4.1}$$

The vector of conserved variables, $\bar{Q}$, and the flux vectors $\bar{F}$ and $\bar{G}$ in the respective x and y directions are written as

$$\bar{Q} = \begin{bmatrix} \rho \\ \rho u \\ \rho v \\ \rho E \end{bmatrix} \qquad \bar{F} = \begin{bmatrix} \rho u \\ \rho u^2 + P \\ \rho uv \\ \rho uH \end{bmatrix} \qquad \bar{G} = \begin{bmatrix} \rho v \\ \rho uv \\ \rho v^2 + P \\ \rho vH \end{bmatrix}. \tag{4.2}$$

Suitable boundary conditions are applied along the whole or part of the boundary $\Gamma = \Gamma_s \cup \Gamma_o$ of the domain sketched in Figure 4.1.
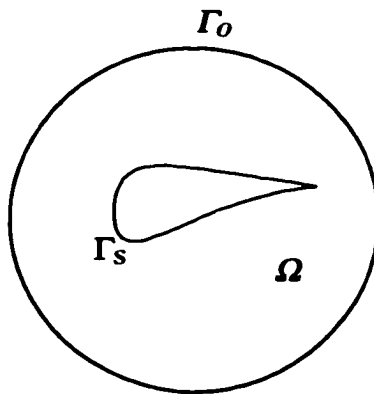
Figure 4.1 Sketch describing a domain Ω with design surface Γ_s and outer boundary Γ_o

The objective functional, I_C, is a general function of pressure, density, and tangential velocity on the body surface that can be written implicitly as:

$$I_c = \int_{\Gamma_r} f(\, p, \rho, u_s \,) \, ds \qquad (4.3)$$

In the above, u_s and ds, denote the tangential velocity and the arc length differential respectively. The optimal design problem under consideration is simply minimization of the above general objective functional.

4.2 Continuous Adjoint Method

I_C is a function of the state variables, $\bar{Q}$, and the governing state equations and its boundary conditions are the constraints subject to which I_C has to be extremized. In line with the method of Lagrange multipliers, an augmented cost functional is introduced as

$$I = I_c + I_R \qquad (4.4)$$

where I_R is the inner product of the governing state equations and its boundary conditions with respective Lagrange multipliers $\bar{\lambda}$ in the domain and ψ on the boundary.

$$I_R = \int_{\Omega} \left(\frac{\partial \bar{F}^T}{\partial x} + \frac{\partial \bar{G}^T}{\partial y} \right) \cdot \bar{\lambda} \, d\Omega + \int_{\Gamma_r} \psi(\rho \bar{q} \cdot \hat{n}) \, ds \qquad (4.5)$$

The farfield boundary condition is not included in Eq. (4.5) and will be treated separately.

4.2.1 First Variation of the Objective Functional

If the cost functional, I_C, was a function of purely field variables such as the pressure or density, Eq. (3.21) could be used directly to yield the first variation with respect to the boundary. However, the tangential velocity on the surface has an element of the surface orientation embedded within that necessitates a special treatment. This simply emanates from the fact that the design derivative of the tangential unit vector to the curve does not have a convective derivative part. Using Eq. (3.21) for the first two arguments of I_C, and Eq. (3.30) for the third argument, u_s, the first variation of I_C can be written as:

$$\dot{I}_C = \int_{\Gamma_s} \left[\begin{array}{c} f_p \left(p' + \vec{V} \cdot \nabla p \right) + f_\rho \left(\rho' + \vec{V} \cdot \nabla \rho \right) \\ + f_{u_s} \left(u_s' + u_n \frac{\partial \left(\vec{V} \cdot \hat{n} \right)}{\partial s} + \frac{\partial u_s}{\partial s} \left(\vec{V} \cdot \hat{t} \right) + \frac{\partial u_s}{\partial n} \left(\vec{V} \cdot \hat{n} \right) \right) \\ + f \left(\frac{\partial \left(\vec{V} \cdot \hat{t} \right)}{\partial s} + \frac{\left(\vec{V} \cdot \hat{n} \right)}{R} \right) \end{array} \right] ds \tag{4.6}$$

Specializing the gradient operator to the s-n orthogonal curvilinear coordinates and noting that the control surface is located on the $n=0$ line renders Eq. (4.6) in the following form:

$$\dot{I}_C = \int_{\Gamma_s} \left(f' + \frac{\partial f}{\partial n} \left(\vec{V} \cdot \hat{n} \right) + \frac{\partial f}{\partial s} \left(\vec{V} \cdot \hat{t} \right) \right) ds + \int_{\Gamma_s} \left[f \left(\frac{\partial \left(\vec{V} \cdot \hat{t} \right)}{\partial s} + \frac{\left(\vec{V} \cdot \hat{n} \right)}{R} \right) + f_{u_s} u_n \frac{\partial \left(\vec{V} \cdot \hat{n} \right)}{\partial s} \right] ds \tag{4.7}$$

The tangential derivatives of the above equation form a complete differential that can be integrated directly, resulting in an additional term at the contour endpoints.

$$\dot{I}_C = \int_{\Gamma_s} \left(f' + \frac{\partial f}{\partial n} \left(\vec{V} \cdot \hat{n} \right) + f \frac{\left(\vec{V} \cdot \hat{n} \right)}{R} + f_{u_s} u_n \frac{\partial \left(\vec{V} \cdot \hat{n} \right)}{\partial s} \right) ds + \left[f \left(\vec{V} \cdot \hat{t} \right) \right]_{\vec{x}_A}^{\vec{x}_B} \tag{4.8}$$

For a closed contour or an open contour with fixed end points, the last term is identically zero. Furthermore, if the design contour lies on the airfoil surface, which is the case here, u_n is zero and the fourth term can also be dropped from Eq. (4.8). However, it should also be noted that for an oscillating airfoil or an airfoil with suction or blowing over a portion of its surface, the fourth term could not be omitted from the above equation. The fourth term reflects the influence of the boundary condition type on the design derivative of the objective functional. It must be kept in mind, however, that the sign convention used for the radius of curvature is that of case (b) in Figure (3.4).

4.2.2 First Variation of the Augmented Cost Functional

In this section, the first variation of I_R, which comprises of two integrals over the domain and airfoil surface, is found using Eqs. (3.20)-(3.24) as follows:

$$\dot{I}_R = \int_\Omega \left(\frac{\partial \bar{F}'^T}{\partial x} + \frac{\partial \bar{G}'^T}{\partial y} \right) \cdot \bar{\lambda} d\Omega + \int_{\Gamma_s} \psi \left((\rho\bar{q})' \cdot \hat{n} + \rho\bar{q} \cdot \dot{\hat{n}} + (\bar{V} \cdot \nabla(\rho\bar{q})) \cdot \hat{n} \right) ds \qquad (4.9)$$

Next, the derivative operators in the first integral are transferred to the adjoint variable by the means of the Gauss' theorem. Also, local derivative of the fluxes are written in terms of the local variation of the vector of conserved variables, $\bar{Q}$, and the flux Jacobians,

$$A \equiv \frac{\partial \bar{F}}{\partial \bar{Q}} \text{ and } B \equiv \frac{\partial \bar{G}}{\partial \bar{Q}}, \text{ by using the chain rule}[1].$$

$$\dot{I}_R = -\int_\Omega Q'^T \left(A^T \cdot \bar{\lambda}_x + B^T \cdot \bar{\lambda}_y \right) d\Omega$$

$$+ \int_{\Gamma = \Gamma_s + \Gamma_o} \left(n_x \bar{F}' + n_y \bar{G}' \right)^T \cdot \bar{\lambda} ds + \int_{\Gamma_s} \psi \left((\rho\bar{q})' \cdot \hat{n} + \rho\bar{q} \cdot \dot{\hat{n}} + (\bar{V} \cdot \nabla(\rho\bar{q})) \cdot \hat{n} \right) ds \qquad (4.10)$$

On the airfoil surface, the integrand of the second integral in Eq. (4.10) can be written in terms of pressure and mass flux vector variations in the following way.

$$n_x \vec{F}' + n_y \vec{G}' = \begin{bmatrix} 1 \\ u \\ v \\ H \end{bmatrix} \Xi + \begin{bmatrix} 0 \\ n_x \\ n_y \\ 0 \end{bmatrix} p' \qquad \Xi = (\rho \vec{q})' \cdot \hat{n} \qquad (4.11)$$

Expanding the last two terms, and using Eq. (4.11), the first variation of the augmented cost functional takes the following form:

$$\begin{aligned} I = &\int_{\Gamma_s} \left\{ f_p p' + f_\rho \rho' + f_{u_s} u'_s + \left(\frac{\partial f}{\partial n} + \frac{f}{R} \right)(\vec{V} \cdot \hat{n}) \right\} ds \\ &- \int_\Omega Q'^T \left(A^T \cdot \vec{\lambda}_x + B^T \cdot \vec{\lambda}_y \right) d\Omega + \int_{\Gamma_o} \left(n_x \vec{F}' + n_y \vec{G}' \right) \cdot \vec{\lambda} \, ds \\ &+ \int_{\Gamma_s} \Xi (\lambda_1 + u\lambda_2 + v\lambda_3 + H\lambda_4) \, ds + \int_{\Gamma_s} p'\left(n_x \lambda_2 + n_y \lambda_3 \right) ds \\ &+ \int_{\Gamma_s} \psi \left(\Xi + \rho \vec{q} \cdot \dot{\hat{n}} + (\vec{V} \cdot \nabla(\rho \vec{q})) \cdot \hat{n} \right) ds \end{aligned} \qquad (4.12)$$

4.3 Adjoint Problem Statement

The domain integral is removed from Eq. (4.12) by requiring that the Lagrange variables satisfy the following adjoint equation:

$$A^T \cdot \frac{\partial \vec{\lambda}}{\partial x} + B^T \cdot \frac{\partial \vec{\lambda}}{\partial y} = 0 \qquad \forall \vec{x} \in \Omega \qquad (4.13)$$

It is evident from Eq. (4.13) that the adjoint of the quasi-linear Euler equations is a linear system with variable coefficients. Some of the terms involving the variations of the flow quantities with respect to the boundary can be eliminated by simply setting the following relation to zero:

---

[1] The details of the algebraic manipulations needed to obtain Eq. (4.10) is provided in Appendix A.

$$\psi + \left(\lambda_1 + u\lambda_2 + v\lambda_3 + H\lambda_4 \right) = 0. \tag{4.14}$$

4.3.1 Farfield Boundary Condition

The farfield integral boundary condition can be rewritten in the following form:

$$\int_{\Gamma_o} \bar{Q}'^T \cdot \bar{A}^T \cdot \bar{\lambda} = 0 \tag{4.15}$$

In this equation, $\bar{A} = n_x A + n_y B$ is the Jacobian matrix associated with the direction of propagation $\hat{n}$. As the adjoint equation in domain (Eq. (4.13)) is a mixed elliptic-hyperbolic equation, the adjoint variable cannot be set to zero everywhere at the farfield. Therefore, it is desirable to put the Eq. (4.15) in a form that some characteristic information can be deduced from it. This can be done by the standard characteristic transformation

$$\begin{aligned} \bar{W}' &= T^{-1} \cdot \bar{Q}' \\ \bar{A} &= T \cdot \Lambda \cdot T^{-1} \\ \Lambda &= Diag \begin{bmatrix} \bar{q} \cdot \hat{n} & \bar{q} \cdot \hat{n} & \bar{q} \cdot \hat{n} + c & \bar{q} \cdot \hat{n} - c \end{bmatrix} \end{aligned} \tag{4.16}$$

where c is the local speed of sound, the columns of T are the right eigenvectors of $\bar{A}$, and the rows of T^{-1} are the left eigenvectors of the same matrix. If a new adjoint variable is also defined as

$$\bar{\Theta} = T^T \cdot \bar{\lambda} \tag{4.17}$$

the farfield boundary condition in terms of the transformed adjoint variable, $\bar{\Theta}$, reduces to the following simple form:

$$\int_{\Gamma_o} \bar{W}'^{T} \cdot \Lambda \cdot \bar{\Theta} ds = 0 \tag{4.18}$$

If the farfield conditions are kept constant, the characteristic variable W'_i corresponding to the ith eigenvalue will be zero for negative eigenvalues. If Θ_i corresponding to the ith positive eigenvalue of $\bar{A}$, is denoted by Θ_i^{+}, the farfield boundary condition will be satisfied if

$$\Theta_i^{+} = 0 . \tag{4.19}$$

Table 4.1 presents the different scenarios in the farfield and the corresponding boundary conditions for the adjoint variables.

	Physical Conditions	**Numerical Conditions**
Subsonic outlet	$\theta_1, \theta_2, \theta_3$	θ_4
Supersonic outlet	$\theta_1, \theta_2, \theta_3, \theta_4$	None
Subsonic inlet	θ_3	$\theta_1, \theta_2, \theta_4$
Supersonic inlet	None	$\theta_1, \theta_2, \theta_3, \theta_4$

Table 4.1 Physical and numerical boundary conditions at the farfield.

However, these boundary conditions on $\bar{\Theta}$ should be transformed back to the original adjoint variable $\bar{\lambda}$. Hence, at any point on the farfield boundary, matrix T defined as

$$T = \begin{bmatrix} 1 & 0 & \dfrac{\rho}{2c} & \dfrac{\rho}{2c} \\[2mm] u & \rho n_y & \dfrac{\rho}{2c}(u+cn_x) & \dfrac{\rho}{2c}(u-cn_x) \\[2mm] v & -\rho n_y & \dfrac{\rho}{2c}(v+cn_y) & \dfrac{\rho}{2c}(v-cn_y) \\[2mm] \dfrac{\vec{q}\cdot\vec{q}}{2} & \rho(un_y-vn_x) & \dfrac{\rho}{2c}(H+c\vec{q}\cdot\hat{n}) & \dfrac{\rho}{2c}(H-c\vec{q}\cdot\hat{n}) \end{bmatrix} \qquad (4.20)$$

is formed and the entries of the LHS of Eq. (4.17) are filled with zeros for the physical conditions and with the extrapolated values of the adjoint variables from the inner domain (e.g. from the cell centers) for the numerical conditions. Subsequently, Eq. (4.17) can be inverted to obtain the adjoint variable $\vec{\lambda}$ at the farfield.

4.3.2 Generalized Wall Boundary Condition

This far, the expression for the first variation of the augmented cost functional has been reduced to

$$\begin{aligned} \bar{I} = &\int_{\Gamma_s}\{f_p p' + f_\rho \rho' + f_{u_s} u'_s + p'(n_x\lambda_2 + n_y\lambda_3)\}ds \\ &- \int_{\Gamma_s}(\lambda_1 + u\lambda_2 + v\lambda_3 + H\lambda_4)\left(\rho\vec{q}\cdot\dot{\hat{n}} + (\vec{V}\cdot\nabla(\rho\vec{q}))\cdot\hat{n}\right)ds \\ &+ \int_{\Gamma_s}\left(\frac{\partial f}{\partial n} + \frac{f}{R}\right)(\vec{V}\cdot\hat{n})ds \end{aligned} \qquad (4.21)$$

In Eq. (4.21), the first integral contains all the local variations of the flow variables and the second and the third integrals contribute directly to the sensitivities. As there are no additional terms to balance local variations of density and tangential velocity, it seems at the first sight that the local variations p', ρ', u'_s can only be eliminated from Eq. (4.21) for

objective functionals solely dependent on the pressure. However, one should note that the pressure, density, and tangential velocity are not independent quantities on the airfoil surface. Because the steady Eulerian flow is inviscid and adiabatic, it is isentropic along the streamlines, but obviously with different constants of proportionality $\frac{p}{\rho^\gamma}$ before and after the shock. Therefore, density or temperature variations can be easily written in terms of the pressure variation as

$$p' = \frac{\gamma p}{\rho} \rho'.^2 \tag{4.22}$$

Furthermore, the pressure and tangential velocity are related through the momentum equation in the s-direction on the airfoil surface ($n = 0$, $u_n = 0$) as follows:

$$\frac{\partial p}{\partial s} + \rho u_s \frac{\partial u_s}{\partial s} + \rho u_n \left(1 + \frac{n}{R}\right)\frac{\partial u_s}{\partial n} + \frac{\rho u_s u_n}{R+n} = 0 \quad \Rightarrow \quad p' = -\rho u_s u_s' \tag{4.23}$$

With the aid of Eqs. (4.22)-(4.23), the generalized wall boundary condition can be written as:

$$n_x \lambda_2 + n_y \lambda_3 + f_p + \frac{\rho}{\gamma p} f_\rho - \frac{f_{u_s}}{\rho u_s} = 0 \tag{4.24}$$

At this stage the adjoint system comprising of Eqs. (4.13),(4.19), (4.24) can be solved for the adjoint variable $\bar{\lambda}$.

---

[2] The relationship between the variations of density, pressure, and the tangential velocity can also be found from the conservation of total enthalpy.

$$\frac{p'\rho - p\rho'}{\rho} + \frac{\gamma-1}{\gamma}\rho u_s u_s' = 0.$$

4.4 Sensitivity Derivatives

The first-variation of the augmented functional now reduces to:

$$i = -\int_{\Gamma_s} \Pi\left(\rho\bar{q}\cdot\dot{\hat{n}} + \left(\bar{V}\cdot\nabla(\rho\bar{q})\right)\cdot\hat{n} \right)ds + \int_{\Gamma_s}\left(\frac{\partial f}{\partial n} + \frac{f}{R}\right)\left(\bar{V}\cdot\hat{n}\right)ds$$

$$\Pi = \lambda_1 + u\lambda_2 + v\lambda_3 + H\lambda_4$$

(4.25)

As it has already been mentioned, it is necessary to switch to body-fitted coordinates s-n to rid the above expression from non-tangential directional derivatives. However, certain control surface parameterizations result in unidirectional design velocity fields and the proposed formulation must be able to take the utmost advantage of this simplifying condition. As such, two slightly different approaches can be used:

i)   Full transformation to the s-n plane

ii)   Coexistence of the Cartesian and s-n coordinate systems in the formulation

In approach i), one can show by straightforward algebraic manipulations that the Eq. (3.14) can be specialized for a 2D curve in the s-n coordinates as

$$\dot{\hat{n}} = \left(\frac{\partial(\bar{V}\cdot\hat{n})}{\partial s} - \frac{\bar{V}\cdot\hat{t}}{R}\right)\hat{t} = \theta'\hat{t}$$

(4.26)

where θ is the angle between the tangent and the positive x-axis. Also, the convective derivative term of Eq. (4.25) with $\hat{n} = \begin{bmatrix} 0 & -1 \end{bmatrix}^T$ can be written as:

$$\left(\bar{V}\cdot\nabla(\rho\bar{q})\right)\cdot\hat{n} = \left(-\frac{\partial}{\partial s}(\rho u_n) + \frac{\rho u_s}{R}\right)\left(\bar{V}\cdot\hat{t}\right) - \frac{\partial}{\partial n}(\rho u_n)\left(\bar{V}\cdot\hat{n}\right)$$

(4.27)

The normal derivative term in Eq. (4.27) can be eliminated by using the continuity equation in the s-n coordinate system.

$$\frac{\partial}{\partial s}(\rho u_s) + \frac{\partial}{\partial n}(\rho u_n) - \frac{\rho u_n}{R} = 0 \ . \tag{4.28}$$

Furthermore, for a solid wall with no suction or blowing, Eq. (4.27) can be further simplified as

$$\left(\vec{V} \cdot \nabla(\rho \, \vec{q})\right) \cdot \hat{n} = \vec{V} \cdot \left(\frac{\rho u_s}{R}\hat{t} + \frac{\partial}{\partial s}(\rho u_s)\hat{n}\right) \tag{4.29}$$

Substituting Eqs. (4.27) and (4.29) back in Eq. (4.25) yields

$$I = -\int_{\Gamma_s} \Pi\left(\rho u_s \theta' + \frac{\rho u_s}{R}(\vec{V} \cdot \hat{t}) + \frac{\partial}{\partial s}(\rho u_s)(\vec{V} \cdot \hat{n})\right)ds + \int_{\Gamma_s}\left(\frac{\partial f}{\partial n} - \frac{f}{R}\right)(\vec{V} \cdot \hat{n})ds \ . \tag{4.30}$$

In approach ii), the convective derivative term of Eq. (4.25) takes the following form in the Cartesian coordinates:

$$\left(\vec{V} \cdot \nabla(\rho \, \vec{q})\right) \cdot \hat{n} = \vec{V} \cdot \left(n_x \nabla(\rho u) + n_y \nabla(\rho v)\right) \tag{4.31}$$

The Cartesian components of Eq. (4.31) can be found very easily by applying a rotation of axis to the results of Eq. (4.29).

$$n_x \nabla(\rho u) + n_y \nabla(\rho v) = \begin{bmatrix} \kappa \rho u_s \cos\theta - \sin\theta \dfrac{\partial(\rho u_s)}{\partial s} \\[2mm] \kappa \rho u_s \sin\theta + \cos\theta \dfrac{\partial(\rho u_s)}{\partial s} \end{bmatrix} \tag{4.32}$$

Therefore, the final form of the sensitivities for approach ii) is

$$I = -\int_{\Gamma_s} \Pi \begin{pmatrix} \rho u_s \theta' + \left(\kappa \rho u_s \cos\theta - \sin\theta \dfrac{\partial(\rho u_s)}{\partial s}\right)(\vec{V} \cdot \hat{i}) + \\[3mm] \left(\kappa \rho u_s \sin\theta + \cos\theta \dfrac{\partial(\rho u_s)}{\partial s}\right)(\vec{V} \cdot \hat{j}) \end{pmatrix} ds + \int_{\Gamma_s}\left(\frac{\partial f}{\partial n} + \frac{f}{R}\right)(\vec{V} \cdot \hat{n})ds \ . \tag{4.33}$$

As it is apparent from Eqs. (4.30) and (4.33), the normal derivative of flow quantities to the control surface only appear implicitly in the normal derivative of the cost functional. Accurate computation of these derivatives is the subject of the following section.

4.4.1 Normal Derivatives of Flow Quantities

The method of approach here is to write the Euler equations in the s-n coordinates and come up with equations relating normal derivatives of flow variables to expressions involving only tangential derivatives. The governing equations in the s-n coordinates are:

$$\frac{\partial}{\partial s}(\rho u_s) + \frac{\partial}{\partial n}(\rho u_n) - \frac{\rho u_n}{R} = 0 \tag{4.34}$$

$$\frac{\partial p}{\partial s} + \rho u_s \frac{\partial u_s}{\partial s} + \rho u_n \left(1 + \frac{n}{R}\right)\frac{\partial u_s}{\partial n} + \frac{\rho u_s u_n}{R+n} = 0 \tag{4.35}$$

$$\frac{\partial p}{\partial n} - \frac{\rho u_s^2}{R+n} + \frac{\rho u_s}{1+\frac{n}{R}}\frac{\partial u_n}{\partial s} + \rho u_n \frac{\partial u_n}{\partial n} = 0 \tag{4.36}$$

$$\frac{\partial}{\partial s}(\rho u_s H) + \frac{\partial}{\partial n}\left(\frac{R\rho u_n H}{n+R}\right) = 0 \tag{4.37}$$

Also, one should note that on the surface, $n=0$, the normal component of velocity, u_n, vanishes. The normal derivative of pressure can be found directly from the normal momentum equation as

$$\frac{\partial p}{\partial n} = \frac{\rho u_s^2}{R} \tag{4.38}$$

Normal derivatives of density and tangential velocity are more involved. The energy equation on the airfoil surface can be simplified to show that the total enthalpy is constant throughout the flowfield before and after the shock.

$$H = C_p T + \frac{u_s^2}{2} = Const.$$ (4.39)

Eq. (4.39) cannot be differentiated with respect to n because it is valid only at $n=0$. However, if $\frac{u_s^2}{2}$ is replaced by $\frac{u_s^2 + u_n^2}{2}$ in Eq. (4.39), then it can be differentiated with respect to n to provide the following relationship between the normal derivatives of density, pressure and tangential velocity.

$$\frac{\partial \rho}{\partial n} = \frac{\gamma}{a^2} \frac{\partial p}{\partial n} + \frac{\rho u_s}{a^2} (\gamma - 1) \frac{\partial u_s}{\partial n}$$ (4.40)

If the tangential momentum equation is differentiated with respect to n, and normal derivatives of pressure and density are substituted from Eqs. (4.38) and (4.40) respectively, the following first order differential equation will result:

$$\frac{\partial}{\partial s}\left(\frac{\partial u_s}{\partial n}\right) + \left(\frac{\partial u_s}{\partial n}\right)\left(\frac{u_s}{a^2}(\gamma - 1)\frac{\partial u_s}{\partial s} - \frac{1}{\rho}\frac{\partial \rho}{\partial s}\right) = -\frac{\partial}{\partial s}\left(\frac{u_s}{R}\right) - \frac{\gamma}{a^2}\frac{u_s^2}{R}\frac{\partial u_s}{\partial s}$$ (4.41)

The source term and the coefficient of the normal derivative of u_s are known functions of s from the CFD analysis. Hence, this equation can be solved for the normal derivative of u_s with a periodic boundary condition. Consequently, normal derivative of density can be found by substituting for the normal derivatives of pressure and tangential velocity in Eq. (4.40).

4.5 Sensitivity with Surface Parameterization

A non-parametric geometry definition requires the surface mesh coordinates. Although this approach utilizes the readily available data, it increases the number of design variables. On the other hand, a parametric geometry definition reduces the number of design variables, since the number of control points is significantly less than the surface mesh points. In the present approach, a mth degree Bezier curve representation is used,

$$\bar{R}(t) = \sum_{i=0}^{m} B_i^m(t)\bar{P}_i, \quad \tau \in [0,1]$$

(4.42)

where $\bar{P}_i$ is the ith control point and $\bar{R}(t)$ is the position vector of a point on the curve. The Bernstein polynomials are defined as:

$$B_i^m(t) = \binom{m}{i} t^i (1-t)^{m-i} = \frac{m!}{i!(m-i)!} t^i (1-t)^{m-i}$$

(4.43)

The design vector at an arbitrary point lying on the control surface can now be defined as the change in its coordinates as the Bezier control points are perturbed.

$$\bar{V} = \sum_{i=0}^{m} B_i^m(t)\bar{P}_i' = \sum_{i=0}^{m} B_i^m(t)\binom{X_i'}{Y_i'}$$

(4.44)

In sensitivity analysis, it is often required to find the design derivative of geometric quantities such as the unit normal and the element of arc length. If the unit tangential and normal vectors are given by

$$\hat{t} = \left(\frac{\dot{x}}{\sqrt{\dot{x}^2 + \dot{y}^2}} \quad \frac{\dot{y}}{\sqrt{\dot{x}^2 + \dot{y}^2}}\right)^T \quad , \quad \hat{n} = \left(\frac{\dot{y}}{\sqrt{\dot{x}^2 + \dot{y}^2}} \quad \frac{-\dot{x}}{\sqrt{\dot{x}^2 + \dot{y}^2}}\right)^T$$

(4.45)

Eq. (4.26) relates the design derivative of the unit normal to the perturbation of the angle θ between the unit tangent and the positive x-axis. θ can be written as:

$$\theta = tan^{-1}\left(\frac{\dot{y}}{\dot{x}}\right)$$

(4.46)

Differentiating Eq. (4.46) with respect to the design variables and substituting for θ' in Eq. (4.26) yields

$$\dot{\hat{n}} = \theta'\hat{t} = \frac{\dot{y}'\dot{x} - \dot{x}'\dot{y}}{\dot{x}^2 + \dot{y}^2}\hat{t} .$$

(4.47)

The design derivative of the components of the unit normal can now be written explicitly as:

$$n_x' = \frac{n_x n_y}{\sqrt{\dot{x}^2 + \dot{y}^2}} \sum_{i=0}^{m} \frac{dB_i^m}{dt} X_i' + \frac{n_y^2}{\sqrt{\dot{x}^2 + \dot{y}^2}} \sum_{i=0}^{m} \frac{dB_i^m}{dt} Y_i'$$

$$n_y' = \frac{-n_x^2}{\sqrt{\dot{x}^2 + \dot{y}^2}} \sum_{i=0}^{m} \frac{dB_i^m}{dt} X_i' - \frac{n_x n_y}{\sqrt{\dot{x}^2 + \dot{y}^2}} \sum_{i=0}^{m} \frac{dB_i^m}{dt} Y_i'$$

(4.48)

It is quite interesting to notice that the term $\rho u_s \theta'$ in Eq. (4.33) further simplifies to

$$\rho u_s \theta' = \frac{\rho u \sum_{i=0}^{m} \frac{dB_i^m}{dt} Y_i' - \rho v \sum_{i=0}^{m} \frac{dB_i^m}{dt} X_i'}{\sqrt{\dot{x}^2 + \dot{y}^2}} .$$

(4.49)

Starting from Eq. (3.9), the design derivative of the element of the arc length for a Bezier- Bernstein representation can be easily shown to have the following form:

$$|\dot{\overline{\delta x}}| = \frac{\dot{\overline{\delta x}} \cdot \overline{\delta x}}{|\overline{\delta x}|} = \left(\frac{\partial v_t}{\partial s} - \frac{v_n}{R}\right)|\overline{\delta x}| = \frac{\dot{x} \sum_{i=0}^{m} \frac{dB_i^m}{dt} X_i' + \dot{y} \sum_{i=0}^{m} \frac{dB_i^m}{dt} Y_i'}{\dot{x}^2 + \dot{y}^2}$$

(4.50)

Finally, the sensitivity equation, i.e. the variation of the cost functional with respect to the y-coordinate of the Bezier control points, is obtained by incorporating Eqs. (4.44) - (4.50) into Eq. (4.33):

$$\frac{\partial I}{\partial Y_i} = -\int_0^1 \Pi Q_2 \frac{dB_i^m}{dt}\, dt$$

$$-\int_0^1 \Pi \frac{B_i^m}{\sqrt{\dot{x}^2 + \dot{y}^2}}\left[\frac{\dot{x}\ddot{y} - \ddot{x}\dot{y}}{\left(\dot{x}^2 + \dot{y}^2\right)^{\frac{3}{2}}}\dot{y}(Q_2\dot{x} + Q_3\dot{y}) + \dot{x}\frac{\partial(\rho u_s)}{\partial s}\right] dt \qquad (4.51)$$

$$+\int_0^1\left(\frac{\partial f}{\partial n}B_i^m\sqrt{\dot{x}^2 + \dot{y}^2} - f\frac{\dot{x}\ddot{y} - \ddot{x}\dot{y}}{\dot{x}^2 + \dot{y}^2}B_i^m\right) dt$$

In the above, $\Pi = \lambda_1 + u\lambda_2 + v\lambda_3 + H\lambda_4$.

4.6 Solving State and Adjoint Equations

The state equation Eq. (4.1) is first expressed in the integral form for a bounded domain Ω with a boundary Γ as:

$$\frac{\partial}{\partial t}\int_\Omega \vec{Q}\, d\Omega + \int_\Gamma \left(n_x A_i^T + n_y B_i^T\right)\cdot\vec{Q}\ d\Gamma = 0 \qquad (4.52)$$

Second-order spatial discretization for the present upwind scheme is accomplished by using Roe's flux-difference splitting. Cell-centered solutions are Taylor-series expanded to each of the faces of each triangular cell in the domain. The spatially discretized form of the governing equations are then integrated in pseudo-time using the explicit four-stage Runge-Kutta method. On the airfoil surface, the standard inviscid boundary conditions for the velocity is implemented: impermeable and velocity parallel to the wall.

In the farfield, Γ_o, characteristic boundary conditions are employed based on the locally one-dimensional Riemann-invariants.

For adapting the mesh to the boundary changes as the shape evolves, the tension-springs analogy is used, i.e., each edge of a triangle is represented by a tension spring. Assuming that the spring stiffness is inversely proportional to the edge length, the equilibrium of the composite spring forces provides the displacement of each node. To restrict the size of the adaptation region, a window is created around a boundary being reshaped. The entire domain is searched to locate the window nodes and the window frame nodes. Then, the window nodes are allowed to be adapted, but the nodes exterior to the window and the window frame nodes are spatially fixed.

The adjoint (co-state) equation, Eq. (4.13), is of the same order and form as the flow equations. Hence, it is desirable to discretize and solve for the Lagrange variable vector, $\vec{\lambda}$, by the same CFD scheme used for the state equations. However, to facilitate this pseudo-time marching scheme, a pseudo-time term is added:

$$\frac{\partial \vec{\lambda}}{\partial t} - A^T \vec{\lambda}_x - B^T \vec{\lambda}_y = 0 \qquad (4.53)$$

Assuming that the flux Jacobeans are constant over the volume of a cell, the discrete form of Eq. (4.53) for cell i, can be written as:

$$\frac{\Delta \Omega_i}{\Delta t} \left(\vec{\lambda}_i^{n+1} - \vec{\lambda}_i^n \right) - \int_\Gamma \left(n_x A_i^T + n_y B_i^T \right) \cdot \vec{\lambda}\, ds = 0 \qquad (4.54)$$

If the Jacobian matrix associated with direction $\hat{n}$ is denoted by

$$n_x A_i^T + n_y B_i^T = \overline{A}\left(\vec{Q}_i ; \hat{n} \right) \qquad (4.55)$$

then the cell boundary term of Eq. (4.55) can be rewritten as

$$\int_{\Gamma} \left(n_x A_i^T + n_y B_i^T \right) \cdot \bar{\lambda} \, ds = \sum_{j \in N_i} G_{ij} l_{ij} \tag{4.56}$$

where l_{ij} is the side of cell i lying between the cell i and the neighboring cell j, and G_{ij} for a cell centered scheme can be written as:

$$G_{ij} = \tfrac{1}{2} \left(\overline{A} \left(\bar{Q}_i ; \hat{n} \right) \left(\bar{\lambda}_l + \bar{\lambda}_r \right) + \left| \tilde{A} \right|^T \left(\bar{\lambda}_r - \bar{\lambda}_l \right) \right) \tag{4.57}$$

$\left| \tilde{A} \right|$ is the Jacobian matrix evaluated at the Roe state and the left and right values are cell quantities extended to the sides by the Taylor series expansion around the cell center. The solution is then advanced in psuedo-time using an explicit four stage Runge-Kutta scheme until convergence to some tolerance.

4.7 Optimization

The gradient-based and constrained optimization method of Kreisselmeier-Steinhauser (1979), as coded in KSOPT and based on the work of Wrenn (1989), is used in this work. This method converts all the equality constraints into a set of inequality constraints, then it combines the objective function and all the inequality constraints into one composite KS function. At this point, a sequential unconstrained minimization technique (SUMT) is used. The particular choice herein is the Davidson-Fletcher-Powell (DFP) search algorithm for the uni-variate search direction and the optimum step size. Although not used here in this work, this method can handle multiple objective functions.

Chapter 5

Limit-Cycle Shape Optimization Using Unsteady Transonic Small Disturbance Equation (UTSD)

Most of the research work in the field of aerodynamic optimization has been conducted for steady flows and the resulting steady aerodynamic loads. In numerous applications, however, the flow is unsteady, which necessitates the analysis equations to include the time dependent terms.

In this chapter, unsteady compressible flows are considered. The analytical sensitivities with respect to the shape are derived using the continuous adjoint approach. The approach is identical to that of Chapter 4, but the sensitivity equation, the adjoint equations and their boundary conditions now include time-dependent terms. This has direct implications on practically every step of a shape optimization methodology, but in particular, the derivation of the analytical sensitivities. With regard to the validity of the formulation for shocked flows, the reader is referred to the concluding paragraph of the introduction to Chapter 4. The derivation is discussed in detail next.

5.1 MATHEMATICAL MODEL

5.1.1 State Equations and Boundary Conditions

The flow is governed by the *modified UTSD* equation, which may be written in the conservation form as

$$\frac{\partial f_0}{\partial t} + \frac{\partial f_1}{\partial x} + \frac{\partial f_2}{\partial y} = 0 \qquad (5.1)$$

where f_0, f_1 and f_2 are defined as

$$f_0 = -B\varphi_x - A\varphi_t \ , \ f_1 = C\varphi_x + D\varphi_x^2 \ , \ f_2 = \varphi_y \qquad (5.2)$$

and constants A, B, C, D are given by:

$$A = M^2, \ B = 2M^2, \ C = 1 - M^2, \ D = -\frac{1}{2}(\gamma+1)M^m. \qquad (5.3)$$

In these equations, t denotes time and x and y are the freestream and stream normal coordinates. The disturbance velocity potential is denoted by φ, M is the freestream Mach number. The exponent m is a function of M chosen to adjust the critical pressure coefficient to match the exact isentropic critical pressure.

Under the assumptions of the small-disturbance theory, the wall and wake boundary conditions can be transferred to the x-axis by performing a Taylor series expansion. The imposed boundary conditions for *low frequency oscillations* of a pitching airfoil about position $x = x_p$ in the Cartesian plane are given by:

Far upstream	$\varphi = 0;$	(5.4a)
Far downstream	$\varphi_x = 0;$	(5.4b)
Far above and below	$\varphi_y = 0;$	(5.4c)
Wake	$[\varphi] = \Gamma, \quad [\varphi_y] = 0, \quad [\varphi_x+\varphi_t] = 0;$	(5.4d)
Subsonic trailing edge	$[C_p] = 0;$	(5.4e)
Oscillating airfoil surface		

$$\varphi_y\big|_{u,l} = \frac{\partial}{\partial x} F_{u,l} - (\alpha_0 + \alpha_a \sin \kappa t) - \kappa\alpha_a(x - x_p)\cos \kappa t \qquad (5.4f)$$

The upper and lower surfaces are denoted by $F_{u,l}(x)$. κ denotes the reduced frequency based on the freestream velocity and chord length. The nondimensional time and circulation are denoted by t and Γ respectively.

5.1.2 Computational Domain and Transformation

It is desirable to cluster the grid points near the airfoil and place the farfield boundaries as far as possible from the source of disturbance. As the physical domain is rectangular, this can be easily achieved by stretching the mesh independently in the x and y directions. Mesh spacing in the x-direction is uniform on the airfoil and increases exponentially away from the body. It is of prime importance to make sure that the metrics are *continuous* throughout the domain. In the y-direction, the mesh is clustered symmetrically about the x-axis as depicted in Figure 5.1.
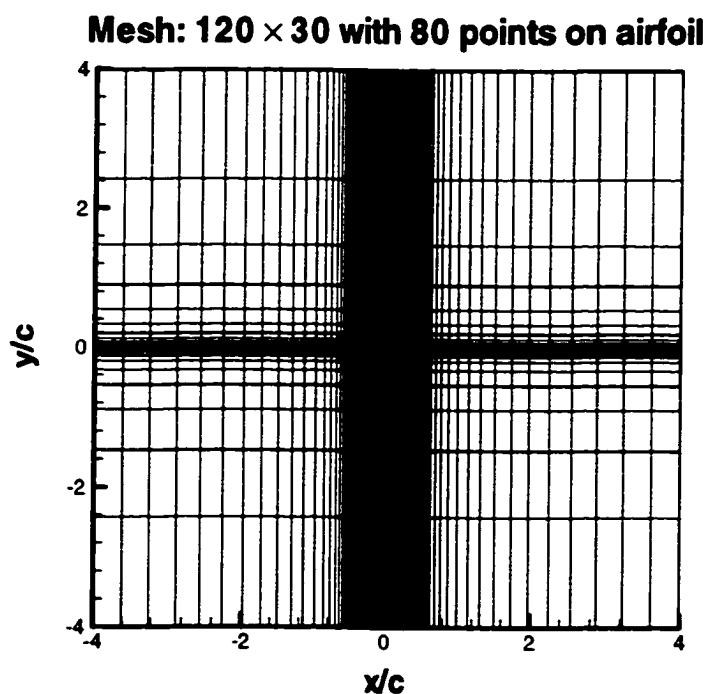
Mesh: 120 × 30 with 80 points on airfoil

Figure 5.1 Clustered grid for transonic flow past an airfoil

With transformations $t = t$, $x = x(\xi)$, and $y = y(\eta)$, the governing equation can be recast in the ξ-η plane as:

$$\frac{\partial}{\partial t}\left(-A\varphi_t - B\varphi_\xi\xi_x\right) + \frac{\partial}{\partial\xi}\left(E\varphi_\xi\xi_x + F\varphi_\xi^2\xi_x^2\right)\xi_x + \frac{\partial}{\partial\eta}\left(\varphi_\eta\eta_y\right)\eta_y = 0 \qquad (5.5)$$

The boundary conditions in the ξ-η plane are found by applying the chain rule to the boundary conditions stated earlier (Eqs. 5.4 a-f).

5.1.3 Discretization and Linearization

For a cell Ω of width $d\xi$ and height $d\eta$ in the $\xi\eta$-plane, one can write

$$\int_\Omega \left\{ \frac{\partial}{\partial t}\left(-A\varphi_t - B\varphi_\xi\xi_x\right) + \frac{\partial}{\partial\xi}\left(C\varphi_\xi\xi_x + D\varphi_\xi^2\xi_x^2\right)\xi_x + \frac{\partial}{\partial\eta}\left(\varphi_\eta\eta_y\right)\eta_y \right\} x_\xi\, y_\eta\, d\xi\, d\eta = 0.$$

$$(5.6)$$

The term $x_\xi\, y_\eta$ is the Jacobian of the transformation. It represents the ratio of the elemental area $dxdy$ to the area of its image in the ξ-η plane. The integral over space can be transferred to the boundaries of the cell via the Green's theorem. After some algebraic manipulations, Eq. (5.6) takes the following form:

$$\frac{(\Delta\eta)^2}{\eta_y\big|_{j+1/2}}\left[A\varphi_n + B\phi_{\xi t}\xi_x\right]_{i,j} - \left[\Delta\eta\varphi_\eta\eta_y\right]_{j-1/2}^{j+1/2} +$$

$$\left(\frac{\Delta\eta}{\Delta\xi}\right)^2\left(\frac{\xi_x\big|_{i+1/2}}{\eta_y\big|_{j+1/2}}\right)\left[-D\left(\varphi_\xi\xi_x\big|_{i+1/2} + \varphi_\xi\xi_x\big|_{i-1/2}\right) - C\right]\left[\Delta\xi\varphi_\xi\xi_x\right]_{i-1/2}^{i+1/2} = 0. \quad (5.7)$$

At this stage, Eq. (5.7) is linearized by letting $\varphi^{n+1} \cong \varphi^* + \varphi'$, where φ^* is an approximation to φ^{n+1} and φ' will approach zero as $\varphi^* \to \varphi^{n+1}$. Then, the time derivative is discretized using second order backward differences, the ξ-derivative in the time dependent term is backward differenced for stability reasons, and other spatial derivatives in ξ are discretized according to the Murman-Cole switch as explained in Murman and Cole (1971). Central differencing is employed for all η-derivatives. Consequently, Eq. (5.7) results in a form for which the left hand side is,

$$\mathbf{LHS} = \frac{3}{2} B \Xi \frac{(\Delta \xi)^2}{\Delta t} \varphi_\xi' \Big|_{i,j}^{n+1} + 2A\Xi \frac{\varphi_{i,j}'}{\xi_x|_{i+1/2}} \left(\frac{1}{\Delta t}\right)^2 + \varphi_\xi' \xi_x \Big|_{i+1/2,j}^{n+1} \Xi \left[-2D\Delta\xi\varphi_\xi^* \xi_x \Big|_{i+1/2,j}^{n} - C \right]$$

$$- \varphi_\xi' \xi_x \Big|_{i-1/2,j}^{n+1} \Xi \left[-2D\Delta\xi\varphi_\xi^* \xi_x \Big|_{i-1/2,j}^{n} - C \right] - \left[\Delta\eta\varphi_\eta'\eta_y\right]_{j-1/2}^{j+1/2}$$

(5.8a)

where $\Xi = \left(\dfrac{\Delta\eta}{\Delta\xi}\right)^2 \dfrac{\xi_x|_{i+1/2}}{\eta_y|_{j+1/2}}$ and the right hand side of this equation is simply the discretized UTSD equation.

$$\mathbf{RHS} = -B\Xi \frac{(\Delta\xi)^2}{2\Delta t} \left[3\varphi_\xi^* - 4\varphi_\xi^n + \varphi_\xi^{n-1}\right]_{i,j} - \frac{A\Xi}{\xi_x|_{i+1/2}} \left(\frac{1}{\Delta t}\right)^2 \left[2\varphi^* - 5\varphi^n + 4\varphi^{n-1} - \varphi^{n-2}\right]_{i,j}$$

$$- \Xi \left[-D\left(\varphi_\xi^* \xi_x \Big|_{i+1/2} + \varphi_\xi^* \xi_x \Big|_{i-1/2}\right) - C \right]_{j+1/2} \cdot \left[\Delta\xi\varphi_\xi^* \xi_x\right]_{i-1/2}^{i+1/2} + \left[\Delta\eta\varphi_\eta^*\eta_y\right]_{j-1/2}^{j+1/2}$$

(5.8b)

As $\varphi^{n+1} = \varphi^* + \varphi'$, the boundary conditions are enforced on both φ^* and φ' to ensure that at the end of each time step, φ will satisfy the stated boundary conditions. The nonhomogenous part of each boundary condition is implemented on the RHS, while

the homogeneous part is applied through the LHS. For instance, the wake boundary is treated with the following jump conditions:

$$[\varphi^{\bullet}] = \Gamma , \quad [\varphi^{\bullet}_{\eta}] = 0 , \quad [\varphi^{'}] = 0 , \quad [\varphi^{'}_{\eta}] = 0 \qquad (5.9)$$

The continuity of the η-derivative across the wake can be utilized to find

$$\varphi_{\eta}\Big|_{\xi=0^{\pm}} = \frac{\varphi_{i,\frac{1}{2}} - \varphi_{i,-\frac{1}{2}} - \Gamma(\xi,t)}{\Delta \eta} \qquad (5.10)$$

where the circulation, Γ, is lagged in time. Continuity of pressure across the wake can be written as an advection equation for the circulation, i.e. $\Gamma_x + \Gamma_t = 0$. This equation is integrated from the trailing edge to the downstream boundary to solve for Γ along the wake. Γ_x is second order upwind differenced, whereas first order backward difference is used for the time derivative. Starting with the new value of $\Gamma(x=x_{TE})$ after the completion of each iteration, one can obtain the new value of the circulation at downstream stations using the following:

$$\Gamma_i^{n+1} = \frac{4\Gamma_{i-1}^{n+1} - \Gamma_{i-2}^{n+1} + \frac{2\Delta\xi}{\xi_x\Delta t}\Gamma_i^n}{3 + \frac{2\Delta\xi}{\xi_x\Delta t}} \qquad (5.11)$$

The flow tangency boundary condition is imposed within the differencing of $\varphi_{\eta}^{\bullet}$ and $\varphi_{\eta}^{'}$ terms on the ξ-axis. Far downstream, $\varphi_{\xi}^{\bullet}$ is computed by second order backward differencing and the boundary condition is simply satisfied by putting $\varphi_{\xi}^{\bullet} + \varphi_{\xi}^{'} = 0$. A similar procedure is applied at the far upstream boundary.

The reader is referred to Caughey (1982), Goorjian and Van Buskirk (1985) and Batina (1988) for further information on the different solution strategies used for the UTSD equation.

5.1.4 Resolution scheme

Eq. (5.8), when written for all the grid points, is a set of linear equations in terms of φ' which needs to be solved at each sub-iteration to update φ^*. These sub-iterations are required to achieve time accuracy. For steady calculations, time accuracy is not an issue and sub-iterations are not used. The unknowns at the cell centers are packed in the η-direction according to $\varphi_k = \varphi_{(i-1)N+j}$, N being the number of divisions in the η-direction. The nonzero elements are confined within a band formed by diagonals parallel to the main diagonal. As the computational stencil of a supersonic cell (i, j) contains four points in the ξ-direction, there are at most six nonzeros on the kth row of the coefficient matrix. Hence, the maximum bandwidth is 3N. The resulting banded matrix is solved efficiently by the public-domain software LAPACK. The importance of mesh stretching becomes transparent in light of the fact that the number of calculations grows rapidly with increasing bandwidth and, consequently, efficiency deteriorates dramatically. Hence, one needs to use highly stretched meshes in the η-direction to reduce the bandwidth without sacrificing accuracy.

5.2 Optimization Problem

5.2.1 Continuous Adjoint Equations

The problem we consider is the design of the shape of a *pitching airfoil* that attains a prescribed velocity potential distribution $\varphi'(s, t)$ within the time period $[T_1, T_2]$. The freestream Mach number, M_∞, and the reduced frequency of oscillation, κ, are fixed. This problem can be cast into an optimization problem, where it is required to minimize the following cost functional:

$$I_C = \int\limits_{T_1}^{T_2} \int\limits_{U,L} [\phi(s,t) - \phi'(s,t)]^2 \, ds \, dt \tag{5.12}$$
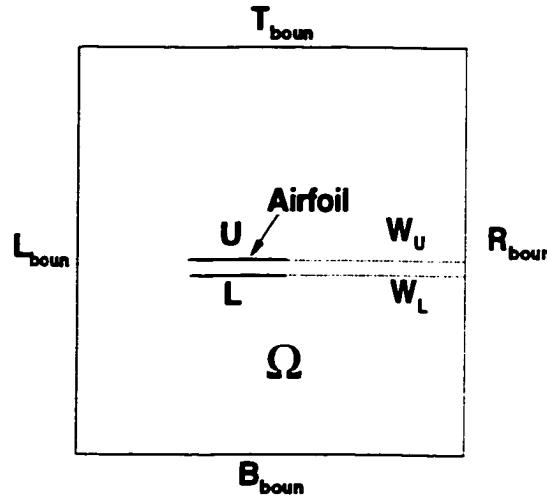

Figure 5.2 Boundaries of the computational domain.

Abbreviations used for the different segments of the boundary are shown in Figure. 5.2. The cost functional I_C is augmented with the weak form of the state equations.

$$I_R = \int\limits_{T_1}^{T_2} \int\limits_{\Omega} \left\{ -\frac{\partial}{\partial t}(A\phi_t + B\phi_x) \right\} \lambda \, d\Omega dt +$$

$$\int\limits_{T_1}^{T_2} \int\limits_{\Omega} \left\{ \frac{\partial}{\partial x}(C\phi_x + D\phi_x^2) + \frac{\partial}{\partial y}\phi_y \right\} \lambda \, d\Omega dt + \int\limits_{T_1}^{T_2} \int\limits_{W} (\Gamma_t + \Gamma_x) \psi \, ds \, dt \tag{5.13}$$

The arbitrary weighting functions, $\lambda(x,y,t)$ and ψ $(x > x_{TE},0,t)$, are the adjoint variables. One can use integration by parts to transfer the derivative operator with respect to time and space to the adjoint variable and arrive at the following for the first variation of I_R with respect to the boundary:

$$
\begin{aligned}
I'_R = & \int_{T_I\Omega}^{T_2} \int \{-(A\lambda_t + B\lambda_x)_t + (C\lambda_x + 2D\phi_x\lambda_x)_x + \lambda_{yy}\}\phi' d\Omega dt + \\
& \int_{T_I}^{T_2}\left\{-\int_{R_{boun}}(C+2D\phi_x)\lambda_x\phi' ds + \int_{L_{boun}}(C+2D\phi_x)\lambda_x\phi' ds\right\}dt \\
& + \int_{T_I}^{T_2}\left\{-\int_{T_{boun}}\lambda_y\phi' ds + \int_{B_{boun}}\lambda_y\phi' ds\right\}dt + \int_{T_I}^{T_2}\left\{\int_{W_U\cup U}(\lambda_y\phi' - \phi'_y\lambda) ds\right\}dt \\
& + \int_{T_I}^{T_2}\left\{\int_{W_L\cup L}(\phi'_y\lambda - \lambda_y\phi') ds - \int_{L_{boun}}(C\phi'_x + 2D\phi_x\phi'_x)\lambda ds\right\}dt \\
& + \int_{T_I}^{T_2}\int_{R_{boun}}B\phi'\lambda_t ds dt - \int_{T_I}^{T_2}\int_W(\psi_x + \psi_t)\Gamma' ds dt + \int_{T_I}^{T_2}[\Gamma'\psi]_{x_{TE}}^{\infty} dt \\
& - \int_\Omega [A\phi'_t\lambda + B\phi'_x\lambda - A\phi'\lambda_t]_{T_I}^{T_2} d\Omega + \int_W [\Gamma'\psi]_{T_I}^{T_2} ds
\end{aligned}
$$

(5.14)

In Eq. (5.14), ϕ' denotes the perturbation in the disturbance potential due to a slight change in the shape of the boundary. Let's denote the time at which the initial transient dies out and the limiting periodic motion starts by t_p. The last two terms in Eq. (5.14) involve $\phi'(x,y)$ at $t = T_1,T_2$ and can be omitted from I'_R if and only if ϕ $(x,y,T_1) = \phi$ (x,y,T_2). In other words, T_1 should be greater than t_p and T_2-T_1 should be an integer multiple of the period of oscillation $2\pi/\kappa$. Eq. (5.14) can be further simplified if the adjoint variable satisfies the following:

$$-A\lambda_{tt} - B\lambda_{tx} + \left(C\lambda_x + 2D\phi_x\lambda_x\right)_x + \lambda_{yy} = 0 \quad \forall \vec{x} \in \Omega$$

$$\lambda_x = 0 \quad \forall \vec{x} \in R_{boun}$$

$$\lambda_y = 0 \quad \forall \vec{x} \in T_{boun} \cup B_{boun} \tag{5.15}$$

$$\lambda = 0 \quad \forall \vec{x} \in L_{boun}$$

$$\begin{cases} \lambda_L = \lambda_U \;, \; \lambda_y\big|_U = \lambda_y\big|_L \\ \quad \psi_x + \psi_t = \lambda_y \qquad \forall t, \vec{x} \in W_U \cup W_L \\ \quad \psi(t, \infty) = 0 \end{cases}$$

Subsequently, the first variation of the augmented cost functional can be written as:

$$I' = I'_C + I'_R = \int_{T_1}^{T_2} \int_{U \cup L} \left(\phi - \phi^t\right)\phi' ds\, dt + \int_{T_1}^{T_2}\left\{\int_U \phi'\lambda_y \, ds - \int_L \phi'\lambda_y \, ds\right\} dt$$

$$+ \int_{T_1}^{T_2}\int_L \frac{\partial F_L}{\partial x}' \lambda\, ds\, dt - \int_{T_1}^{T_2}\int_U \frac{\partial F_u}{\partial x}' \lambda\, ds\, dt + \int_{T_1}^{T_2} \Gamma'\psi\big|_{x=x_{TE}}\, dt \tag{5.16}$$

To eliminate the remaining perturbations of the disturbance potential, one can rewrite the last term in Eq. (5.16) using the Dirac delta notation, $\delta\,(x\text{-}x_{TE})$, as:

$$\int_{T_1}^{T_2} \Gamma'\psi\big|_{x=x_{TE}}\, dt = \int_{T_1}^{T_2}\int_U \phi'\psi\big|_{x=x_{TE}}\, \delta(x - x_{TE})dx\,dt - \int_{T_1}^{T_2}\int_L \phi'\psi\big|_{x=x_{TE}}\, \delta(x - x_{TE})dx\,dt$$

$$\tag{5.17}$$

Consequently, the wall boundary condition is found as:

$$\lambda_y + \left(\phi - \phi_u^t\right)\!-\delta(\,x - x_{TE}\,)\psi\big|_{x=x_{TE}} = 0 \qquad \forall t, \vec{x} \in U$$

$$\lambda_y - \left(\phi - \phi_l^t\right)\!-\delta(\,x - x_{TE}\,)\psi\big|_{x=x_{TE}} = 0 \qquad \forall t, \vec{x} \in L \tag{5.18}$$

However, if one chooses to use the more relevant cost functional

$$I_C(\phi, \vec{X}_D) = \frac{1}{2}\int_{T_1}^{T_2} \int_{U,L} \left[\phi_x(s,t) - \phi_x^t(s,t)\right]^2 ds\, dt \tag{5.19}$$

the wall boundary condition becomes

$$\lambda_y - \left(\phi_{xx} - \phi_{xx}^t\right) - \delta(x - x_{TE})\left[\psi\big|_{x=x_{TE}} - \left(\phi_x^{TE} - \phi_x^{t\,TE}\right)\right]$$

$$- \delta(x - x_{LE})\left[\phi_x^{LE} - \phi_x^{t\,LE}\right] = 0 \qquad \forall t, \bar{x} \in U$$

(5.20)

$$\lambda_y + \left(\phi_{xx} - \phi_{xx}^t\right) - \delta(x - x_{TE})\left[\psi\big|_{x=x_{TE}} + \left(\phi_x^{TE} - \phi_x^{t\,TE}\right)\right]$$

$$+ \delta(x - x_{LE})\left[\phi_x^{LE} - \phi_x^{t\,LE}\right] = 0 \qquad \forall t, \bar{x} \in L$$

Eq. (5.16) for the first variation of the objective cost functional reduces to

$$I' = \int_{T_I}^{T_2}\int_L \left(\frac{\partial F_L}{\partial x}\right)' \lambda \, ds\, dt - \int_{T_I}^{T_2}\int_U \left(\frac{\partial F_u}{\partial x}\right)' \lambda \, ds\, dt$$

(5.21)

5.2.2 Resolution of Discrete Adjoint Equations

As the coefficients of the highest order derivatives appearing in Eq. (5.16) are only a function of space, the adjoint equation is linear in λ and the linearization step described in the discretization of the governing UTSD equation can be skipped. At any point (x, y) in the domain, the sign of $E+2F\phi_x$ determines whether the PDE is locally elliptic, hyperbolic, or parabolic. Central difference formulas can be used for the elliptic points while the discretization is upwind-biased at the hyperbolic points using the Murman-Cole switch. The discretization of the adjoint equation in the domain takes the following form in the computational domain (ξ, η):

$$\left(\frac{\xi_x|_{i+1/2}}{\eta_y|_{j+1/2}}\right)\left(\frac{\Delta\eta}{\Delta\xi}\right)^2 \left[C\Delta\xi\lambda_\xi^{n+1}\xi_x + 2D\Delta\xi\phi_\xi\lambda_\xi^{n+1}\xi_x^2\right]_{i-1/2}^{i+1/2} + \lambda_\eta^{n+1}\eta_y\Delta\eta\Big|_{j-1/2}^{j+1/2} -$$

$$\frac{\Delta\eta}{\eta_y|_{j+1/2}}\left[A\frac{2\lambda^{n+1} - 5\lambda^n + 4\lambda^{n-1} - \lambda^{n-2}}{\Delta t^2} + B\frac{3\lambda_\xi^{n+1} - 4\lambda_\xi^{n+1} + \lambda_\xi^{n+1}}{2\Delta t}\xi_x^{i+1/2}\right] = 0.$$

$$(5.22)$$

However, λ is related to the wake Lagrange variable, ψ, by the nonhomogenous linear convection equation

$$\begin{cases} \psi_x + \psi_t = \lambda_y \\ \psi(t,\infty) = 0 \end{cases} \qquad (5.23)$$

Hence at each time step, Eqs. (5.22) and (5.23) need to be resolved simultaneously by some iterative procedure. In the present work, successive over-relaxation is used to update the λ's. The process is continued until the L_2-norm of the difference between two consecutive iterations falls below some tolerance, ε, currently taken as 10^{-8}. The numerical representation of the Dirac delta function and its impact on the accuracy of the sensitivity derivatives will be discussed in Chapter 8. Also in Chapter 8, after validating the unsteady flow analysis and unsteady sensitivity analysis components, the overall methodology will be demonstrated for a stationary airfoil and for an airfoil performing a sinusoidal pitching oscillation.

Chapter 6

Continuous Adjoint Sensitivities of Helmholtz Equation

In this chapter, the method of continuous adjoint sensitivity analysis is applied to an acoustic diffraction problem. The acoustic phenomena in a stationary fluid medium can be modeled by the wave equation. The time dependency is alleviated by applying the method of *normal modes*, whereby the noise source is resolved into modes, which may be treated separately due to the linearity of the governing wave equation. As such, the wave equation is transformed into a complex elliptic Helmholtz equation with boundary conditions of the Dirichlet, Neumann, or Sommerfeld radiation (Robin) type imposed over the whole boundary. There is a trade-off between time dependency and switching from the real to the complex domain. In this chapter, it is intended to obtain the shape sensitivity derivatives of an acoustic pressure field. This problem is not only very interesting mathematically, but has practical applications as well. Noise pollution in populated urban areas is a major problem that has resulted in a dramatic increase of academic interest in the development of computational techniques for noise propagation simulations and design of noise reducing disposals (e.g. Harris (1992) and Piacentini (1996)). One of the most effective noise reducing disposals are optimally shaped and placed barriers on the side of highways, railroads, airports, and industrial buildings. Height, shape, position relative to the noise source, and surface properties determine the effectiveness of such barriers. However, aesthetic, architectural, and economic constraints on the size of barriers result in a very small feasible design space. Under such

circumstances, accurate sensitivity information is essential for a successful search for a better design.

In this chapter, it will be demonstrated that the shape sensitivity derivatives of any general objective functional involve the first and second order directional derivatives of the acoustic pressure field on the control surface. Hence, it is essential to ensure that these derivatives are computed quite precisely. The sensitivity derivatives will be derived in two different coordinate systems and compared for relative accuracy.

6.1 Mathematical Model

The wave equation can be easily obtained from the linearized Euler equations with zero mean flow by adding the derivative of the x-component of the momentum equation with respect to x and the y- derivative of the y- momentum equation. The wave equations is given by:

$$\frac{\partial^2 P}{\partial t^2} = a_0^2 \nabla^2 P + S(\bar{x}, t) \tag{6.1}$$

where P is the acoustic pressure and $S(\bar{x}, t)$ is a time-dependent source. a_0 is the velocity of sound in the medium, i.e., the velocity at which small amplitude acoustic waves propagate. As this equation is linear in its dependent variable, the pressure field and the source term can be resolved into their harmonics, with the obvious advantage of being able to study each harmonic component separately. The harmonic time dependence can be exploited to write

$$P = p(\bar{x})e^{i\omega t} + \overline{p(\bar{x})}e^{-i\omega t}$$
$$S(\bar{x}, t) = \delta(\bar{x}_s)e^{i\omega t} + \delta(\bar{x}_s)e^{-i\omega t} \tag{6.2}$$

in which the bar denotes the complex conjugate and a point source generating spherical acoustic waves at frequency ω is represented using a Dirac delta function centered at $\bar{x}_s$, the position of the source. Substitution of Eq. (6.2) in Eq. (6.1), yields the Helmholtz equation

$$\nabla^2 p(\bar{x}) + k^2 p(\bar{x}) = \delta(\bar{x}_S) \tag{6.3}$$

$k = \omega/a_0$ is the acoustic wave number. In the farfield, p must satisfy the Sommerfeld radiation boundary condition:

$$\lim_{r \to \infty} r\left\{\frac{\partial p}{\partial r} - ikp\right\} = 0 \tag{6.4}$$

The boundary condtion imposed on a solid wall reflects its physical properties: homogenous Neumann condition for rigid perfectly reflecting surfaces, homogenous Dirichlet for non-reflecting walls, and Robin condition with complex coefficients for absorbing walls.

The particular problem considered in this paper is the diffraction of 2-D acoustic waves by a barrier placed on an infinite perfectly reflecting ground. As the ground extends to infinity from both directions, it can be removed from the computational model and an equivalent infinite-domain problem can be solved by including the images of the noise source and the barrier with respect to the plane of the ground in the model (Figure 6.1). Consequently, Eq. (6.3) is modified as:

$$\nabla^2 p(\bar{x}) + k^2 p(\bar{x}) = \delta(\bar{x}_S) + \delta(\bar{x}_{S'}) \tag{6.5}$$

Figure 6.1 is a schematic of a barrier located on an infinite rigid ground. The barrier, ground, farfield and design surfaces are denoted by Γ, G, O, and D respectively.
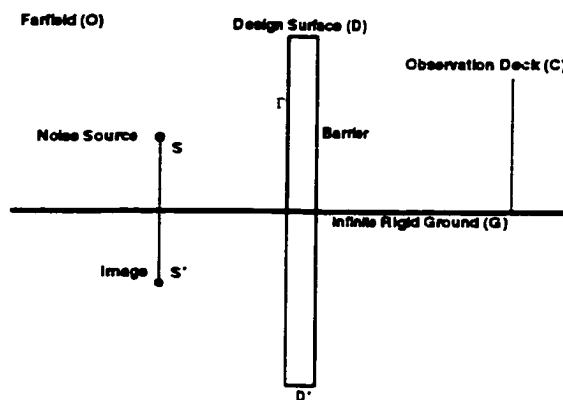
Figure 6.1 Barrier on an infinite rigid ground

6.2 Optimization Problem

The process of searching for an optimal design configuration requires accurate sensitivity information. The objective is to find the design configuration that minimizes a measure of sound intensity on some contour C. Choosing the time average of the square of $p(t)$ as a suitable measure of the acoustic field, the cost functional of the equivalent minimization problem can be written as:

$$I_C = \frac{1}{2} \int_C \left(p^2 \right)_{av}^{\;2} ds = \frac{1}{2} \int_C \left(\frac{1}{2} p\bar{p} \right)^2 ds \qquad (6.6)$$

6.2.1 First Variation of Cost Functional

In Eq. (6.6), I_C is not an analytical function in p as it involves the complex conjugate of the acoustic pressure field. Hence, variation in I_C cannot be written only in terms of the complex pressure field and it is needed to write the variation explicitly in terms of the real and imaginary parts of p.

$$I_C = \int_C \left(\tfrac{1}{2}p\overline{p}\right)\left(p_r p_r' + p_i p_i'\right)ds$$

$$+ \int_C \left\{ \left(\tfrac{1}{2}p\overline{p}\right)\left(p_r \frac{\partial p_r}{\partial n} + p_i \frac{\partial p_i}{\partial n} \right) + \frac{\tfrac{1}{2}\left(\tfrac{1}{2}p\overline{p}\right)^2}{R} \right\}\left(\vec{V} \cdot \hat{n}\right)ds \tag{6.7}$$

The second integral in the above equation will simply vanish if the contour C is stationary in space. Also, the terms involving the normal derivatives of the pressure field vanish, as either the contour lies on the surface, where the boundary condition endorses a zero normal derivative, or the contour lies stationary in the domain, in which case $\vec{V} \equiv 0$.

6.2.2 First Variation of Augmented Functional

The real and imaginary parts of the governing Helmholtz equation are multiplied by arbitrary Lagrange multipliers, λ_r, λ_i, respectively and integrated over the whole domain Ω. Then using Eq. (2.20), the first variation of I_R can be written as:

$$I_R = \int_\Omega \lambda_r \left(\nabla^2 p_r' + k^2 p_r'\right)d\Omega + \int_\Omega \lambda_i \left(\nabla^2 p_i' + k^2 p_i'\right)d\Omega \tag{6.8}$$

Using the Green's second identity or symmetrical theorem, Eq. (6.8) can be cast in the following form:

$$I_R = \int_\Omega p_r' \left(\nabla^2 \lambda_r + k^2 \lambda_r\right)d\Omega + \int_\Omega p_i' \left(\nabla^2 \lambda_i + k^2 \lambda_i\right)d\Omega$$

$$+ \int_\Gamma \left(\lambda_r \frac{\partial p_r'}{\partial n} - p_r' \frac{\partial \lambda_r}{\partial n} \right)d\Gamma + \int_\Gamma \left(\lambda_i \frac{\partial p_i'}{\partial n} - p_i' \frac{\partial \lambda_i}{\partial n} \right)d\Gamma \tag{6.9}$$

Combining results of Eq. (6.7) and Eq. (6.9), the design derivative of the augmented cost functional becomes:

$$I = I_{C+}I_R = \int_C \left(\frac{1}{2}p\overline{p}\right)\left(p_r p_r' + p_i p_i'\right)ds$$

$$+ \int_C \frac{\frac{1}{2}\left(\frac{1}{2}p\overline{p}\right)^2}{R}\left(\vec{V}\cdot\hat{n}\right)ds$$

$$+ \int_\Omega p_r'\left(\nabla^2\lambda_r + k^2\lambda_r\right)d\Omega + \int_\Omega p_i'\left(\nabla^2\lambda_i + k^2\lambda_i\right)d\Omega$$

$$+ \int_\Gamma\left(\lambda_r\frac{\partial p_r'}{\partial n} - p_r'\frac{\partial\lambda_r}{\partial n}\right)d\Gamma + \int_\Gamma\left(\lambda_i\frac{\partial p_i'}{\partial n} - p_i'\frac{\partial\lambda_i}{\partial n}\right)d\Gamma$$

<div align="right">(6.10)</div>

6.2.3 Adjoint System Formulation

First, we focus our attention on the farfield boundary condition (Eq. 6.4). As the boundary at infinity is stationary, the perturbed boundary condition at infinity can be written

$$\lim_{r\to\infty} r\left\{\frac{\partial p_r'}{\partial n} + kp_i'\right\} = 0$$

$$\lim_{r\to\infty} r\left\{\frac{\partial p_i'}{\partial n} - kp_r'\right\} = 0$$

<div align="right">(6.11)</div>

Substituting Eq. (6.11) in Eq. (6.10) and looking for a suitable choice of the Lagrange multipliers that would eliminate p' from integrals over the farfield present in Eq. (6.10), it is not hard to show that the Lagrange variables should satisfy the following at the farfield:

$$\lim_{r\to\infty} r\left\{\frac{\partial\lambda_r}{\partial n} - k\lambda_i\right\} = 0$$

$$\lim_{r\to\infty} r\left\{\frac{\partial\lambda_i}{\partial n} + k\lambda_r\right\} = 0$$

<div align="right">(6.12)</div>

If the complex adjoint variable, λ, is defined as $\lambda = \lambda_r + i\lambda_i$, Eq. (6.12) can be written more compactly as:

$$\lim_{r \to \infty} r\left\{\frac{\partial \lambda}{\partial n} + ik\lambda\right\} = 0 \qquad (6.13)$$

Comparing Eqs. (6.4) and (6.13), it is interesting to note that the Sommerfield radiation boundary condition describes an outgoing wave at infinity while its adjoint counterpart requires an incoming wave structure for the adjoint variable.

Examination of Eq. (6.10) reveals that the formulation of the adjoint system depends on the location of the contour C. If C lies on the barrier surface, the governing adjoint in the domain will be homogenous while the Neumann boundary condition on the portion of the surface coinciding with C will be nonhomogenous. The opposite holds for C located in the domain Ω.

If C lies on the design surface, the top edge of the barrier, it is easy to show that the complex adjoint variable has to satisfy the following:

$$\nabla^2 \lambda + k^2 \lambda = 0 \qquad \forall \bar{x} \in \Omega$$

$$\frac{\partial \lambda}{\partial n} = 0 \qquad \forall \bar{x} \in \Gamma \cup G - D$$

$$\frac{\partial \lambda}{\partial n} - \left(\tfrac{1}{2} p\bar{p}\right)p = 0 \qquad \forall \bar{x} \in D \qquad (6.14a)$$

$$\frac{\partial \lambda}{\partial n} - ik\lambda = 0 \qquad \forall \bar{x} \in O$$

If C lies in the domain, the term arising from the variation of the cost functional is absorbed in the adjoint equation as a source term.

$$\nabla^2 \lambda + k^2 \lambda + \left(\tfrac{1}{2} p\bar{p}\right)p\delta_C = 0 \qquad \forall \bar{x} \in \Omega$$

$$\frac{\partial \lambda}{\partial n} = 0 \qquad \forall \bar{x} \in \Gamma \cup G \qquad (6.14b)$$

$$\frac{\partial \lambda}{\partial n} - ik\lambda = 0 \qquad \forall \bar{x} \in O$$

In Eq. (6.14b), the Dirac delta term δ_C is defined as:

$$\int_{\Omega} f\delta_C d\Omega = \int_C fds \qquad (6.15)$$

6.2.4 Sensitivity Derivatives

The sensitivity equation, Eq. (6.10) reduces to

$$i = \int_D \left(\lambda_r \frac{\partial p_r'}{\partial n} + \lambda_i \frac{\partial p_i'}{\partial n} \right) d\Gamma + \int_C \left\{ \frac{\frac{1}{2}\left(\frac{1}{2} p\bar{p}\right)^2}{R} \right\} (\vec{V} \cdot \hat{n}) ds \qquad (6.16)$$

At this stage, one needs to find the material derivative of the boundary condition prescribed on the design surface. This would allow us to write $\dfrac{\partial p'}{\partial n}$ in terms of the design velocity and pressure fields as

$$\frac{\partial p'}{\partial n} = -\vec{V} \cdot \nabla(\nabla p) \cdot \hat{n} - \nabla p \cdot \hat{n}' \qquad (6.17)$$

Substituting Eq. (6.17) in Eq. (6.16) yields

$$i = -\int_D \left(\lambda_r (\vec{V} \cdot \nabla(\nabla p_r) \cdot \hat{n} + \nabla p_r \cdot \hat{n}') + \lambda_i (\vec{V} \cdot \nabla(\nabla p_i) \cdot \hat{n} + \nabla p_i \cdot \hat{n}') \right) d\Gamma$$

$$+ \int_C \frac{\frac{1}{2}\left(\frac{1}{2} p\bar{p}\right)^2}{R} (\vec{V} \cdot \hat{n}) ds \qquad (6.18)$$

Once again, one should notice that for a stationary contour the second integral in Eq. (6.18) vanishes. The above equation is a vector relation and coordinate system independent. In the following, this equation is specialized to the Cartesian and the s-n coordinate systems and the accuracy of obtained sensitivities will be discussed consequently.

6.2.4.1 Cartesian Coordinate System

The design vector field is chosen to have only one component in the y-direction, V_y, and Bezier-Bernstein parameterization is used on the control surface as depicted in Figure 6.2. It is easy to see that Eq. (6.18) can be written in the following form for the design sensitivities with respect to the y-coordinate of the Bezier control points:

$$\frac{\partial I}{\partial Y_i} = -\int_0^l \left\{ \lambda_r \left[B_i^m \sqrt{\dot{x}^2 + \dot{y}^2} \left(\frac{\partial^2 p_r}{\partial y^2} n_y + \frac{\partial^2 p_r}{\partial y \partial x} n_x \right) + \frac{dB_i^m}{dt} \left(-\frac{\partial p_r}{\partial x} n_y^2 + \frac{\partial p_r}{\partial y} n_x n_y \right) \right] \right\} dt$$

$$- \int_0^l \left\{ \lambda_i \left[B_i^m \sqrt{\dot{x}^2 + \dot{y}^2} \left(\frac{\partial^2 p_i}{\partial y^2} n_y + \frac{\partial^2 p_i}{\partial y \partial x} n_x \right) + \frac{dB_i^m}{dt} \left(-\frac{\partial p_i}{\partial x} n_y^2 + \frac{\partial p_i}{\partial y} n_x n_y \right) \right] \right\} dt$$

$$+ \int_0^l \left\{ \frac{\frac{1}{2} \left(\frac{1}{2} p \bar{p} \right)^2}{R} \right\} B_i^m n_y \sqrt{\dot{x}^2 + \dot{y}^2} dt$$

$$(6.19)$$

6.2.4.2 Body-fitted s-n coordinates

The second order tensor, $\nabla(\nabla p)$, can be shown to have the following form in the s-n coordinates:

$$\nabla(\nabla p) = \begin{bmatrix} \frac{R}{R+n} \left(\frac{\partial^2 p}{\partial s^2} \frac{R}{R+n} + \frac{\partial p}{\partial s} \frac{n}{(R+n)^2} \frac{\partial R}{\partial s} + \frac{1}{R} \frac{\partial p}{\partial n} \right) & \frac{R}{R+n} \left(\frac{\partial^2 p}{\partial s \partial n} - \frac{\partial p}{\partial s} \frac{1}{R+n} \right) \\ \frac{\partial^2 p}{\partial s \partial n} \frac{R}{R+n} - \frac{R}{(R+n)^2} \frac{\partial p}{\partial s} & \frac{\partial^2 p}{\partial n^2} \end{bmatrix}$$

$$(6.20)$$

Substituting Eq. (6.20) with $n=0$ and $\hat{n} = \begin{bmatrix} 0 & -1 \end{bmatrix}^T$ in Eq. (6.18) yields

$$I = -\int_D \lambda_r \left(\frac{1}{R} \frac{\partial p_r}{\partial s} (\vec{V} \cdot \hat{t}) + \frac{\partial^2 p_r}{\partial n^2} (\vec{V} \cdot \hat{n}) + \frac{\partial p_r}{\partial s} \theta' \right) d\Gamma$$

$$- \int_D \lambda_i \left(\frac{1}{R} \frac{\partial p_i}{\partial s} (\vec{V} \cdot \hat{t}) + \frac{\partial^2 p_i}{\partial n^2} (\vec{V} \cdot \hat{n}) + \frac{\partial p_i}{\partial s} \theta' \right) d\Gamma + \int_C \frac{\frac{1}{2} \left(\frac{1}{2} p \bar{p} \right)^2}{R} (\vec{V} \cdot \hat{n}) ds$$
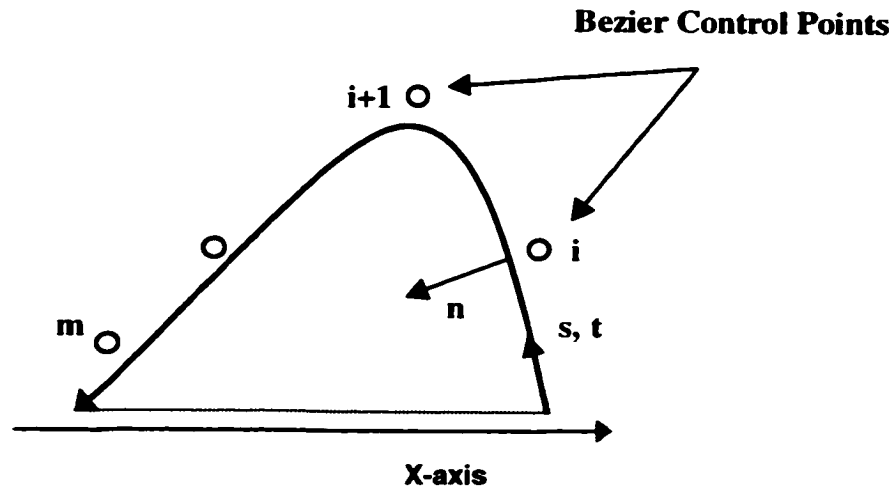
$$(6.21)$$

Bezier Control Points

Figure 6.2 Schematic representation of the control surface (Barrier's top surface)

θ is the angle between the unit tangent and the positive x-axis. In the above equation, the second derivative of the pressure normal to the control surface can be eliminated by writing the governing equation in the s-n coordinates .

$$\nabla^2 p + k^2 p = \frac{R^2}{(n+R)^2}\frac{\partial^2 p}{\partial s^2} + \frac{Rn}{(n+R)^3}\frac{dR}{ds}\frac{\partial p}{\partial s} + \frac{1}{R+n}\frac{\partial p}{\partial n} + \frac{\partial^2 p}{\partial n^2} + k^2 p = 0 \qquad (6.22)$$

By setting $n=0$ and the normal derivative of pressure to zero (from the boundary condition), Eq. (6.21) simplifies considerably and allows us to write the second derivative of p in the normal direction only in terms of its second derivative in the tangential direction and p itself. Hence, the sensitivity derivatives of the cost functional with respect to the y-coordinate of the Bezier control points can be written as:

$$\frac{\partial I}{\partial Y_i} = -\int_0^l \lambda_r \left(B_i^m \frac{1}{R} \frac{\partial p_r}{\partial s} \sin\theta + B_i^m \left(\frac{\partial^2 p_r}{\partial s^2} + k^2 p_r \right) \cos\theta - \frac{\partial p_r}{\partial s} \frac{\cos\theta}{\sqrt{\dot{x}^2 + \dot{y}^2}} \frac{dB_i^m}{dt} \right) \sqrt{\dot{x}^2 + \dot{y}^2} \, dt$$

$$-\int_0^l \lambda_i \left(B_i^m \frac{1}{R} \frac{\partial p_i}{\partial s} \sin\theta + B_i^m \left(\frac{\partial^2 p_i}{\partial s^2} + k^2 p_i \right) \cos\theta - \frac{\partial p_i}{\partial s} \frac{\cos\theta}{\sqrt{\dot{x}^2 + \dot{y}^2}} \frac{dB_i^m}{dt} \right) \sqrt{\dot{x}^2 + \dot{y}^2} \, dt$$

$$-\int_0^l \left\{ \frac{\frac{1}{2} \left(\frac{1}{2} p\bar{p} \right)^2}{R} \right\} B_i^m \cos\theta \sqrt{\dot{x}^2 + \dot{y}^2} \, dt$$

$$(6.22)$$

6.3 Numerical Solution of State Equation

The similarity of the Helmholtz and Laplace's equations suggests that the boundary element method (BEM) is a good candidate for solving the problem in hand. First, a suitable fundamental solution is needed to start off the BEM method. The Bessel function of the second kind and order 0, Y_0, with a coefficient of $-1/4$ satisfies

$$\nabla^2 u^* + k^2 u^* + \delta(\bar{x}_i) = 0 \tag{6.23}$$

and the Bessel function of the first kind and order 0, J_0, satisfies the above equation without the Dirac delta term. Hence, a combination of the form

$$u^*(kr) = \alpha J_0(kr) - \frac{1}{4} Y_0(kr) \qquad r \equiv r[\bar{x}_i, \bar{x}] \tag{6.24}$$

can be used as the fundamental solution. r is the distance between point $\bar{x}_i$ and any field point. However, it is desirable to choose the coefficient α in a way that u^* also satisfies the farfield Sommerfeld boundary condition. For large values of r, the following asymptotic relationships hold:

$$J_n(kr) \sim \sqrt{\frac{2}{\pi kr}} \cos\left(kr - \frac{\pi}{4} - \frac{n\pi}{2}\right)$$

$$Y_n(kr) \sim \sqrt{\frac{2}{\pi kr}} \sin\left(kr - \frac{\pi}{4} - \frac{n\pi}{2}\right)$$

(6.25)

It is straightforward to show that with the choice of $\alpha = i/4$, u^* satisfies the boundary condition of Eq. (6.4) with u^* replacing p. This would help to restrict the surface unknowns to the barrier surface only.

Next, the inner product of the differential problem with the fundamental solution is formed:

$$\lim_{\sigma \to 0} \int_{\Omega - \Omega_\sigma} \left(\nabla^2 p(\bar{x}) + k^2 p(\bar{x}) - \delta(\bar{x}_S) - \delta(\bar{x}_{S'})\right) u^* d\Omega = 0 \qquad (6.26)$$

The limiting process is essential because u^* is unbounded as r tends to zero. Ω_σ is a circle of radius σ centered at $\bar{x}_i$ isolating point $\bar{x}_i$ from the rest of the domain (Figure 6.3). Using Green's second identity, the BIE formulation for the Helmholtz equation is obtained as:

$$\lim_{\sigma \to 0} \left(\int_{\Omega - \Omega_\sigma} p\left(\nabla^2 u^* + k^2 u^*\right) d\Omega + \int_{\Gamma \cup \Gamma_\sigma} \left(u^* \frac{\partial p}{\partial n} - p \frac{\partial u^*}{\partial n}\right) d\Gamma \right) - u^*(\bar{x}_S) - u^*(\bar{x}_{S'}) = 0 \qquad (6.27)$$

Substituting from Eq.(6.23), the first integral has a Dirac delta as the integrand, but as $r=0$ has been excluded from its domain, it vanishes. Therefore, Eq.(6.27) reduces to

$$\lim_{\sigma \to 0} \int_{\Gamma \cup \Gamma_\sigma} \left(u^* \frac{\partial p}{\partial n} - p \frac{\partial u^*}{\partial n}\right) d\Gamma - u^*(\bar{x}_S) - u^*(\bar{x}_{S'}) = 0 \qquad (6.28)$$

Interior Point   **Boundary Point**
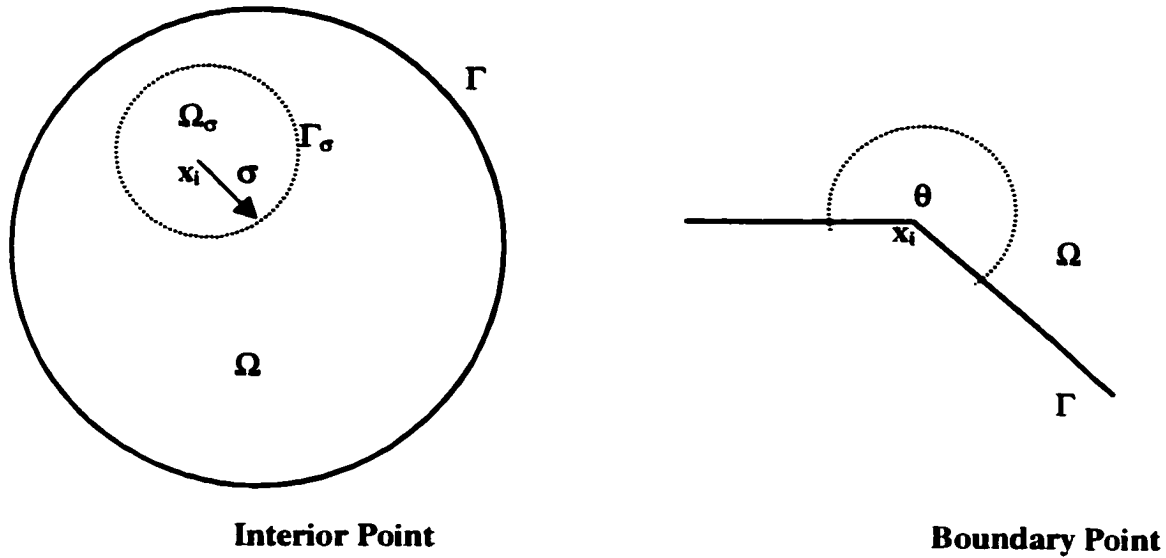
Figure 6.3 Process of exclusion of a point from domain

The fundamental solution u^*, behaves like

$$u^* \sim \frac{i}{4}\left[1 + i\frac{2}{\pi}\ln\left(\frac{kr}{2}\right)\right]$$

(6.29)

for small r and its normal derivative behaves like $1/r$. Therefore, the limiting process is quite straightforward and yields

$$\lim_{\sigma \to 0} \int_{\Gamma \cup \Gamma_\sigma} \left(u^*\frac{\partial p}{\partial n} - p\frac{\partial u^*}{\partial n}\right)d\Gamma = \int_\Gamma \left(u^*\frac{\partial p}{\partial n} - p\frac{\partial u^*}{\partial n}\right)d\Gamma - C(\bar{x}_i)p(\bar{x}_i)$$

(6.30)

where $C(\bar{x}_i)$ is equal to unity for points in the domain interior and on the boundary it is equal to $\theta(\bar{x}_i)/2\pi$, $\theta(\bar{x}_i)$ being the internal angle subtended at $\bar{x}_i$. Application of the boundary condition for perfectly reflecting surfaces renders the final form of the BIE formulation:

$$C(\bar{x}_i)p(\bar{x}_i) + \int_\Gamma p\frac{\partial u^*}{\partial n}d\Gamma = -u^*(\bar{x}_S) - u^*(\bar{x}_{S'})$$

(6.31)

Both linear panels and three node quadratic elements are used to represent the geometry and the unknown p. Eq. (6.31) can be written in matrix form as $Hp=S$; H being the coefficient matrix resulting from the discretization of the LHS and S the vector of source terms from the RHS. The coefficients H_{ij} are calculated using numerical integration formulae such as Gauss quadrature for nonsingular elements ($i \neq j$). For linear, constant, and quadratic elements, the contribution of singular panels can be shown to be identically zero. Linear and quadratic panels are only C_0 continuous and, for C_1 continuity, one has to use cubic elements with two degrees of freedom at each endpoint.

6.4 Numerical Solution of Adjoint Problem

The adjoint problem in the domain is identical to the Helmholtz equation and it is possible to use the same fundamental solution of Eq. (6.24). However, the farfield boundary condition of the adjoint system is different from that of the state equation. Hence, one can still proceed and use the same fundamental solution but will need to add panels at farfield as the farfield boundary condition is not satisfied by the fundamental solution. The alternative is to look for a fundamental solution satisfying the boundary condition of Eq. (6.13). It is not too difficult to see that

$$u^*(kr) = -\frac{i}{4}(J_0(kr) - iY_0(kr))$$ (6.32)

satisfies the adjoint radiation boundary condition. With regard to the adjoint system of Eq. (6.14a), one has to account for the nonhomogenous boundary condition on the control surface and its image, while in the case of Eq. (6.14b), special care has to be given to the accurate integration of the source term in the domain equation.

6.5 Gradient and Hessian of Acoustic field

Sensitivities of Eq. (6.19) require accurate computation of the gradient and some second order derivatives of the acoustic pressure field on the control surface. As the derivatives of p involve highly singular integrals and finding the finite part of these integrals with quadratic shape functions is very cumbersome, this part of the analysis is done on linear panels with two degrees of freedom at the endpoints. Starting from Eq. (6.31) and assuming that $\bar{x}_i$ is away from the endpoints of the panel where $C(\bar{x}_i)$ is discontinuous, it can be written as follows:

$$\frac{1}{2}\nabla_i p = -\int_\Gamma p \nabla_i \left(\frac{\partial u^*}{\partial n}\right) ds - \frac{\partial u^*}{\partial r}\cdot \nabla_i r\bigg|_{\bar{x}_S} - \frac{\partial u^*}{\partial r}\cdot \nabla_i r\bigg|_{\bar{x}_{S'}} \tag{6.33}$$

It can be shown by using some vector identities that

$$\nabla_i\left(\frac{\partial u^*}{\partial n}\right) = (\hat{n}\cdot\nabla_i)\nabla u^* = \left[n_x\frac{\partial}{\partial x_i} + n_y\frac{\partial}{\partial y_i}\right]\nabla u^* = \frac{n_x(x_i - x) + n_y(y_i - y)}{r}\frac{\partial}{\partial r}\left(\frac{\partial u^*}{\partial r}\nabla r\right) \tag{6.34}$$

After some algebraic manipulations, Eq. (6.33) can be cast in the following form:

$$\frac{1}{2}\nabla_i p = -\int_\Gamma p \left\{ \begin{array}{l} \dfrac{1}{r^2}\dfrac{\partial^2 u^*}{\partial r^2}\left[n_x(x_i - x) + n_y(y_i - y)\right]\left[(x - x_i)\hat{i} + (y - y_i)\hat{j}\right] \\[3mm] + \dfrac{1}{r^3}\dfrac{\partial u^*}{\partial r}\left[\begin{array}{l}\left(-n_x(y - y_i)^2 + n_y(y - y_i)(x - x_i)\right)\hat{i} \\ + \left(n_x(x - x_i)(y - y_i) - n_y(x - x_i)^2\right)\hat{j}\end{array}\right] \end{array} \right\} ds$$

$$- \frac{\partial u^*}{\partial r}\cdot \nabla_i r\bigg|_{\bar{x}_S} - \frac{\partial u^*}{\partial r}\cdot \nabla_i r\bigg|_{\bar{x}_{S'}} \tag{6.35}$$

This integral is performed along the whole boundary and it is obviously an improper integral when point i lies on panel j. To simplify the matters, it is chosen to find the

derivatives only at the center of the panels. The above integral on non-singular panels can be found very accurately using Gaussian quadrature but for the singular panel, using the notation of Figure 6.4, it can be shown that

$$\int\limits_{panel\ j} = -\left(sin\,\alpha\,\hat{i} - cos\,\alpha\,\hat{j}\right)\int\limits_{panel\ j} \frac{p\,\frac{\partial u^*}{\partial r}}{r}\,ds \tag{6.36}$$

and the singular integral on the RHS of Eq. (6.36) can be written as

$$\int\limits_{panel\ j} \frac{p\,\frac{\partial u^*}{\partial r}}{r}\,ds = 2p_i\left\{\int\limits_0^{\frac{l}{2}} \frac{1-\frac{2r}{l}}{r}\frac{\partial u^*}{\partial r}\,dr + \frac{2}{l}\int\limits_0^{\frac{l}{2}}\frac{\partial u^*}{\partial r}\,dr\right\} \tag{6.37}$$

Substituting for u^* in terms of the Bessel functions, J_0 and Y_0, the first integral on the RHS of Eq. (6.37) can be cast in the following form:

$$2p_i\int\limits_0^{\frac{l}{2}} \frac{1-\frac{2r}{l}}{r}\frac{\partial u^*}{\partial r}\,dr = \frac{-ikp_i}{2}\int\limits_0^{\frac{l}{2}} \frac{1-\frac{2r}{l}}{r}J_1(kr)dr + \frac{kp_i}{2}\int\limits_0^{\frac{l}{2}} \frac{1-\frac{2r}{l}}{r}Y_1(kr)dr \tag{6.38}$$

The integral involving J_1 is regular as J_1/r is finite as $r \rightarrow 0$, but the integral with Y_1 in its integrand is singular and its principal value (PV) needs to be found. After integration by parts and some straightforward limiting process, it can be shown that

$$PV\left(\frac{kp_i}{2}\int\limits_0^{\frac{l}{2}} \frac{1-\frac{2r}{l}}{r}Y_1(kr)dr\right) = \frac{p_i}{l}\left(Y_0(v) - \frac{2}{\pi}(\gamma - ln\,2)\right) + \frac{kp_i}{2}\int\limits_0^v Y_0\,d\eta - \frac{kp_i}{2}Y_1(v) \tag{6.39}$$

where $v = kl/2$ and $\gamma = .5772156$ is the Euler's constant.
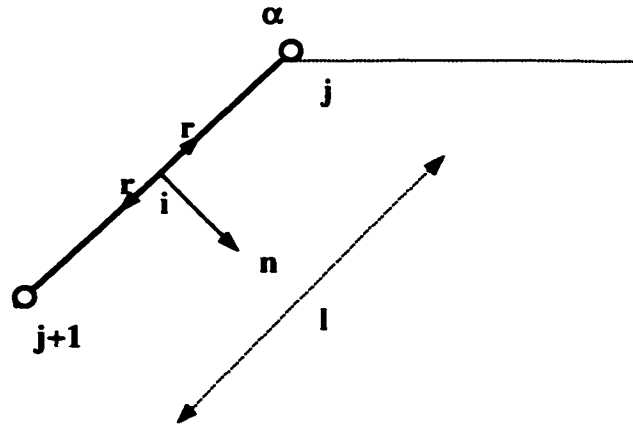
Figure 6.4 Schematic of a panel on the surface of the barrier

Putting together the results of Eqs. (6.37)-(6.39), the principal value of the integral on the singular panel can be finally written as:

$$PV\left(\int_{panel\,j}\right) = -(sin\,\alpha\,\hat{i} - cos\,\alpha\,\hat{j})PV\left(\int_{panel\,j}\frac{p\frac{\partial u^*}{\partial r}}{r}ds\right)$$

$$= -(sin\,\alpha\,\hat{i} - cos\,\alpha\,\hat{j})\left[\frac{p_i}{4l}\left(u^*(v) - \frac{l}{4}\left(\frac{2}{\pi}(\gamma - ln\,2)\right)\right) - \frac{ikp_i}{2}\int_0^{\frac{l}{2}}\frac{l - \frac{2r}{l}}{r}J_1(kr)dr\right]$$
$$\left. + \frac{p_i}{l}\left(Y_0(v) - \frac{2}{\pi}(\gamma - ln\,2)\right) + \frac{kp_i}{2}\int_0^v Y_0 d\eta - \frac{kp_i}{2}Y_1(v)\right]$$

(6.40)

Note that the integral of Y_0 in the above equation is regular because Y_0 behaves like the natural logarithm for small values of r. Now, the second derivatives of the acoustic pressure field on the barrier's surface can be computed by differentiating Eq. (6.35) with respect to x_l and y_l and after some algebraic manipulation, the following three equations are obtained.

$$\frac{1}{2}\frac{\partial^2 p}{\partial x_i^2} = -\int_\Gamma p \left\{ \begin{array}{l} \dfrac{1}{r^2}\dfrac{\partial^2 u^*}{\partial r^2}\left[-2n_x(x_i - x) - n_y(y_i - y)\right] - \dfrac{1}{r^3}\dfrac{\partial u^*}{\partial r}n_y(y - y_i) \\[3mm] + \dfrac{x_i - x}{r}\left[-n_x(x_i - x)^2 + n_y(y_i - y)(x - x_i)\right]\left(\dfrac{-2}{r^3}\dfrac{\partial^2 u^*}{\partial r^2} + \dfrac{1}{r^2}\dfrac{\partial^3 u^*}{\partial r^3}\right) \\[3mm] + \left(-\dfrac{3}{r^4}\dfrac{\partial u^*}{\partial r} + \dfrac{1}{r^3}\dfrac{\partial^2 u^*}{\partial r^2}\right)\left(-n_x(y - y_i)^2 + n_y(y - y_i)(x - x_i)\right)\dfrac{x_i - x}{r} \end{array} \right\} ds$$

$$- \left[\frac{x_i - x}{r}\left(\frac{1}{r^2}\frac{\partial^2 u^*}{\partial r^2} - \frac{1}{r^2}\frac{\partial u^*}{\partial r}\right)(x_i - x_s) + \frac{1}{r}\frac{\partial u^*}{\partial r}\right]_{\bar{x} = \bar{x}_S}$$

$$- \left[\frac{x_i - x}{r}\left(\frac{1}{r^2}\frac{\partial^2 u^*}{\partial r^2} - \frac{1}{r^2}\frac{\partial u^*}{\partial r}\right)(x_i - x_{s'}) + \frac{1}{r}\frac{\partial u^*}{\partial r}\right]_{\bar{x} = \bar{x}_{S'}}$$

(6.41a)

$$\frac{1}{2}\frac{\partial^2 p}{\partial y_i^2} = -\int_\Gamma p \left\{ \begin{array}{l} \dfrac{1}{r^2}\dfrac{\partial^2 u^*}{\partial r^2}\left[-n_x(x_i - x) - 2n_y(y_i - y)\right] + \dfrac{1}{r^3}\dfrac{\partial^2 u^*}{\partial r^2}n_x(x_i - x) \\[3mm] + \dfrac{y_i - y}{r}\left[-n_y(y_i - y)^2 + n_x(y - y_i)(x_i - x)\right]\left(\dfrac{-2}{r^3}\dfrac{\partial^2 u^*}{\partial r^2} + \dfrac{1}{r^2}\dfrac{\partial^3 u^*}{\partial r^3}\right) \\[3mm] + \left(-\dfrac{3}{r^4}\dfrac{\partial u^*}{\partial r} + \dfrac{1}{r^3}\dfrac{\partial^2 u^*}{\partial r^2}\right)\left(-n_y(x - x_i)^2 + n_x(y - y_i)(x - x_i)\right)\dfrac{y_i - y}{r} \end{array} \right\} ds$$

$$- \left[\frac{y_i - y}{r}\left(\frac{1}{r^2}\frac{\partial^2 u^*}{\partial r^2} - \frac{1}{r^2}\frac{\partial u^*}{\partial r}\right)(y_i - y_s) + \frac{1}{r}\frac{\partial u^*}{\partial r}\right]_{\bar{x} = \bar{x}_S}$$

$$- \left[\frac{y_i - y}{r}\left(\frac{1}{r^2}\frac{\partial^2 u^*}{\partial r^2} - \frac{1}{r^2}\frac{\partial u^*}{\partial r}\right)(y_i - y_{s'}) + \frac{1}{r}\frac{\partial u^*}{\partial r}\right]_{\bar{x} = \bar{x}_{S'}}$$

(6.41b)

$$
\frac{1}{2}\frac{\partial^2 p}{\partial y_i \partial x_i} = -\int_\Gamma p \left\{
\begin{aligned}
&\frac{1}{r^2}\frac{\partial^2 u^*}{\partial r^2}n_y(x-x_i) + \frac{1}{r^3}\frac{\partial u^*}{\partial r}\left[2n_x(y-y_i)-n_y(x-x_i)\right] \\
&+\frac{y_i-y}{r}\left[-n_x(x_i-x)^2 + n_y(y_i-y)(x-x_i)\right]\left(\frac{-2}{r^3}\frac{\partial^2 u^*}{\partial r^2}+\frac{1}{r^2}\frac{\partial^3 u^*}{\partial r^3}\right) \\
&+\left(-\frac{3}{r^4}\frac{\partial u^*}{\partial r}+\frac{1}{r^3}\frac{\partial^2 u^*}{\partial r^2}\right)\left(-n_x(y-y_i)^2+n_y(y-y_i)(x-x_i)\right)\frac{y_i-y}{r}
\end{aligned}
\right\} ds
$$

$$
-\left[\frac{y_i-y_s}{r}\left(\frac{1}{r^2}\frac{\partial^2 u^*}{\partial r^2}-\frac{1}{r^2}\frac{\partial u^*}{\partial r}\right)\right]_{\bar{x}=\bar{x}_s}
-\left[\frac{y_i-y}{r}\left(\frac{1}{r^2}\frac{\partial^2 u^*}{\partial r^2}-\frac{1}{r^2}\frac{\partial u^*}{\partial r}\right)\right]_{\bar{x}=\bar{x}_{s'}}
$$

$$(6.41c)$$

When point i lies on the panel, the above integrals are singular and the principal values of these integrals need to be determined. Fortunately, it can be shown that the integrands of the singular panels of the Eqs. (6.41a-c) can be all written in terms of one singular integral as indictated in Eq. (6.42).

$$
\int_{panel\,j} Eq.(6.41a) = -\sin(2\alpha)\int_{panel\,j}\frac{p}{r^2}\left(-r\frac{\partial^2 u^*}{\partial r^2}+\frac{\partial u^*}{\partial r}\right)ds
$$

$$
\int_{panel\,j} Eq.(6.41b) = \sin(2\alpha)\int_{panel\,j}\frac{p}{r^2}\left(-r\frac{\partial^2 u^*}{\partial r^2}+\frac{\partial u^*}{\partial r}\right)ds \qquad (6.42)
$$

$$
\int_{panel\,j} Eq.(6.41c) = \cos(2\alpha)\int_{panel\,j}\frac{p}{r^2}\left(-r\frac{\partial^2 u^*}{\partial r^2}+\frac{\partial u^*}{\partial r}\right)ds
$$

Using the first order shape functions and assuming that I is at the middle of the panel, the singular integral of the RHS of Eq. (6.42) reduces to

$$
\int_{panel\,j}\frac{p}{r^2}\left(-r\frac{\partial^2 u^*}{\partial r^2}+\frac{\partial u^*}{\partial r}\right)ds = 2p_i\int_0^{\frac{l}{2}}\left(-\frac{\partial^2 u^*}{\partial r^2}+\frac{1}{r}\frac{\partial u^*}{\partial r}\right)dr \qquad (6.43)
$$

Substituting for the fundamental solution in terms of Bessel functions and using the reccurence formulas available for the Bessel functions, the integrand of Eq. (6.43) reduces to

$$-\frac{\partial^2 u^*}{\partial r^2} + \frac{1}{r}\frac{\partial u^*}{\partial r} = \frac{k^2}{4}\frac{(Y_2 - iJ_2)}{r} \tag{6.44}$$

and upon using integration by parts and the fact that

$$PV\left(\frac{Y_1(\varepsilon)}{\varepsilon}\right) = \frac{1}{\pi}(\gamma - \ln 2) - \frac{1}{2\pi} \tag{6.45}$$

the following expression for the principal value of Eq. (6.43) is obtained.

$$PV\left(\int_j \frac{p}{r^2}\left(-r\frac{\partial^2 u^*}{\partial r^2} + \frac{\partial u^*}{\partial r}\right)ds\right) = 2p_i\left[\frac{k^2}{4}\left(-\frac{Y_1(v)}{v} + PV\left(\frac{Y_1(\varepsilon)}{\varepsilon}\right)\right) - \frac{ik}{4}\left(-\frac{J_1(v)}{v} + \frac{1}{2}\right)\right] \tag{6.46}$$

The result of Eq. (6.46) can be inserted in Eq. (6.42) to compute the principal value of the singular panels confronted in the computation of the second derivatives of the acoustic field. For all the regular panels, Gaussian quadrature is used for integration.

CHAPTER 7

Results of Shape Optimization with 2D Euler Equations on Unstructured Meshes for General Cost Functionals

7.1 Definition of Demonstrated Cases

The continuous adjoint formulation of Chapter 4, which is coupled with a CFD solver, optimizer, surface parameterizer, and mesh movement module, will now be demonstrated. Three cases are considered where the shape of an airfoil is optimized for different objective functions, f, as assigned to the cost function of Eq. (3.3). In all three cases, the Bezier control points, $\bar{P}_i$, of Eq. (3.42) are treated as the design variables, and side constraints are assigned to the y-coordinate of each one of the knots, Y_i of Eq. (3.44). Also, geometric constraints can be applied to control, e.g., the trailing edge included angle, maximum thickness, thickness at mid-chord, included area.

Each optimization cycle starts with a symmetric profile as the initial design. A steady state solution is obtained for the airfoil at 2-deg angle of attack in Mach 0.75 flow. For the sake of driving the optimization, the target aerodynamics is obtained from the solution of the flow at the same conditions but for an RAE profile. The initial profile and its 11th order Bezier control point distribution and the unstructured mesh for the target profile are shown in Figure 7.1 a-b. The mesh has 14,590 cells (7,480 nodes) and there are 370 nodes on the airfoil (design) surface. The airfoil surface is Bezier-Bernstein parameterized with 24 Bezier control points, of which 22 of them are used as the design variables. The Bezier points located at the leading and trailing edges are kept fixed to enforce unit chord length and avoid the effect of pure translation in a finite computational domain.
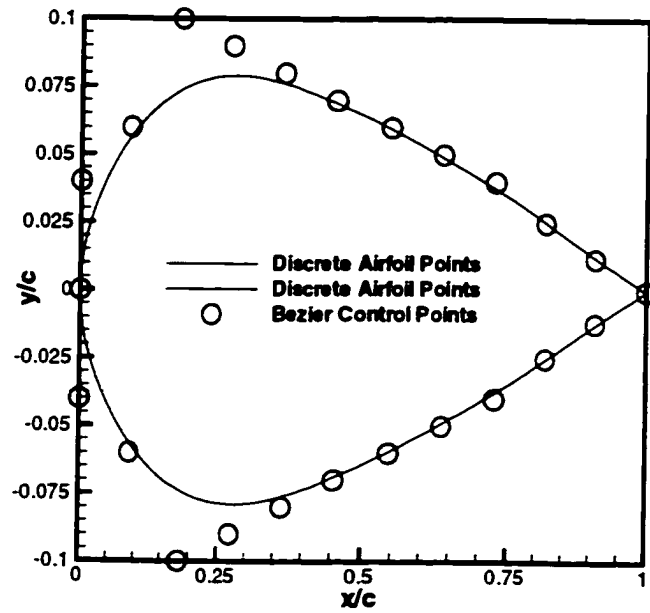
(a)

Figure 7.1 (a) Bezier control points for initial airfoil (b) Unstructured mesh for target airfoil design.
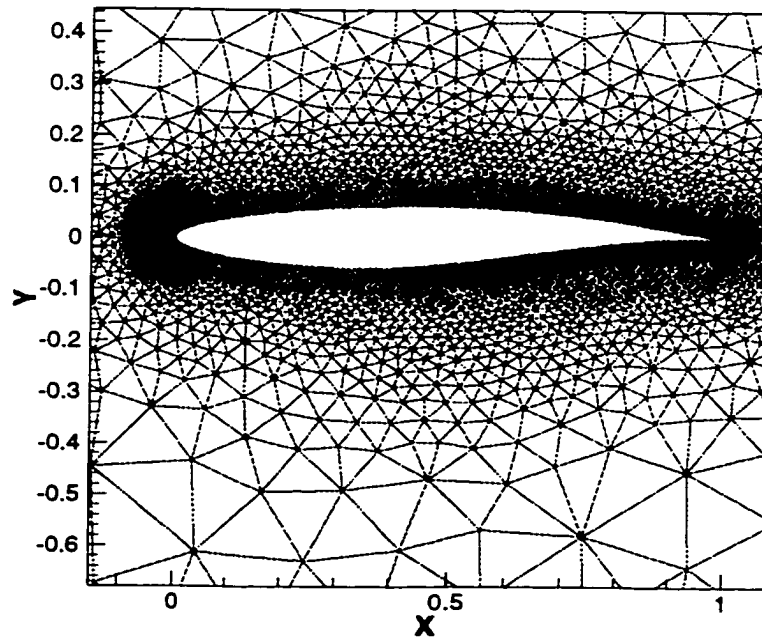
(b)

Figure 7.1 Concluded.

7.2 Sensitivities and Optimization

In Figure 7.2, the computed sensitivities are compared with the benchmark brute force derivatives to ensure that the formulation is capable of producing comparable derivatives with the finite-difference sensitivities. As the discretization error of the continuous formulation does not correspond to that of the state equations, only in the limit when the mesh size approaches zero, the continuous approach and the brute force method are expected to yield identical sensitivities. However, it is clear from Figure 7.2 that the computed sensitivities compare well with the finite difference derivatives for the fairly fine mesh employed in this work.
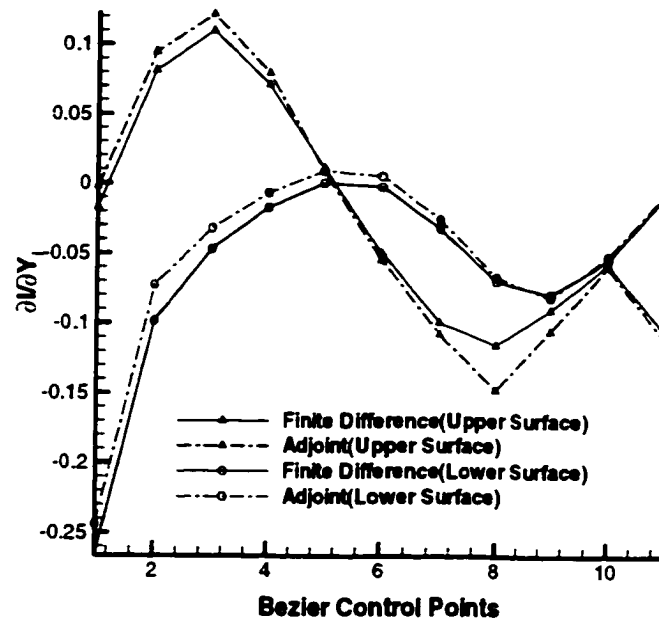
Figure 7.2 Computed continuous adjoint sensitivities versus benchmark finite-difference (brute force) derivatives.

The first case is the conventional minimization of the departure from the target pressure distribution denoted by p^t

$$f = \tfrac{1}{2}\left(p - p^t\right)^2 \tag{7.1}$$

Presented in Figures 7.3 a-c are the surface pressure distributions, shape evolution, and the variation of the cost functional for Case 1. Each figure includes the respective plots for the initial and target profiles, and those that correspond to two intermediate and the final designs. The final design and its pressure distribution are virtually identical to the target. Although the results are very close to the target after 30 flow analyses and 5 gradient evaluations, with the shock locations coincident, the residual of the cost functional does not meet the stopping criterion. It is only after another 45 analyses and 5 gradient evaluations, the variations in the cost functional reduces to stop the optimization.
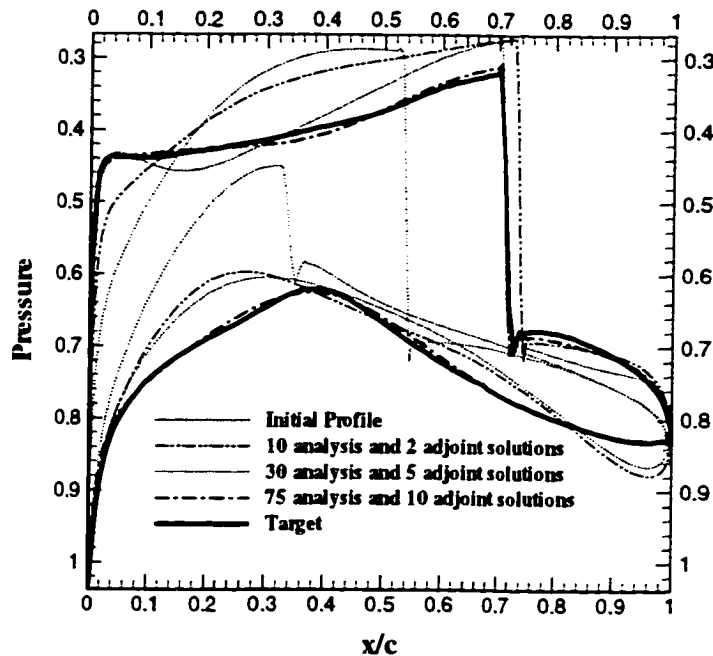
(a)

Figure 7.3 (a) History of surface pressure distributions for Case 1

(b) Evolution of airfoil shapes for Case 1

(c) Convergence history for Case 1.
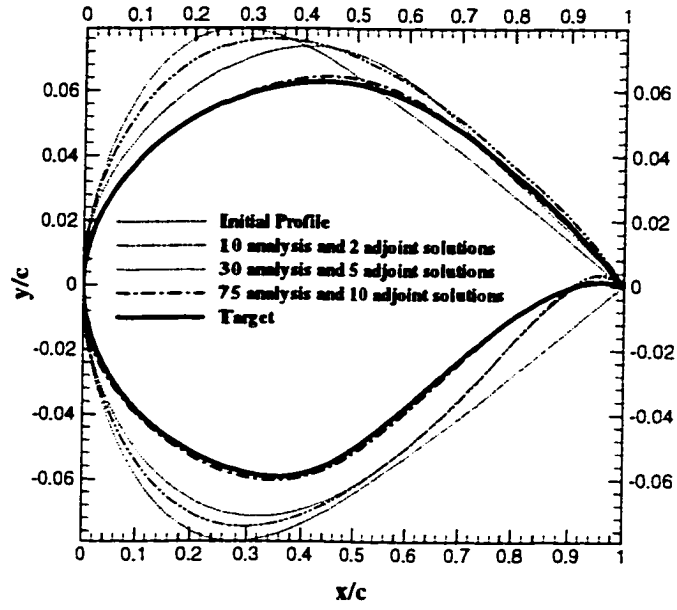
(b)

Figure 7.3 Continued.
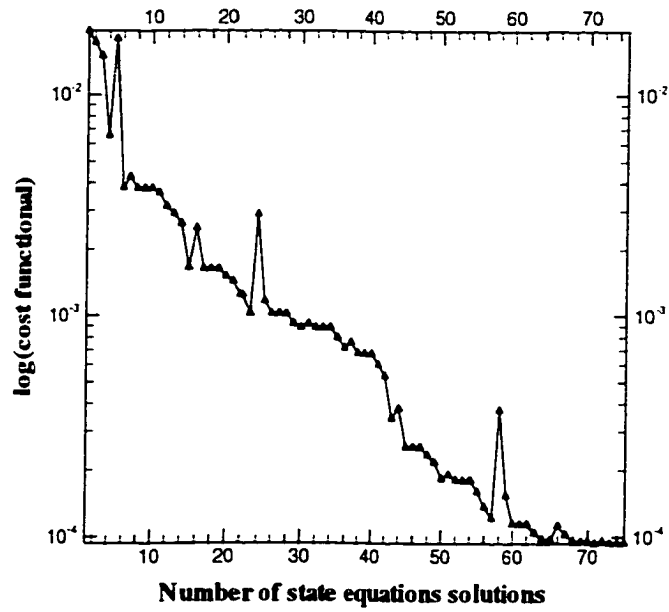
(c)

Figure 7.3 Concluded.

The second case is selected to demonstrate that the present formulation is general and the cost functional does not have to include pressure. The objective now is the minimization of the departure from a target density distribution, ρ_t,

$$f = \tfrac{1}{2}\left(\rho - \rho^t\right)^2 \tag{7.2}$$

Presented in Figures 7.4 a-c are the surface density distributions, shape evolution, and the variation of the cost functional for Case 2. Each figure includes the respective plots for the initial and target profiles, and those that correspond to one intermediate and the final designs. The final design and its pressure distribution are again virtually identical to the target. To the best of author's knowledge, these results are the only results available in the literature for a generalized cost functional with the continuous adjoint method.
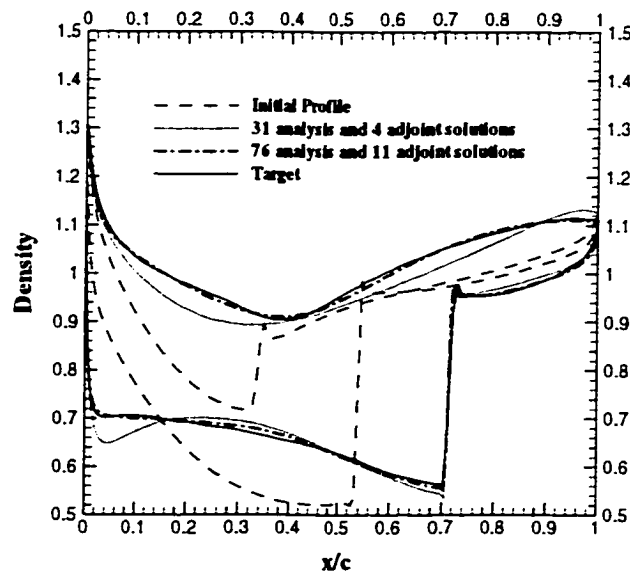
(a)

Figure 7.4 (a) History of surface density distributions for Case2.
(b) Airfoil shape evolution for Case 2.
(c) Convergence history for Case2.
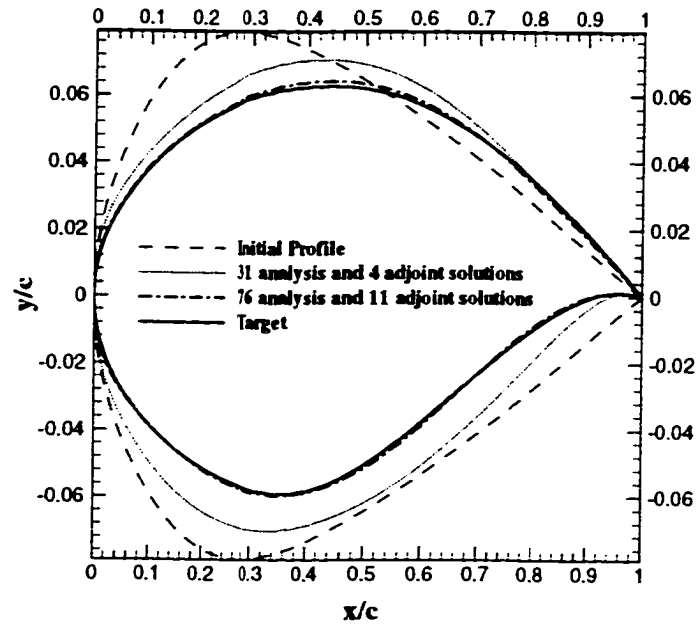
(b)

Figure 7.4 Continued.
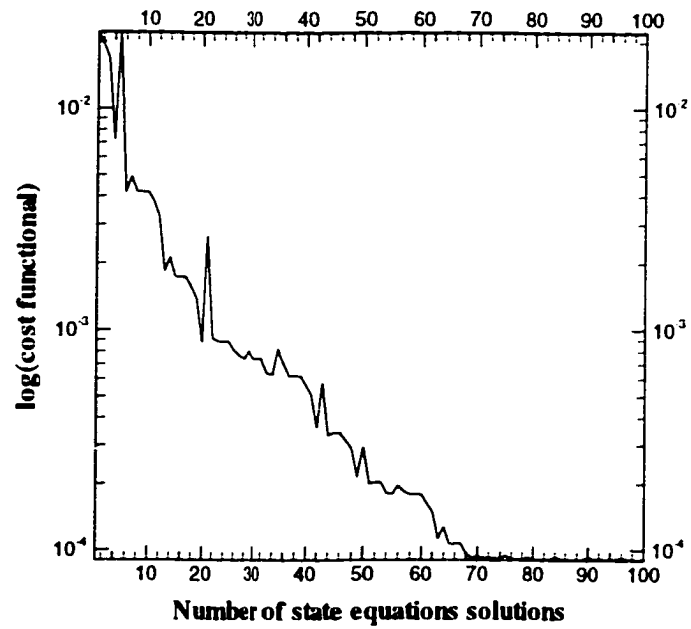
(c)

Figure 7.4 Concluded.

Finally, Case 3 is considered to demonstrate a composite cost functional which includes an aerodynamic constraint through a penalty coefficient. The drag is added to the cost functional of Case 1 after multiplying it by the coefficient, Λ, which is assigned a value of 0.1:

$$f = \tfrac{1}{2}\left(p - p^{t}\right)^{2} ds + \Lambda C_{d} \tag{7.3}$$

Presented in Figures 7.5 a-c are the surface pressure distributions, shape evolution, and the history of the lift and drag for Case 3. Each figure includes the respective plots for the initial and target profiles, and those that correspond to three intermediate and the final designs.
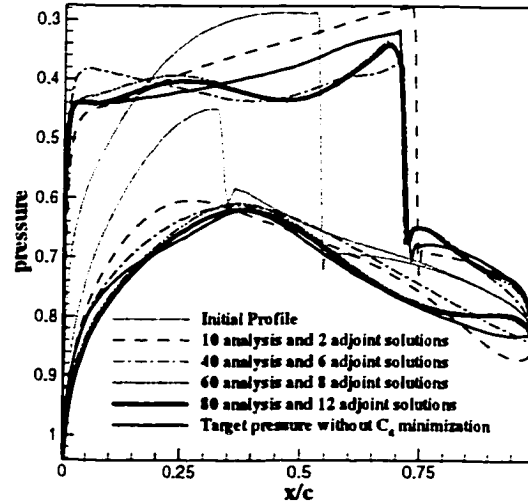
(a)

Figure 7.5 (a) History of surface pressure distributions for Case3.

(b) Shape evolution for Case 3.

(c) History of C_L and C_D in optimization process for Case 3.

Since this case is not only a minimization of a departure from the target but also drag

minimization, the final shape is not known a priori (blind optimization). Instead, the

profile that supports the target pressure distribution (the first term in Eq. (7.3)), is

overlaid on the figures. The final design has the upper surface shock at about the same

location as the target shape. However, as expected, the shape and the distribution,

particularly the upper surface, are shaped by the optimizer to minimize the drag.
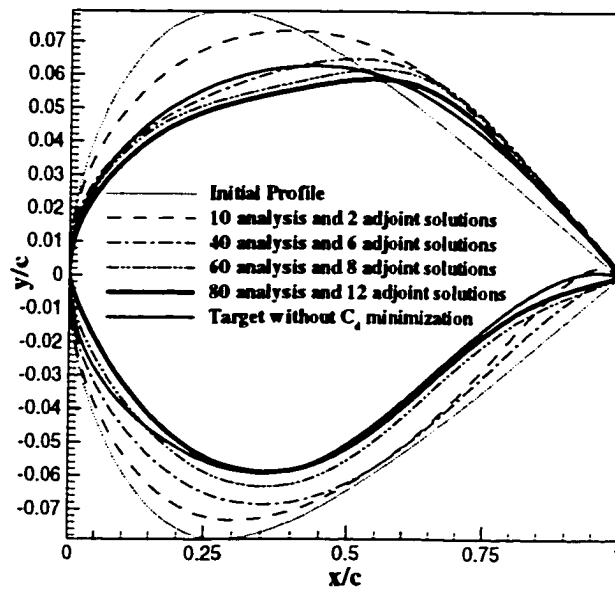
(b)

Figure 7.5 Continued.
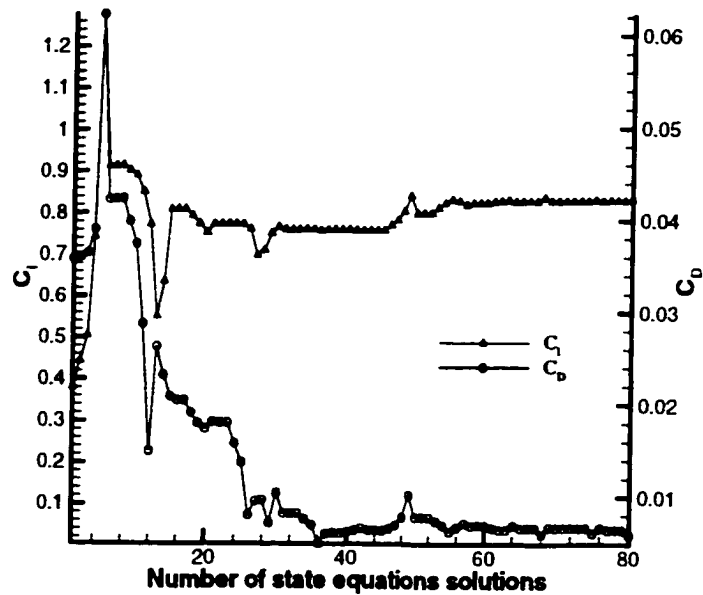
(c)

Figure 7.5 Concluded.

All of these cases are produced on a desktop computer. This is possible since generating the continuous sensitivities requires no additional memory beyond that of the flow analysis (for the present cases, it is 65 megabytes). Unlike solving for the discrete sensitivities, here there is no need to form any large matrices. In the present continuous adjoint method, the average computational time needed for one design cycle is about 1.8 times that for one flow analysis.

7.3 Summary of Results

An adjoint approach is developed to obtain the continuous sensitivity derivatives for the Euler equations and general cost functionals. Both the state and the adjoint equations are second-order finite-volume discretized for unstructured meshes, and they

are coupled with a constrained optimization algorithm. Also integrated into the overall methodology are a geometry parameterization method for the shape optimization, and a dynamic unstructured mesh method for the shape evolution and the consequent volume mesh adaptations. For the proof-of-concept, three airfoil optimization problems in transonic flow are presented. These results establish the generality of the method in accepting cost functions, the accuracy of the obtained sensitivity derivatives, and the efficiency with which the optimized shapes are obtained on a desktop personal computer.

Chapter 8

Results of Steady and Limit-Cycle Shape Optimization with Transonic Small Disturbance Equation

8.1 Justifying TSD Modification

Experimentation with the original TSD shows, that for a NACA 0012 airfoil at freestream Mach number of 0.63 and 2° angle of attack, a nonphysical shock appears on the suction surface, whereas experimental data certifies that both surfaces are subcritical. Figure 8.1 illustrates that the inclusion of the correction term in Eq. (5.2) delays the unphysical transition of the partial differential equation from elliptic (subsonic) to hyperbolic type (supersonic).

NACA 0012, $M_\infty=0.63$, $\alpha=2.0°$
Mesh: 300×40 with 200 points on the airfoil surface

Modified TSD (m=1.5)
Original TSD
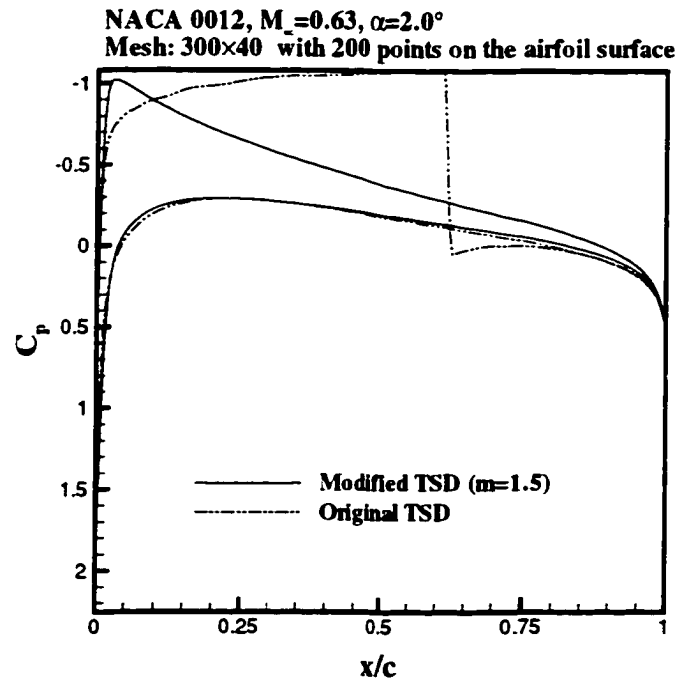
Figure 8.1 Prediction of shock-free flow past airfoil with modified TSD.

8.2 Steady Transonic Flowfield

Figures 8.2 and 8.3 show the present computations performed for flows past a NACA 0012 airfoil at different Mach numbers and angles of incidence. In Figure 8.2, the results have been compared with the corresponding Euler solution, which requires significantly more computing time. The comparison is strikingly good except very close to the leading edge. This is somewhat expected, since the small disturbance assumption is less valid in the vicinity of a blunt leading edge.
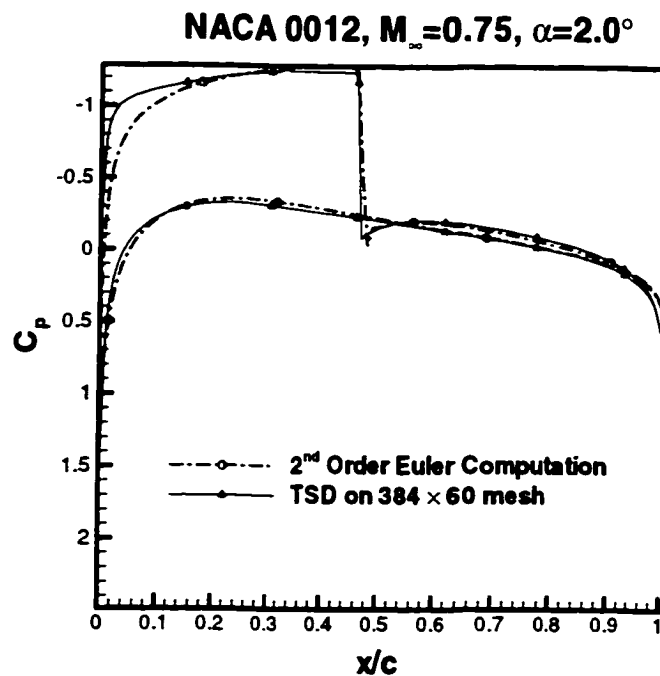
Figure 8.2 Comparison of TSD and Euler solution.

Shown in Figure 8.3 are the pressure distributions over the same airfoil at the freestream Mach number of 0.70 but for different angles of attack.

NACA 0012, M_∞=0.70, m=1.90
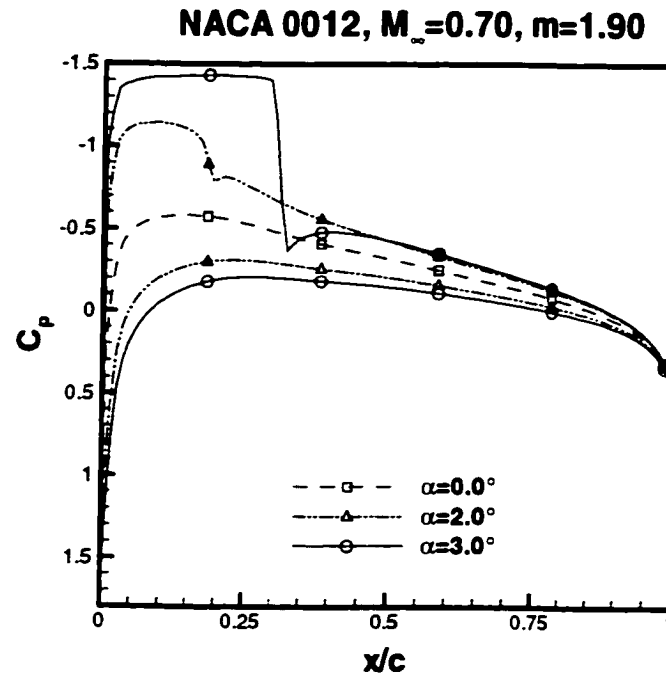
Figure 8.3 TSD solutions for flow past airfoil at different angles of attack.

The agreement of the TSD results with the experimental data deteriorates as the shock gets stronger (by increasing either the incidence or the freestream Mach number). This is attributable to the limitation of the TSD equation in modeling shocks; it does not satisfy the jump condition across the shock. Thence, as shocks get stronger, their position and the pressure coefficients before and after the shock are predicted with less accuracy. This also manifests itself in more iterations required for convergence, as can be observed in Figure 8.4 and Table 8.1. The convergence (reduction of L_2-norm of the residual to 10^{-13}) of the algorithm for computations on a 192×20 grid (128 points on each airfoil surface) requires more execution with increasing angle of attack.
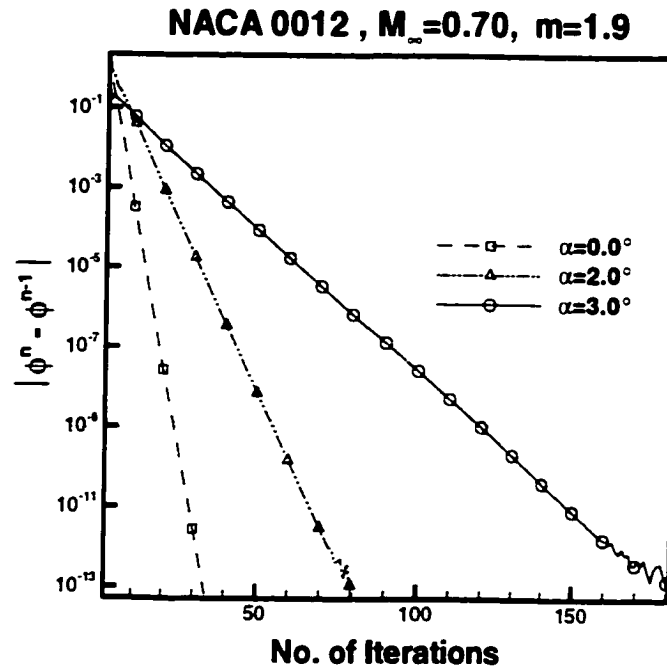
Figure 8.4 Convergence history for flow past airfoil at different angles of attack

$M_\infty=0.70$	No. of Iterations	Execution Time (Seconds)[1]
$\alpha=0.0°$	34	6.5
$\alpha=2.0°$	73	13.9
$\alpha=3.0°$	181	33.7

Table 8.1 Execution time and iteration numbers versus angle of attack

[1] All computations performed on a 200 MHz Pentium Pro desktop computer.

8.3 Validation of Unsteady Flow Analysis

The problem considered here for the validation is the AGARD benchmark case number 5 of Landon (1982): NACA 0012 airfoil in freestream Mach number of 0.755, undergoing a forced pitching oscillation around a pivot point at its quarter-chord measured from the leading edge. The angle of incidence as a function of time is given by $\alpha(t) = \alpha_0 + \alpha_a \sin(\kappa t)$ where $\alpha_0 = 0.016°$, $\alpha_a = 2.51°$, and $\kappa = 0.1628$. The grid size is 150×20 with 100 points on each side of the airfoil. In Figure 8.5, the normal force coefficient is plotted against the angle of attack. The limit cycle is achieved after computing three cycles, and the results compare as well with the experimental data as the other published results using Euler or Navier-Stokes equations, e.g. Periare (1997).
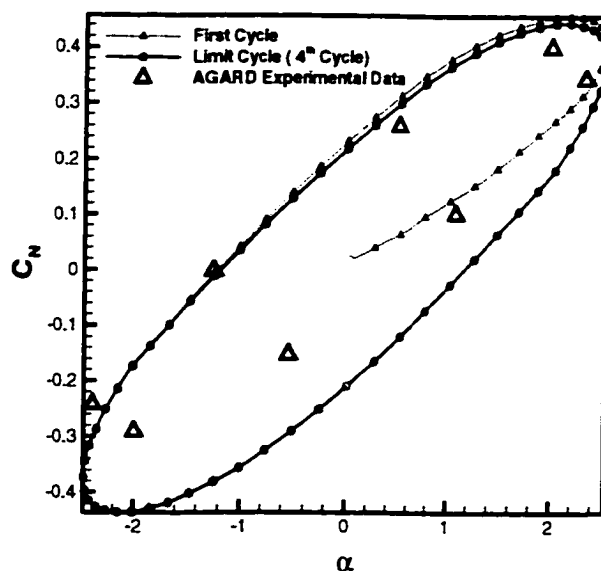

Figure 8.5 Limit-cycle for normal force of a pitching airfoil in Mach 0.755.

Also compared with the experimental data are the instantaneous pressures over the airfoil surface at three different instants (Figure. 8.6 a-c). Only minor deviations are observed,

as expected, close to the leading edge. In these computations, one cycle is covered in 200 uniform time steps, with 15 to 20 subiterations needed per time step to achieve convergence to 10^{-10}. On a 200 MHz Pentium computer, each time step requires approximately 3.8 seconds to converge. The number of time steps per cycle can be reduced at the expense of an increase in the number of subiterations. The optimal combination for the minimum processing time has not been studied.
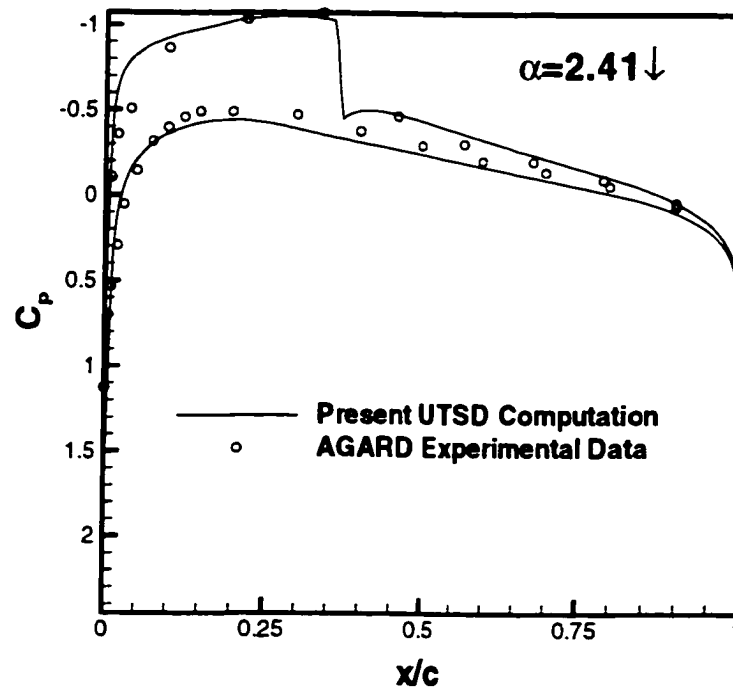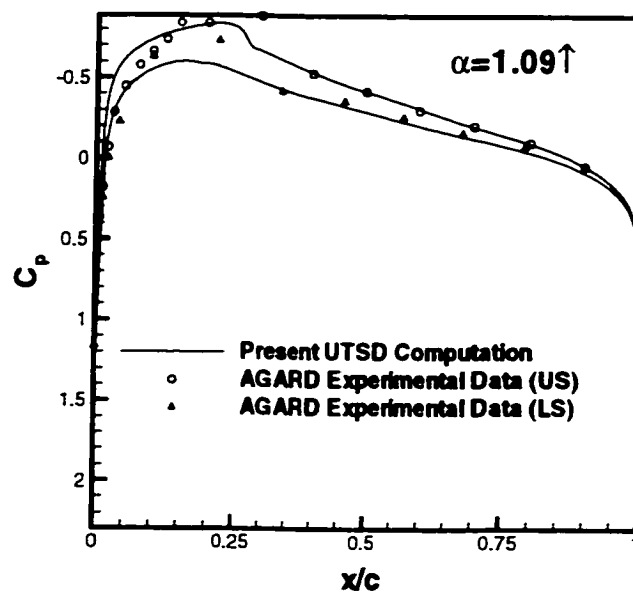

(a)

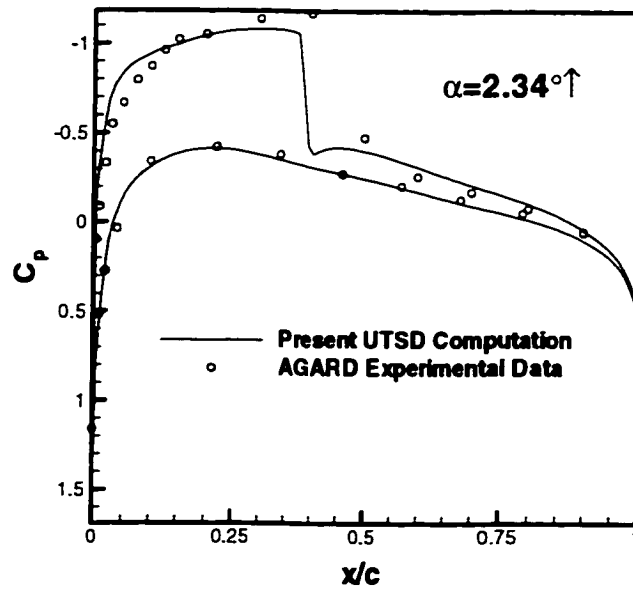Figure 8.6 Pressure coefficients on airfoil surface in Mach 0.755 flow at three instants:
(a) 2.41° -pitch down, (b) 1.09°-pitch up, and (c) 2.34°-pitch up.

(b)

Figure 8.6 Continued.

(c)

Figure 8.6 Concluded.

8.4 Validation of Analytical Adjoint Sensitivities

The present continuous adjoint sensitivities are now compared in Figure 8.7 with those obtained by the brute-force finite differences. The Dirac delta function in the wall boundary conditions, Eq. (5.20), confronts the methodology with the problem of representing an infinite number (δ $(x\text{-}x_{TE})\rightarrow \infty$ as $x \rightarrow x_{TE}$) on a finite grid. Refining the mesh in the vicinity of x_{TE} and scaling the Dirac delta with the local mesh spacing can alleviate this obstacle at the expense of a stretched mesh close to the trailing edge. Yet ignoring the Dirac delta term causes error in the computed sensitivities. Also shown in Figure 8.7 is the divergence of the sensitivities from the correct values when the Dirac delta is dropped from the analysis.
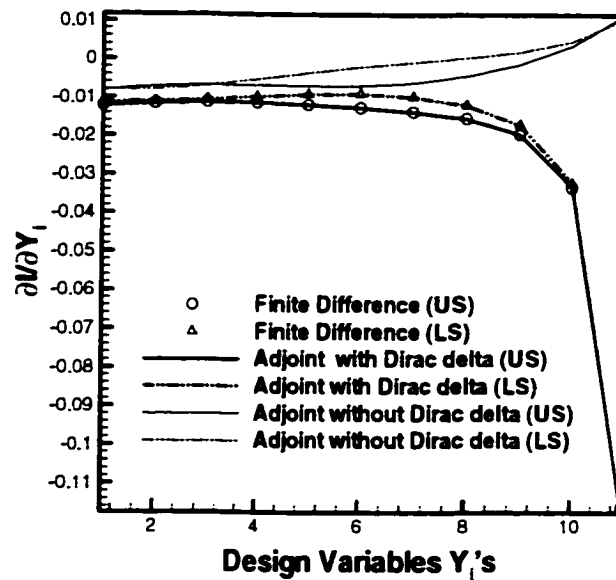

Figure 8.7 Comparing adjoint sensitivities with finite-difference derivatives and effect of boundary conditions.

More specifically, this would effectively be neglecting the boundary sensitivity of the circulation Γ, which takes values that are at least two orders of magnitude larger than the sensitivities of the cost functional as can be seen in Figure 8.8.
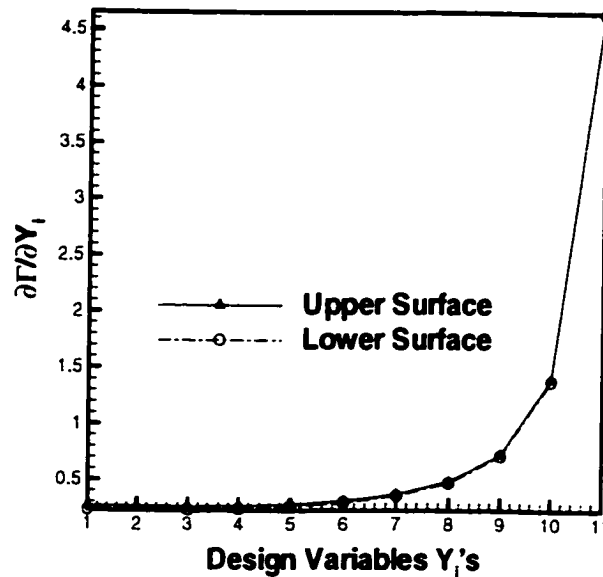

Figure 8.8 Sensitivity of flow circulation.

8.5 Steady Shape Optimization

The present method will now be used to optimize a shape subjected to steady loads. The demonstrative example considered herein, starts from an arbitrary symmetric airfoil as the initial design. A steady state solution is obtained for Mach 0.6 flow approaching at 2.0° angle of attack. The target values of the velocity potential distribution are obtained from the solution of a RAE airfoil at the same conditions. The mesh, which has 192×30 points, is highly stretched normal to the surface, and 128 points are along the airfoil surface. The design variables are the 22 of the total 24 Bezier control points. The evolution of the profile shape and the corresponding C_p distributions are

presented in Figures 8.9(a) and 8.9(b) respectively. The resulting optimized shape meets the target airfoil shape virtually point by point.
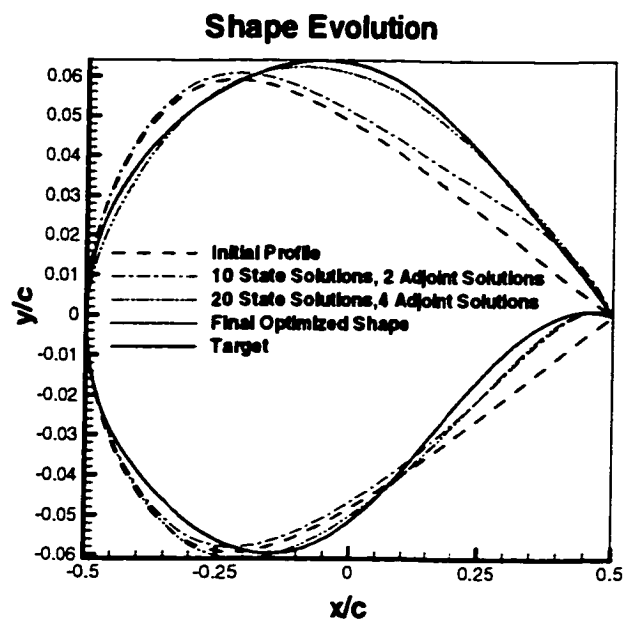
Shape Evolution

(a)

Figure 8.9 History of optimization with steady loads: (a) shape, (b) surface pressures.

This result is obtained after 51 adjoint solutions (full optimization cycles) and a total of 288 state equation solutions (Figure 8.10). Each state equation solution is converged to 10^{-9} in about 20 seconds on a 200 MHz Pentium Pro desktop computer. The cost of an average adjoint solution with convergence to 10^{-8} is about 2.2 times that of one flow analysis.
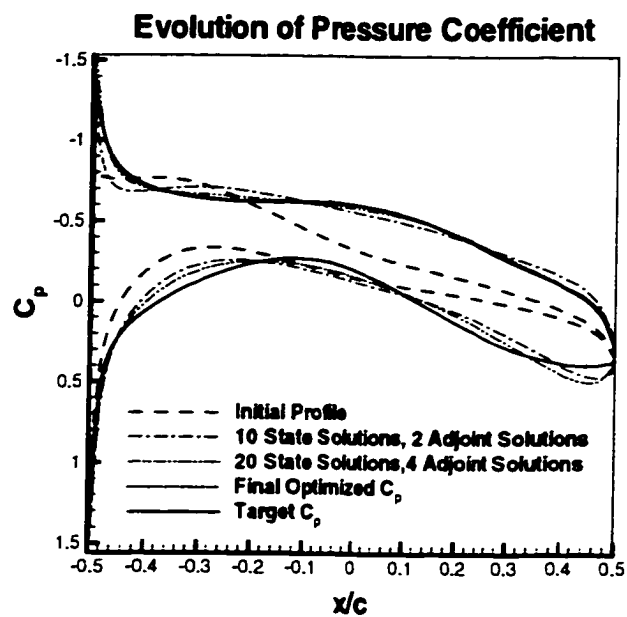
Evolution of Pressure Coefficient

(b)

Figure 8.9 (Concluded)

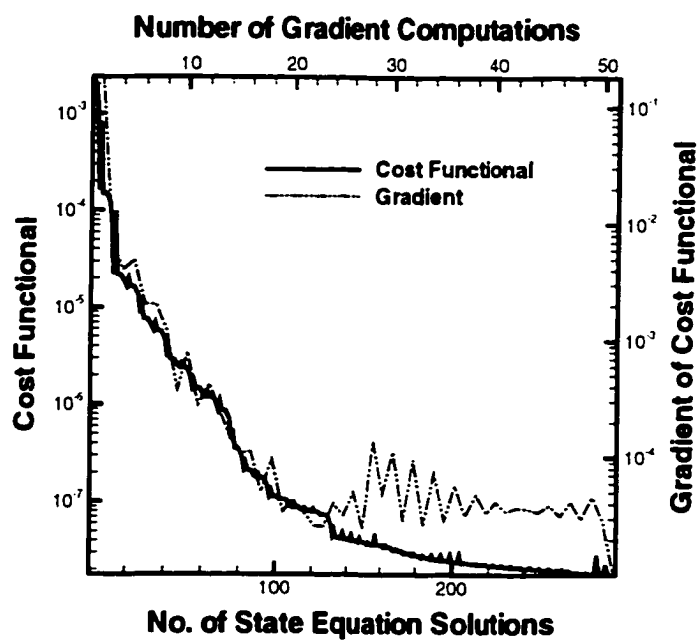**Number of Gradient Computations**

Figure 8.10 Convergence history of cost functional and its gradient during steady optimization

8.6 Unsteady Shape Optimization

The example considered here is an inverse problem, where the target potential is that of a known RAE airfoil at freestream Mach number of 0.6. The airfoil is performing a pitching oscillation with $\alpha_0 = 0°$, $\alpha_a = 2°$, and $\kappa = 0.1$. The pivot point is located at the quarter-chord measured from the leading edge. Each cycle of the airfoil motion is divided into 60 equal computational time steps. The mesh size for this case is 120×20, with 80 points along the airfoil surface, and the mesh is highly stretched normal to the surface. As in the steady flow case, the design variables are the 22 Bezier control points defining the upper and lower surfaces of the profile.

Double integrals present in the formulation (Eq. 5.21) are reduced to two one-dimensional integrations. At each time step, the integrand is approximated in space with an interpolating cubic spline and the integration is carried out analytically. The integrated values are once again fitted with an interpolating cubic spline in time and the value of the double integral is rendered by the analytical integration of the piecewise continuous interpolating spline.

In Figures 8.11-8.12, this shape optimization process is summarized. The evolution of the shape from the initial to the target profile is demonstrated in Figure 8.11. The optimized profile shape is very close to the target profile. As it is observed in Figure 8.11, the normal force variation of the optimized shape for one period of motion matches that of the target airfoil very closely.
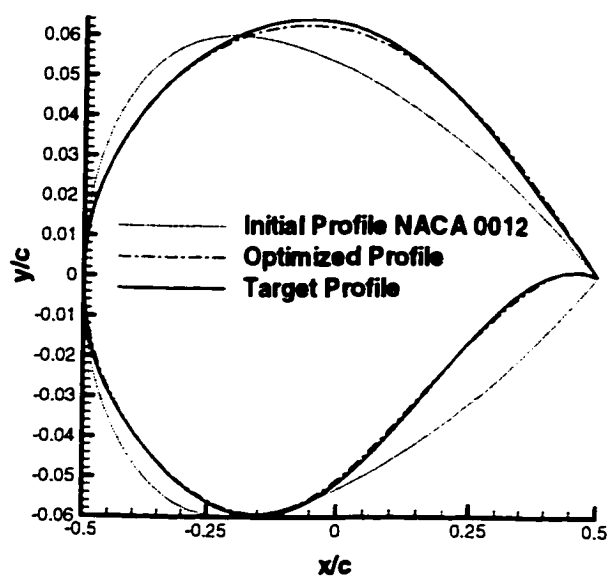
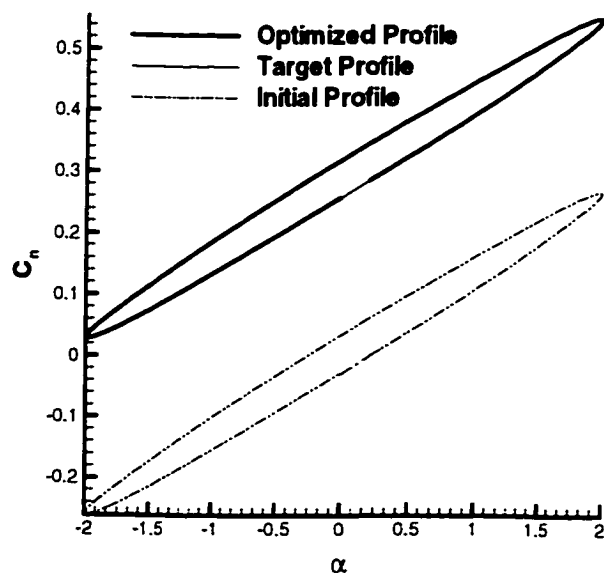Figure 8.11 Shape evolution during optimization with unsteady loads due to airfoil oscillations.

Figure 8.12 Normal force coefficient versus angle of attack at limit-cycle.

The convergence histories of the cost functional and its gradient are presented in Figure 8.13. An average adjoint solution takes about 163 seconds on a 200 MHz Pentium Pro desktop computer, which is about 0.2 of one UTSD solution. The unsteady flow analysis from the UTSD equation requires about 20 sub-iterations for advancing the solution by one time step while the adjoint solution requires only about 5 iterations to resolve the coupled adjoint variable system λ-ψ at each time step. Therefore, the average cost of obtaining the gradient of the cost functional is about 1.2 times that of an analysis.

No. of Adjoint Solutions

No. of State Equation Solutions
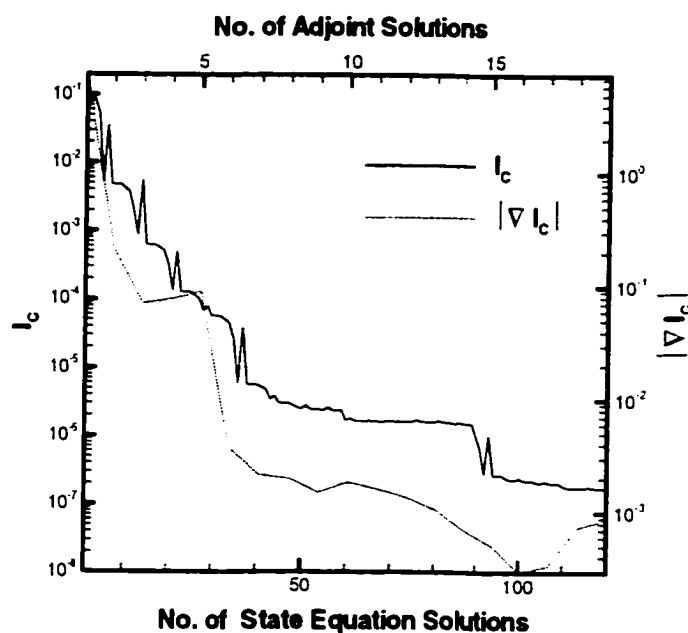
Figure 8.13 Convergence of cost functional and its gradient during optimization with unsteady loads.

8.7 Summary of Results

In unsteady aerodynamics and automated aerodynamic design optimization, the flowfield needs to be analyzed numerous times. Hence, a compromise between the computational efficiency and the level of accuracy in the flow physics quickly becomes

the critical issue. Therefore, the modified, unsteady, transonic, small disturbance (UTSD) equation is considered to render quick and inexpensive solutions for a design environment on desktop computers. By virtue of the underlying assumptions, only flows past streamlined objects at small angles of attack can be considered.

To perform gradient-based shape optimization, a new time-accurate algorithm is developed for the UTSD equation and its adjoint equation. The steady state and limit-cycle sensitivities are derived by the continuous adjoint method and validated by comparing them with those obtained by using the brute-force finite difference approach. The importance of accounting for the variation of the flow circulation, appearing as a Dirac delta in the wall boundary condition, is emphasized and demonstrated. Then, an airfoil is shape optimized very efficiently to meet the prescribed target aerodynamics in both steady and unsteady flow regimes.

It is remarkable that the cost of an unsteady adjoint solution is about 0.2 times that of a state equation solution, which demonstrates the advantage of the continuous adjoint method over the brute force method. It should be noted, however, that unsteady optimization requires the history of the flow variables within a full period of the flow oscillation. This can potentially be impractical for higher-fidelity physical models of the flowfield. Further research, therefore, would be needed to extend the method to more complicated models of the flow physics such as the Euler and N-S equations.

CHAPTER 9

Demonstration of Helmholtz Equation Sensitivities

9.1 Sensitivities at Various Control Surface Configurations

In this chapter, the results of the application of the continuous adjoint method to the Helmholtz equation are demonstrated. In Chapter 6, the sensitivity derivatives were derived in two coordinate systems, the Cartesian and the natural s-n coordinates, and it was emphasized that the accuracy of the computed derivatives depended primarily on the accuracy with which the first and second order derivatives of the acoustic field were obtained. It was also shown that in the s-n system, the only derivative terms in the final expression for the sensitivities were the first and second-order tangential derivatives, while in the Cartesian system, the sensitivities involved the gradient vector and the Hessian of the acoustic pressure. Intuitively, one would expect the s-n coordinates to render more accurate results, and this point is illustrated through the computation of design derivatives for a few carefully chosen test cases in the present chapter.

In Figure 6.1, the sound source of frequency $f=150$ Hz is located at $x_s=$ -54.0″ and $y_s=$ 12.27″, measured from the origin of a coordinate system with the y-axis along the symmetry line of the barrier and the x-axis on the ground. The thickness of the barrier is 4.875″ and its height is 55.25″. The speed of sound a_0 is assumed to be 1140 ft/sec. The x and y dimensions are both scaled by $x\_scale = 7.875″$, and the frequency f, is scaled by a_0 / x_scale, resulting in an acoustic wave number k equal to 0.452. The control surface

is chosen to be the top surface of the barrier, parameterized with the Bezier-Bernstien polynomials. The Helmholtz equation and its adjoint system are both resolved using quadratic panels, but the derivative information on the control surface for the Cartesian approach are computed using linear panels. The cost functional is chosen as,

$$I_C = \frac{1}{2} \int_C \left(\frac{1}{2} p\bar{p} \right)^2 ds.$$

(9.1)

The contour C is chosen to be either the control surface itself or a vertical straight line in the domain connecting points $(27.625, 55.250)''$ and $(27.625, 82.875)''$.

The initial configurations, at which the design derivatives are computed, are shown in Figure 9.1.
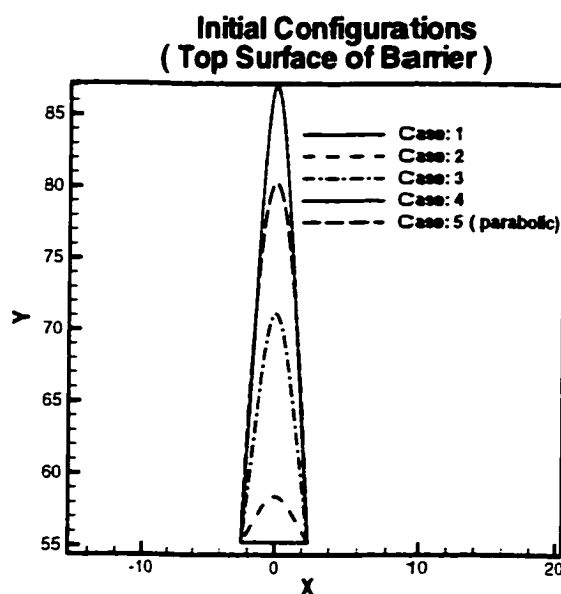

Figure 9.1 Top surface shapes at which the sensitivites are computed.

In Cases 1-4, the control surface is parameterized with an 8th order Bezier-Bernstein polynomial, while a 2nd order (parabolic) polynomial is used for Case 5. The

curvature of the control surface in Case 1 is zero everywhere, but the Cases 2-4 exhibit considerable variation in curvature as a function of arclength, increasing in the order of their numbering.

First, cases where the contour C is coincident with the control surface are considered. Figure 9.2a illustrates the sensitivities obtained using the Cartesian formulation for Case 1.
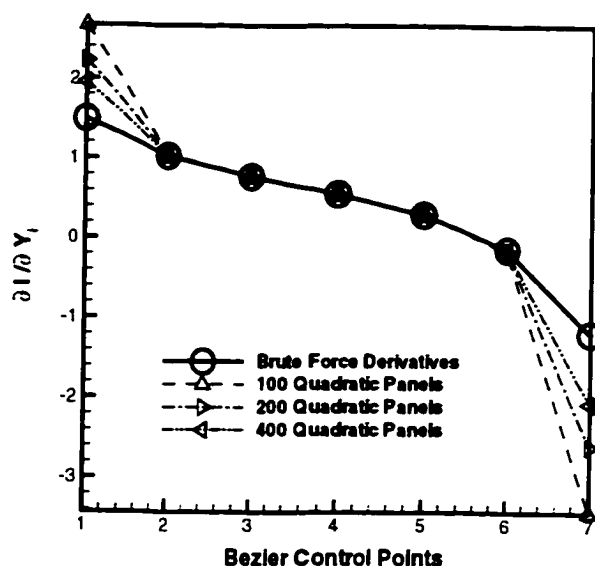
(a)

Figure 9.2 (a) Design derivatives with the Cartesian formulation for Case 1.
(b) Effect of panel refinement on accuracy.

The computed sensitivities agree fairly well with the finite-difference derivatives for Bezier control points 2-5 but deviate considerably at the control points close to the end points of the top surface. However, as the number of panels are increased, the deviation at the end control points decrease rapidly. This is expected, because the accuracy of the gradient and the Hessian matrix deteriorate considerably in the vicinity of

geometric singularities (slope discontinuity at the intersection of the barrier walls with the top surface). Figure 9.2b focuses on the 4th control point and demonstrates the effect of panel refinement on the accuracy of design derivatives.
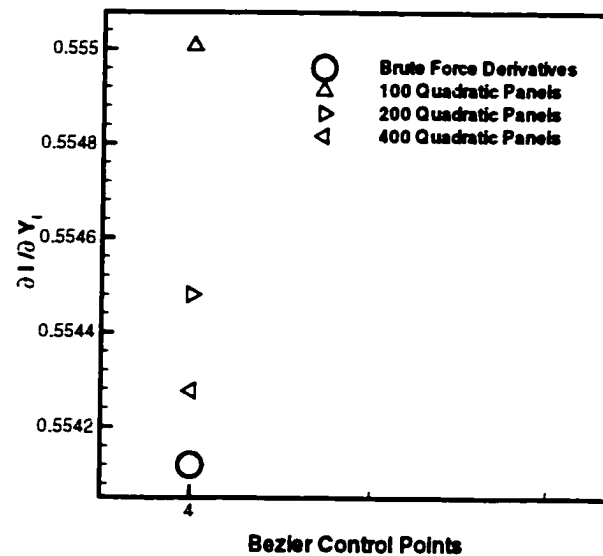
(b)

Figure 9.2 Concluded.

However, the Cartesian approach fails in predicting accurate derivatives for Case 2, as depicted in Figure 9.3. Even the panel refinement has an unexpected adverse effect on the accuracy. This phenomenon is in line with the Babuska paradox as discussed in Chapter 4. The author believes that further work is necessary to obtain the first and second order derivatives from second-order quadratic panels instead of linear panels. At its current form, the Cartesian approach cannot handle curved surfaces.
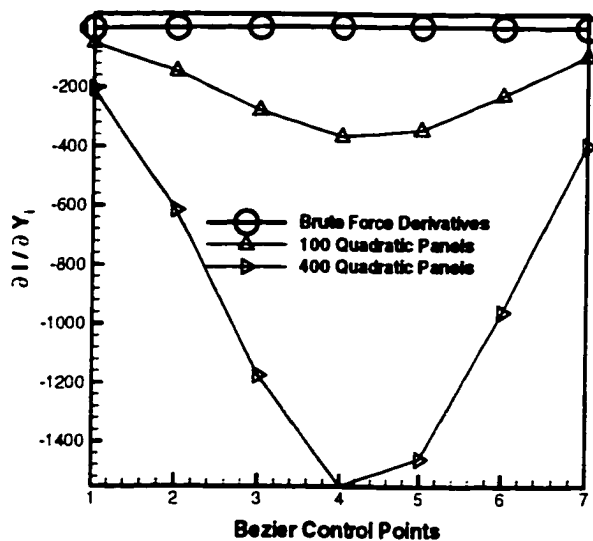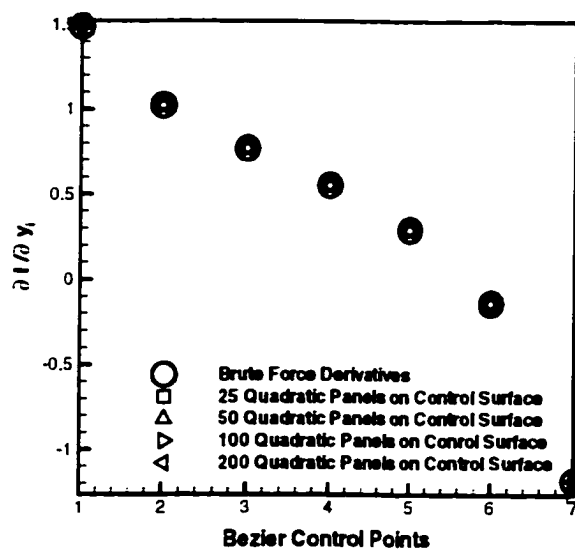
Figure 9.3 Deviation of the Cartesian approach in spite of panel refinement for Case 2.

(a)

Figure 9.4 (a) The s-n approach sensitivities for Case 1.

(b) Effect of panel refinement.

Next, the natural coordinate approach is tested with the Case 1 configuration. In

all the following results, the acoustic pressure on the control surface are fitted with

interpolating cubic splines and the integrations are done adaptively to capture the sharp variation of surface curvature. As it can be seen from Figure 9.4a, the s-n formulations produces design derivatives which match the brute force derivatives virtually point by point. A blow up of Figure 9.4a at the 4th control point is shown below in Figure 9.4b, demonstating the effect of panel refinement. With 200 panels on the design surface, the derivatives differ on average from the exact values by less than 0.005%.
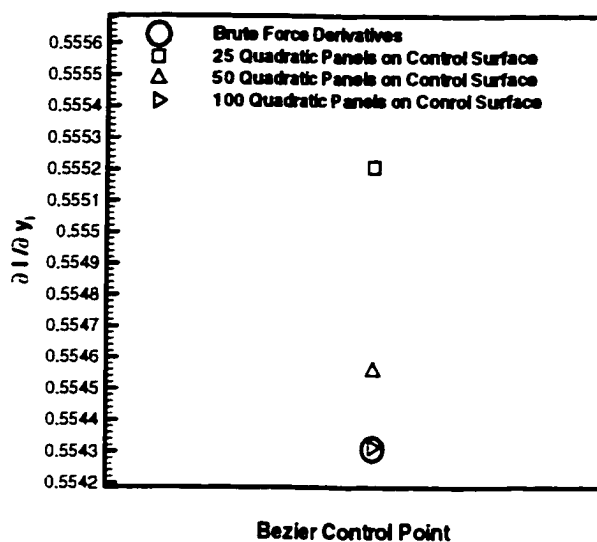
(b)

Figure 9.4 Concluded.

The s-n formulation design sensitivities for Cases 2-4 are illustrated in Figures 9.5-9.7. It can be easily seen that the accuracy of the obtained derivatives deteriorates sharply as the control surface becomes progressively more curved. For instance, for the slightly curved Case 2, derivatives match the finite difference values by an average margin of error of 0.01% with 100 quadratic panels on the control surface. For Case 2, this margin increases

to 0.7% with 200 panels, and for Case 3 the derivatives deviate from the brute force derivatives by more than 34% with 300 panels!
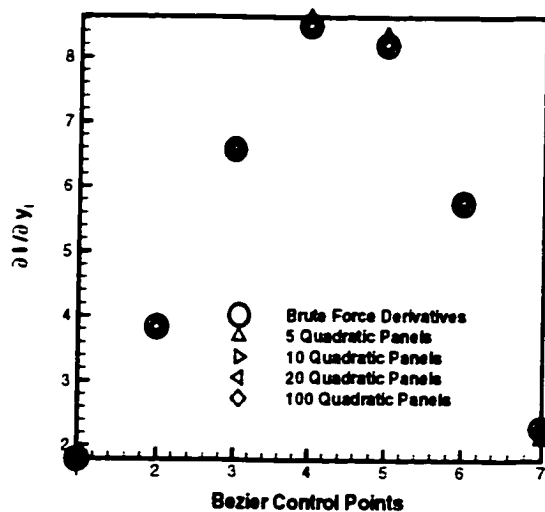
(a)

Figure 9.5 (a) The *s-n* approach sensitivities for Case 2.

(b) Effect of panel refinement.
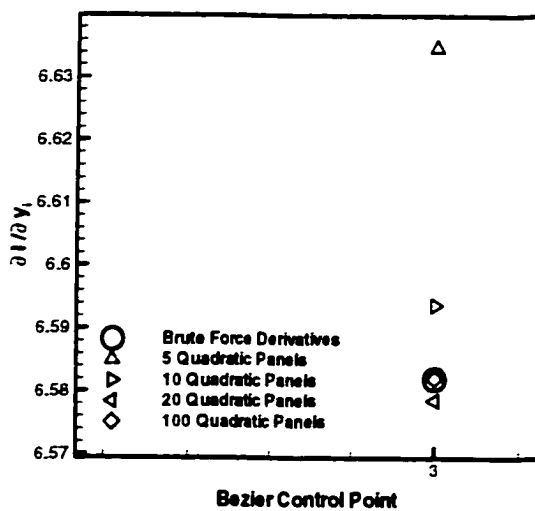
(b)

Figure 9.5 Concluded.
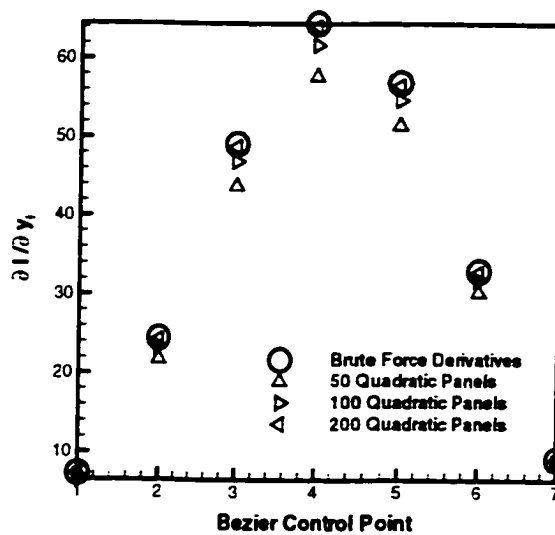
(a)

Figure 9.6 (a) The *s-n* approach sensitivities for Case 3.

(b) Effect of panel refinement.
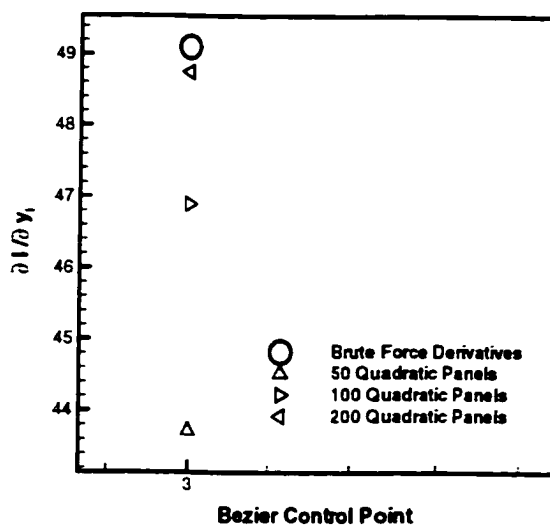
(b)

Figure 9.6 Concluded.
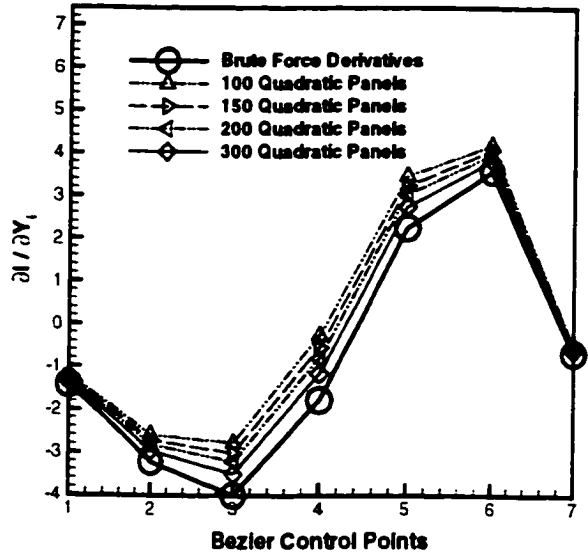
(a)

Figure 9.7 (a) The *s-n* approach sensitivities for Case 4.

(b) Effect of panel refinement.
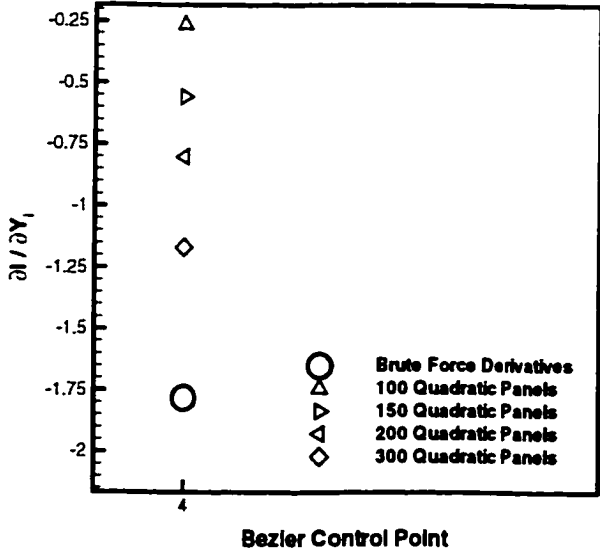
(b)

Figure 9.7 Concluded.

It is clearly seen that the rate of convergence to the brute-force derivatives drops sharply as the surface curvature becomes more pronounced. There can be two plausible explanations for this phenomenon: either the analytical development is wrong or the problem lies in the numerics. The analytical formulation of Chapter 6 assumes continuous first and second order tangential derivatives gauranteeing smooth variation of the control surface curvature. However, at the discretized level, the control surface is fitted with piecewise quadratic panels with discontinous derivatives at panels endpoints. The curvature that the discretized equations see is the curvature of the quadratic panels , while the analysis deals with the curvature of the smooth 8th order Bezier-Bernstein polynomial. It can be seen from Figure 9.7b that as the number of panels increase the deviation of the adjoint sensitivities from the finite-difference derivatives decreases, but it is essential to show that this is actually the case. To validate the analytical sensitivities of Chapter 6 and the above argument, the control surface is parameterized with a second order Bezier-Bernstein polynomial (Case 5 of Figure 9.1). With this choice of parameterization, the quadratic panels would match the quadratic parameterized curve and the curvature seen by the discretization would be identical to that of the analytical developement. The end Bezier control points are fixed and only one design variable remains. The results are listed in the Table 9.1. With 300 quadratic panels on the design surface, the deviation from the brute-force derivative is less than 3%, dropping to about 0.3% for 700 panels. Comparing these results with the results shown in Figure 9.7 for Case 4, where the deviation is approximately 34% with 300 panels, further validates the above argument.

No. of Quadratic Panels	Derivative
100	57.716
200	61.327
300	62.926
500	64.218
700	64.593
Finite-Difference Derivative	**64.778**

Table 9.1 Comparison of brute-force derivative with continuous adjoint derivative for a

parabolic control surface.

Next, the results of the case with curve C in the domain for Cases 1 and 3 are

demonstrated.
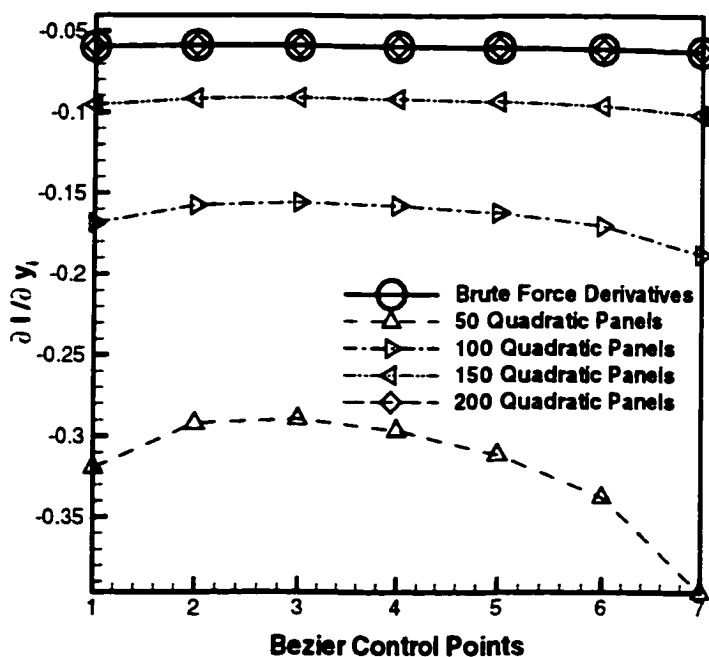
(a)

Figure 9.8 (a) The s-n approach sensitivities with C in the domain for Case 1.

(b) Effect of panel refinement.
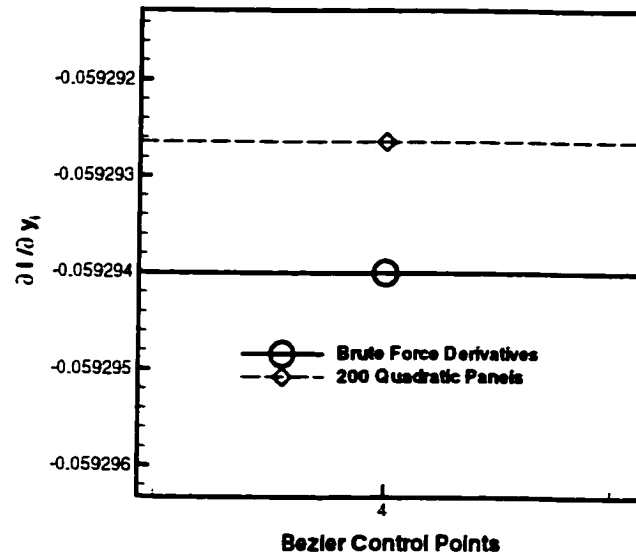
(b)

Figure 9.8 Concluded.
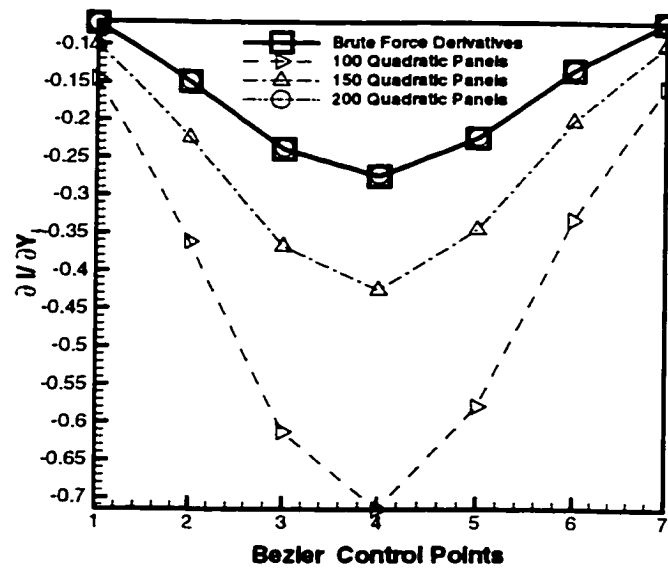
(a)

Figure 9.9 (a) The s-n approach sensitivities with C in the domain for Case 3.

(b) Effect of panel refinement.
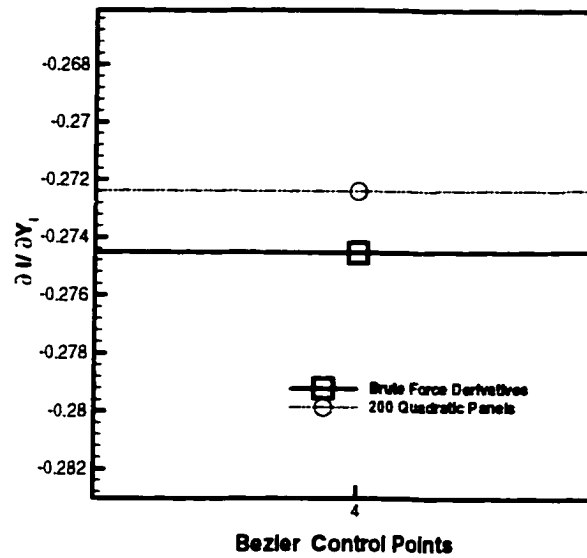
(b)

Figure 9.9 Concluded.

Figures 9.8a-b and 9.9a-b clearly show that the method can easily provide sensitivity information for functionals that are not necessarily defined on the control surface. The key to obtaining accurate sensitivities is precise integration of the source term of the adjoint system, which can be easily done adaptively to the required accuracy. Figure 9.8b clearly shows that with 200 quadratic panels on the design surface, the deviation from the exact derivative is less than 0.002%. The deviation from the brute-force derivatives is considerably higher (0.3%) for Case 3.

9.2 Summary of Results

The results demonstrate a satisfactory correspondence between the finite-difference derivatives and the continuous adjoint sensitivities for the Helmholtz equation.

The conclusion with regard to the deployment of the natural coordinates for ridding the analysis from normal derivatives in the final sensitivity expression and its impact on the accuracy of design derivatives is the most notable achievement of this chapter. Acquiring accurate and efficient gradient information is the most crucial element for any gradient-based optimization process to be practical. In Baysal *et al.* (1999) and Baysal and Kelly (1999), the finite-difference sensitivities of the Helmholtz equation are coupled with an optimization module to increase the acoustic effectiveness of a railroad barrier through reshaping the top surface of the barrier. Replacing the brute-force sensitivities with the present validated adjoint sensitivities of this chapter will result in a more efficient optimization process.

The author also believes that this experience can somehow help to pave the way for obtaining consistent sensitivities of the Navier-Stokes equations, where the first and second order derivatives of the state variables appear in the sensitivity integrals.

CHAPTER 10

Conclusions and Recommendations for Future Work

In this dissertation, the method of continuous adjoint sensitivity analysis has been applied successfully to the two-dimensional steady Euler equations, the unsteady transonic small disturbance equation (UTSD), and the Helmholtz equation. In the course of the analytical and computational development of each of these problems, new ideas and improvements on the existing methodologies have been discussed and demonstrated. In the following, a summary of the achievements and conclusions pertaining to each of the above-mentioned problems is presented

10.1 Sensitivities of the Two-dimensional Steady Euler Equations

In this work, the sensitivities of the steady Euler equations associated with a general cost functional that can be a function of pressure, density, and tangential velocity on the airfoil surface has been derived analytically. Generalization of the airfoil surface boundary condition of the adjoint set of equations to allow a proper closure of the Lagrangian functional is one of the first attempts to address this specific problem. The demonstrated results for an inverse problem with density as the prescribed target is the first of its kind in the current literature. In the numerical aspect of the work, it has been shown that for second order accurate schemes on a cell-centered triangular mesh, boundary derivative information can be accurately obtained to the s-n coordinate system.

The transformation to the natural coordinate system in conjunction with the reduction of the governing state equation to the control surface results in sensitivity integrals that are only a function of the tangential derivatives of the state variables. These tangential derivatives can be computed very accurately with cubic spline fitting of the available information on the surface and furthermore, this approach eliminates the need for normal derivative computations that can be erroneous.

With regard to computational storage, the continuous adjoint approach primarily uses allocated space of the CFD module and in this sense, it is much more economical than the discrete sensitivity approach. Furthermore, the gradient of the cost functional with respect to the array of design variables is computed within the cost of two state equation solutions, almost independent of the number of design parameters.

10.2 Limit-Cycle Sensitivities of the UTSD Equation

In this part of the work, the continuous adjoint methodolgy is extended to unsteady flows. It is demonstrated that for periodic airfoil oscillations that lead to a limit-cycle behavior at large times, the Lagrangian functional can only be closed if the time interval of interest spans one or more periods of the flow oscillations after the limit cycle has been attained. Consequently, a new time-accurate algorithm is developed for the UTSD equation and its adjoint equation and the steady state and limit-cycle sensitivities are derived by the continuous adjoint method and validated by comparing them with those obtained by using the brute-force finite difference approach. The analytical work of Chapter 7 for the UTSD equation and the computational results for limit-cycle sensitivities of Chapter 8 are the first of their kind in the field.

Furthermore, the importance of accounting for the variation of the flow circulation, appearing as a Dirac delta in the wall boundary condition at the trailing edge, is emphasized and demonstrated. It has been shown that the proper closure of the Lagrangian necessitates the inclusion of the Dirac Delta term, and it has a great impact on the accuracy of the obtained sensitivities.

It is remarkable that the cost of an unsteady adjoint solution is about 0.2 times that of a state equation solution, which demonstrates the advantage of the continuous adjoint method over the brute force method. It should be noted, however, that unsteady optimization requires the history of the flow variables within a full period of the flow oscillation. This can potentially be impractical for higher-fidelity physical models of the flowfield.

10.3 Sensitivities of the Helmholtz Equation

The starting point of this work is the wave equation in two-dimensions that is reduced to an elliptic Helmholtz equation by applying the method of normal modes. There is obviously a trade-off between solving for the unsteady wave equation in the real domain and the elliptic Helmholtz equation in the complex domain. The derivation of the adjoint system is straightforward but one needs to be careful with the choice of the fundamental solution for the adjoint set. From all the various feasible choices for the fundamental solution of the adjoint system, the clever choice is the one that satisfies the incoming wave behavior at the farfield identically. With any other choice for the fundamental solution, one has to use panels at the farfield and this increases the number of boundary unknowns dramatically.

The sensitivities of the Helmholtz equation require the gradient and the Hessian of the acoustic field in the Cartesian coordinate system. It has been shown that for curved surfaces, accurate Hessian computation is not an easy task and with a linear presentation of the curved surface, it is impossible to find directional derivatives having components along the normal to the surface direction (Babuska paradox). However, obtaining the Hessian by differentiating the discretization directly for a quadratic representation of the curved boundary is quite cumbersome, because of the need for finite-part computations of highly singular integrals, and it has not been attempted in this work. Nevertheless, it has been demonstrated that in the s-n coordinates the only derivative information needed are the first and second order tangential derivatives. These derivatives can be easily computed by fitting the boundary information with the cubic-spline interpolating function. It should be noted that it is of utmost importance that all integrations are done adaptively to capture the curvature variation along the control surface.

10.4 Recommendations for Future Work

Based on the experience gained in this work with the steady Euler equations, the extension to the Navier-Stokes equations remains to be investigated. Anderson and Venkatakrishnan (1997) abandoned the continuous approach in favor of the discrete sensitivity analysis, arguing that the accurate and consistent acquirement of second order derivative information on the control surface necessitates a higher order discretization of the flowfield, possibly third or fourth order accurate schemes. The experience gained in the work done on the Helmholtz sensitivities, which also requires the Hessian of the state variable, suggests that a similar transformation to the s-n coordinates in two dimensions

or the *s-n-b* system in three dimensions may ease the problem associated with the acquisition of accurate boundary derivative information.

Extension of the work on UTSD limit-cycle sensitivities to the Euler equations and transient sensitivities of unsteady state equations remains to be investigated. As these problems require the full flow history within a time interval of interest, computer storage and run-time problems may render the problem impractical.

Another open issue that needs further investigation is the level of coupling between the state, adjoint, optimization, and surface parameterization modules required for the minimization of the whole optimization cycle. Flow control and error estimation analysis with the aid of adjoint equations are among several newly emerging fields that the continuous adjoint methodolgy can be applied to directly.

REFERENCES

(In Alphabetical Order)

Angrand, F., (1983), "Optimum Design for Potential Flows," *International Journal for Numerical Methods in Fluids*, Vol. 3, pp. 265-282.

Anderson, W. K., and Venkatakrishnan, V., (1997), "Aerodynamic Design Optimization on Unstructured Grids with a Continuous Adjoint Formulation," NASA/CR-97-201650 ICASE Report No. 97-9, NASA Langley Research Center, Hampton, VA.

Anderson, W. K., and Bonhaus, D. L., (1997), "Aerodynamic Design on Unstructured Grids for Turbulent Flows," NASA Technical Memorandum, No. 112867, NASA Langley Research Center, Hampton, VA.

Arian, E., and Salas, M. D., (1997), "Admitting the Inadmissible: Adjoint Formulation for Incomplete Cost Functionals in Aerodynamic Optimization" NASA/CR-97-206269 ICASE Report No. 97-69, NASA Langley Research Center, Hamptom, VA.

Arian, E., and Ta'asan, S., (1994), "Multigrid One Shot Methods for Optimal Control Problems: Infinite Dimensional Control," NASA/CR-94-194939 ICASE Report No. 94-52, NASA Langley Research Center, Hamptom, VA.

Arslan, A. E., and Carlson, L. A., (1994), "Integrated Determination of Sensitivity Derivatives for an Aeroelastic Transonic Wing," AIAA Paper 94-4400.

Balakumar, P., and Hall, P., (1996), "Optimum Suction Distribution for Transition Control," AIAA Paper 96-1950, 27th AIAA Fluid Dynamics Conference, New Orleans, LA.

Banks, H. T., (1992), <u>Control and Estimation in Distributed Parameter Systems</u>, SIAM Frontiers in Applied Mechanics, Vol. 11.

Batina, J. T., (1988), "Efficient Algorithm for Solution of the Unsteady Transonic Small-Disturbance Equation," *Journal of Aircraft*, Vol. 25, No. 7, pp. 598-605.

Baysal, O., and Eleshaky, M. E., (1991), "Aerodynamic Sensitivity Analysis Methods for the Compressible Euler Equations," *Journal of Fluids Engineering*, Vol. 113, No. 4, pp. 681-688.

Baysal, O., and Eleshaky, M. E., (1992), "Aerodynamic Design Optimization Using Sensitivity Analysis and Computational Fluid Dynamics," *AIAA Journal*, Vol. 30, No. 3, pp.718-725.

Baysal, O., Eleshaky, M. E., and Burgreen, G. W., (1993), "Aerodynamic Shape Optimization Using Sensitivity Analysis on Third-Order Euler Equations," *Journal of Aircraft*, Vol. 30, No. 6, pp. 953-961.

Baysal, O., Cordero, Y., and Pandya, M. J., (1997), "Improving Discrete-Sensitivity-Based Approach for Practical Design Optimization," <u>International Conference on Fluid Engineering</u>, Vol. 1, Centennial Grand Congress of Japanese Society of Mechanical Engineers, Tokyo, Japan, pp. 417-424.

Baysal, O., and Ghayour, K., (1998), "Continuous Adjoint Sensitivities for General Cost Functionals on Unstructured Meshes in Aerodynamic Shape Optimization," AIAA Paper 98-4904, <u>Proceedings of the 7th AIAA/USAF/NASA/ ISSMO Symposium on Multidisciplinary Analysis and Optimization</u>, St. Louis, MO, pp. 1483-1491.

Baysal, O., Idres, M., and Ghayour, K., (1999), "Noise Barrier for Light Rail System: Computational Modeling and Design Optimization," Technology Applications Center Report, Old Dominion University, Norfolk, VA.

Baysal, O., and Kelly, J. J., (1999), "Evaluation of Concrete Noise Barrier for Light Rail System: Insertion Loss from Acoustical Measurements," Technology Applications Center Report, Old Dominion University, Norfolk, VA.

Becker, R., and Rannacher, R., (1996), "Weighted a Posteriori Error Control in Finite Element Methods," Technical Report, Universitat Heidelberg, Preprint No. 96-1.

Beichang, H., Ghattas, O., and Antaki, J. F., (1997), "Computational Strategies for Shape Optimization of Time-Dependent Navier-Stokes Flows," Technical Report CMU-CML-97-102, Civil and Environmental Engineering, Carnegie Mellon University, Pittsburgh, PA.

Beux, F., and Dervieux, A., (1992), "Exact-Gradient Shape Optimization of a 2-D Euler Flow," *Finite Elements in Analysis and Design*, Vol. 12, pp. 281-302.

Bewley, T., and Moin, B., (1994), "Optimal Control of Turbulent Channel Flows," *Active Control of Vibration and Noise*, ASME DE-Vol. 75, pp. 221-227.

Bewley, T., Temam, R., and Ziane, M., (1997), "A General Framework for Robust Control in Fluids Mechanics," Annual Research Briefs, Center for Turbulence Research, pp. 299-316.

Bonnet, M., (1992), "Shape Identification Using Acoustic Measurements: A Numerical Investigation Using BIE and Shape Differentiation," IUTAM Symposium Tokyo/Japan 1992, Inverse problems in Engineering Mechanics, (Eds. M. Tanaka and H. Bui), pp. 191-200.

Burgreen, G. W., and Baysal, O., (1994), "Aerodynamic Shape Optimization Using Preconditioned Conjugate Gradient Methods," AIAA Journal, Vol. 32, No. 11, pp. 2145-2152.

Burkardt, J., and Gunzburger, M., (1995), "Sensitivity Discrepancy for Geometric Parameters," CFD for Design and Optimization (Ed. O. Baysal), ASME FED-Vol. 232, pp. 9-15.

Caughey, D. A., (1982), "The Computation of Transonic Potential Flows," Annual Review of Fluid Mechanics, Vol. 14, pp. 261-283.

Chandrasekhara, M. S., Wilder, M. C., and Carr, L. W., (1998), "Unsteady Stall Control Using Dynamically Deforming Airfoils," AIAA Journal, Vol. 36, No. 10, pp. 1792-1800.

Cliff, E. M., Heinkenschloss, M., and Shenoy, A. R., (1995), "An Optimal Control Problem for Flows with Discontinuities," ICAM Report 95-09-02, Interdisciplinary Center for Applied Mathematics, Virginia Polytechnic Institute and State University.

Elbanna, H. M., and Carlson, L. A., (1990), "Determination of Aerodynamic Sensitivity Coefficients Based on the Transonic Small Perturbation Formulation," Journal of Aircraft, Vol. 27, No. 6, pp. 507-515.

Elbanna, H. M., and Carlson, L. A., (1992), "Determination of Aerodynamic Sensitivity Coefficients on the Three-Dimensional Full Potential Equation," AIAA Paper 92-2670.

Eleshaky, M. E., and Baysal, O., (1993), "Airfoil Shape Optimization Using Sensitivity Analysis on Viscous Flow Equations," *Journal of Fluids Engineering*, Vol. 115, No. 1, pp. 75-84.

Eleshaky, M. E., and Baysal, O., (1994a), "Preconditioned Domain Decomposition Scheme for 3-D Aerodynamic Sensitivity Analysis," *AIAA Journal*, Vol. 32, No. 12, pp. 2489-2491.

Eleshaky, M. E., and Baysal, O., (1994b), "Aerodynamic Shape Optimization via Sensitivity Analysis on Decomposed Computational Domains," *Journal of Computers and Fluids*, Vol.23, No. 4, pp. 595-611.

Elliot, J. K., and Peraire, J., (1996), "Practical 3D Aerodynamic Design and Optimization Using Unstructured Meshes," AIAA Paper 96-4170, 6th AIAA/NASA/USAF Multidisciplinary Analysis & Optimization Symposium, Seattle, WA.

Elliot, J. K., and Peraire, J., (1997), "Aerodynamic Optimization on Unstructured Meshes with Viscous Effects," AIAA Paper 97-1849, 13th AIAA CFD Conference, Snowmass Village, CO.

Frank, P. D., and Shubin, G. R., (1992), "A comparison of Optimization-Based Approaches for a Model Computational Aerodynamics Design Problem," *Journal of Computational Physics*, Vol. 98, pp. 74-89.

Gad-el-Hak, M., (1996), "Modern Developments in Flow Control," ASME Applied Mechanics Review, Vol. 49, No. 7.

Ghayour, K., and Baysal, O., (1999), "Limit-Cycle Shape Optimization Using Time-Dependent Transonic Equation," AIAA Paper 99-3375, Proceedings of the 14th AIAA Computational Fluid Dynamics Conference, Vol. 2, pp. 1040-1048.

Ghayour, K., and Baysal, O., (2000), " Continuous Adjoint Sensitivities of the Helmholtz Equation for Acoustic Optimization," Paper No. 2000-0687, 39th AIAA Aerospace Sciences Meeting and Exhibition, Reno, NV.

Giles, M. B., and Pierce, N. A., (1997), "Adjoint equations in CFD: duality, boundary conditions and solution behavior," AIAA Paper No.97-1850.

Giles, M. B., and Pierce, N. A., (1999), "Improved Lift and Drag Estimates Using Adjoint Euler Equations," AIAA Paper No. 99-3293.

Goorjian, P. M., and Van Buskirk, R. D., (1985), " Second-Order Accurate Spatial Differencing for the Transonic Small-Disturbance Equation," *AIAA Journal*, Vol. 23, No. 11, pp. 1693-1699.

Gunzburger, M. D., (1995), Flow Control, The Institute for Mathematics and its Applications, Vol. 68, Springer-Verlag.

Haug, E. J., Choi, K. K., and Komov, V., (1986), Design Sensitivity Analysis of Structural Systems, Mathematics in Science and Engineering, Vol. 177, Academic Press, Florida, pp. 193-197.

Harris, P. J., (1992), "A boundary element method for the Helmholtz equation using finite part integration," *Computational Methods in Applied Mechanical Engineering*, Vol. 95, pp. 331-342.

Hiernaux, S., and Essers, J. A., (1999), "Aerodynamic Optimization Using Navier-Stokes Equations and Optimal Control Theory," AIAA Paper 99-3297, 14th AIAA CFD Conference, Norfolk, VA.

Ho., C. M., and Tai, Y. C., (1996), Review: MEMS and its application for flow control, *ASME Journal of Fluid Engineering*, Vol. 118.

Ho., C. M., and Tai, Y. C., (1998), "Micro-electro-mechanical systems (MEMS) and Fluid Flows," Annual Review of Fluid Mechanics, Vol. 30, pp. 579-612.

Iollo, A., and Salas, M. D., (1995), "Contribution to the Optimal Shape Design of Two-Dimensional Internal Flows with Embedded Shocks," NASA/CR 95-1955062 ICASE Report No. 95.20.

Ito, K., and Ravindran S. S., (1996), "A Reduced Order Model for Simulation and Control of Fluid Flows," CRSC-TR96-27, Center for Research in scientific Computation, Department of Mathematics, North Carolina State University.

Jameson, A., (1988), "Aerodynamic Design via Control Theory," *Journal of Scientific Computing*, Vol. 3, pp. 233-260.

Jameson, A., (1990), "Automatic Design of Transonic Airfoils to Reduce the Shock Induced Pressure Drag," MAE Report No. 1881, Princeton University, also

presented at the 31st Israel Annual Conference on Aviation and Aeronautics, February 21-22, 1990.

Jameson, A., (1994), "Optimum Aerodynamic Design via Boundary Control," Lectures at the Von Karman Institute (VKI), April 1994.

Johnson, C., and Rannacher, R., (1994), "On Error Control in CFD," Technical Report, Universitat Heidelberg, Preprint No. 94-13.

Jameson, A., Alonso, J. J., Reuther, J., Martinelli, L., and Vassberg, J. C., (1998), "Aerodynamic Shape Optimization Techniques Based on Control Theory," AIAA Paper 98-2638, 29th AIAA Fluid Dynamics Conference, Alburquerque, NM.

Joslin, R. D., Gunzburger, M. D., Nicolaides, R. A., Erlebacher, G., and Hussaini, M. Y., (1997), "Self-Contained Automated Methodology for Optimal Flow Control," *AIAA Journal*, Vol. 35, No. 5, pp. 816-824.

Kolonay, R. M., (1995), "Transonic Unsteady Aeroelastic Analysis for the Multidisciplinary Design Environment," AIAA Paper No. 95-1285.

Kolonay, R. M., (1996), "Unsteady Aeroelastic Optimization in the Transonic Regime," AIAA Paper 96-3983, 6th AIAA/NASA/ USAF Multidisciplinary Analysis & Optimization, Bellevue, WA.

Kreisselmeier, G., and Steinhauser, R., (1979), "Systematic Control Design by Optimizing a Vector Performance Index," <u>Proceedings of the IFAC Symposium on Computer Aided Design of Control Systems</u>, Zurich, Switzerland, pp. 113-117.

Kuruvila, S., Ta'asan, S., and Salas, M. D., (1994), "Airfoil Optimization by the One-Shot Method," AGARD-FDP-VKI Special Course on Optimum Design for Aerodynamics, AGARD Report 803, pp. 7.1-7.21.

Lagnese, J. E., Russell, D. L., and White L. W., (1995), Control and Optimal Design of Distributed Parameters Systems, The Institute for Mathematics and its Applications, Vol.70, Springer-Verlag.

Landon, R. H., (1982), "NACA 0012 Oscillatory and Transient Pitching," Data Set 3, Compendium of Unsteady Aerodynamic Measurements, AGARD Report 702.

Li, W. L., and Livne, E., (1995), "Analytical Sensitivities and Approximations in Supersonic and Subsonic Wing/Control Surface Unsteady Aerodynamics," AIAA Paper 95-1219, 36th AIAAASME/ASCE/AHS/ASC Structures, Structural Dynamics and Materials Conference, New Orleans, LA.

Lions, J. L., (1971), Optimal Control of Systems Governed by Partial Differential Equations, Springer-Verlag, New York.

Loncaric, J., (1998), "Optimal Control of Unsteady Stokes Flow Around a Cylinder and the Sensor/Actuator Placement Problem," NASA/CR–98-207680 ICASE Report 98-18.

Lorence, C. B., and Hall, K. C., (1994), "Sensitivity Analysis of Unsteady Aerodynamic Loads in Cascades," AIAA Paper 94-0064, 32nd Aerospace Sciences Meeting & Exhibition, Reno, NV.

Marco, N., and Beux, F., (1993), "Multilevel Optimization: Application to One-Shot Shape Optimization Design," INRIA Report No. 2068.

Marrocco, A., and Pironneau, O., (1978), "Optimum Design with Lagrangian Finite Elements: Design of an Electromagnet," *Journal of Computer Methods in Applied Mechanics and Engineering*, Vol. 15, pp. 277-308.

McMichael, J. M., (1996), "Progress and Prospects for Active Flow Control Using Microfabricated Electro-Mechanical Systems (MEMS)," AIAA Paper 96-0360.

Murman, E. M., and Cole, J. D., (1971) "Calculations of Plane Steady Transonic Flow," *AIAA Journal*, Vol. 9, No. 2, pp. 114-121.

Murthy, D. B., and Kaza, K .R. V., (1991), "Semi-analytical Technique for Sensitivity Analysis of Unsteady Aerodynamic Computations," *Journal of Aircraft*, Vol. 28, No. 8, pp. 481-488.

Newman, J. C., Anderson, W. K., and Whitfield, D. L., (1998), "Multidisciplinary Sensitivity Derivatives Using Complex Variables," MSSU-COE-ERC-98-08, Computational Fluid Dynamics Laboratory, NSF Engineering Research Center for Computational Field Simulation, Mississippi State University, MS.

Nielson, E. J., and Anderson, W. K., (1998), "Aerodynamic Design Optimization on Unstructured Meshes Using the Navier-Stokes Equations," AIAA Paper 98-4809.

Pandya, M. J., and Baysal, O. (1997a), "Gradient-Based Aerodynamic Shape Optimization Using Alternating Direction Implicit Method," *Journal of Aircraft*, Vol. 34, No. 3.

Pandya, M. J., and Baysal, O., (1997b), "3D Viscous ADI Algorithm and Strategies for Shape Optimization," AIAA Paper 97-1853, June-July 1997.

Peraire, J., (1997), "Aeroelastic Computations in the Time Domain Using Unstructured Meshes," *International Journal of Numerical Methods in Engineering*, Vol. 40, pp. 2413-2431.

Piacentini, A., Invernizzi, M., and Pannese, L., (1996), "Computational acoustics: noise reduction via diffraction by barriers with different geometries," *Computational Methods in Applied Mechanical Engineering*, Vol. 130, pp. 81-91.

Pironneau, O., (1994), "Optimal Shape Design for Aerodynamics," Lectures at the Von Karman Institute (VKI), Rhodes Saint-Genese, Belgium.

Ravindran, S. S., (1995), " Electromagnetic Control for Fluid Flows,"CRSC-TR95-30, Center for Research in scientific Computation, Department of Mathematics, North Carolina State University.

Reuther, J., and Jameson, A., (1994), "Control Theory Based Airfoil design for Potential Flow and a Finite Volume Discretization," AIAA Paper 94-0499, 32nd Aerospace Sciences Meeting & Exhibitions, Reno, NV.

Saad, Y., and Schultz, M. H., (1986), "GMRES: A Generalized Minimum Residual Algorithm for Solving Nonsymmetric Linear Systems," *SIAM Journal of Scientific and Statistical Computing*, Vol. 7, No. 3, pp. 856-869.

Shenoy, A., Heinkenschloss, M., and Cliff, E. M., (1997), "Airfoil Design by an All-At-Once Method," TR97-17, Department of Computational and Applied Mathematics, Rice University.

Soemarwoto, B., (1997), "The Variational Method for Aerodynamic Optimization Using the Navier-Stokes Equations," NASA/CR-97-206277 ICASE Report No. 97-71.

Sorensen, T. M., and Drela, M., (1995), "Aeroelastic Sensitivity Calculations Using a Newton-Based Full-Potential Equation Solver," AIAA Paper 95-1834

Sritharan, S. S., (1998), Optimal Control of Viscous Flows, SIAM Publication.

Strang, G., and Fix, G. J., (1973), An analysis for the Finite Element Method, pp. 60-64, Prentice-Hall, Englewood Cliffs, New Jersey.

Ta'asan, S., Kuruvila, G., and Salas, M. D., (1992), "Aerodynamic Design and Optimization in One Shot," AIAA Paper 92-0025, 30th Aerospace Sciences Meeting & Exhibitions, Reno, NV.

Tang, K. Y., Graham, W. R., and Peraire, J., (1996), "Active Flow Control Using a reduced Order Model and Optimum Control," AIAA Paper 96-1946.

Venditti, D. A., and Darmofal, D. L., (1999), "A Multilevel Error Estimation and Grid Adaptive Strategy for Improving the Accuracy of Integral Outputs," AIAA Paper 99-3292.

Wrenn, G. A., (1989), "An Indirect Method for Numerical Optimization Using the Kreisselmeier-Steinhauser Function," NASA CR-4220.

APPENDIX A

Starting from

$$I_R = \int_\Omega \left(\frac{\partial \bar{F}^T}{\partial x} + \frac{\partial \bar{G}^T}{\partial y} \right) \cdot \bar{\lambda} d\Omega + \int_{\Gamma_r} \psi (\rho \bar{q} \cdot \hat{n}) ds \qquad (A.1)$$

and using Eqs. (3.4) and (3.9), one can easily arrive at the following expression for the design derivative of I_R.

$$I_R = \int_\Omega \left(\frac{\partial \bar{F}'^T}{\partial x} + \frac{\partial \bar{G}'^T}{\partial y} \right) \cdot \bar{\lambda} d\Omega + \int_\Gamma \left(\frac{\partial \bar{F}^T}{\partial x} + \frac{\partial \bar{G}^T}{\partial y} \right) (\vec{V} \cdot \hat{n}) ds$$

$$+ \int_{\Gamma_s} \psi \left(\rho \bar{q} \cdot \dot{\hat{n}} + \left((\rho \bar{q})' + \vec{V} \cdot \nabla (\rho \bar{q}) \right) \cdot \hat{n} \right) ds + \int_{\Gamma_s} \psi (\rho \bar{q} \cdot \hat{n}) \left(\frac{\partial v_t}{\partial s} - \frac{v_n}{R} \right) ds \qquad (A.2)$$

The second integral is identically zero because the governing Euler equations are satisfied on the boundary Γ and the fourth integral vanishes because of the wall boundary condition on Γ_s. Hence, Eq. (A.2) reduces to

$$I_R = \int_\Omega \left(\frac{\partial \bar{F}'^T}{\partial x} + \frac{\partial \bar{G}'^T}{\partial y} \right) \cdot \bar{\lambda} d\Omega + \int_{\Gamma_s} \psi \left(\rho \bar{q} \cdot \dot{\hat{n}} + \left((\rho \bar{q})' + \vec{V} \cdot \nabla (\rho \bar{q}) \right) \cdot \hat{n} \right) ds. \qquad (A.3)$$

Now, the first integral appearing in Eq. (A.3) can be rewritten as follows:

$$\int_\Omega \left(\frac{\partial \bar{F}'^T}{\partial x} + \frac{\partial \bar{G}'^T}{\partial y} \right) \cdot \bar{\lambda} d\Omega = \int_\Omega \left(\frac{\partial}{\partial x} \left(\bar{F}'^T \cdot \bar{\lambda} \right) + \frac{\partial}{\partial y} \left(\bar{G}'^T \cdot \bar{\lambda} \right) - \bar{F}'^T \cdot \frac{\partial \bar{\lambda}}{\partial x} - \bar{G}'^T \cdot \frac{\partial \bar{\lambda}}{\partial y} \right) d\Omega \qquad (A.4)$$

The fluxes, F and G, are functions of the state variable, $\bar{Q}$, and their local design variations can be written as

$$\bar{F}'^T = \bar{Q}' \cdot A^T$$
$$\bar{G}'^T = \bar{Q}' \cdot B^T \qquad (A.5)$$

using the chain rule. In Eq. (A.5) the flux Jacobians A and B are defined as:

$$A \equiv \frac{\partial \vec{F}}{\partial \vec{Q}} \quad , \quad B \equiv \frac{\partial \vec{G}}{\partial \vec{Q}} \tag{A.6}$$

Using the Gauss' theorem, the complete differentials present in Eq. (A.4) are written in terms of boundary integrals. Hence, Eq. (A.4) reduces to

$$\int_{\Omega} \left(\frac{\partial \vec{F}'^T}{\partial x} + \frac{\partial \vec{G}'^T}{\partial y} \right) \cdot \vec{\lambda} d\Omega = \int_{\Gamma=\Gamma_s+\Gamma_O} \left(n_x \vec{F}' + n_y \vec{G}' \right)^T \cdot \vec{\lambda} ds - \int_{\Omega} \left(\vec{F}'^T \cdot \frac{\partial \vec{\lambda}}{\partial x} + \vec{G}'^T \cdot \frac{\partial \vec{\lambda}}{\partial y} \right) \tag{A.7}$$

Upon using Eq. (A.5) in Eq. (A.7), and then in Eq. (A.3), the following is obtained

$$\begin{aligned}
i_R = &-\int_{\Omega} Q'^T \left(A^T \cdot \vec{\lambda}_x + B^T \cdot \vec{\lambda}_y \right) d\Omega \\
&+ \int_{\Gamma=\Gamma_s+\Gamma_O} \left(n_x \vec{F}' + n_y \vec{G}' \right)^T \cdot \vec{\lambda} ds + \int_{\Gamma_s} \psi \left((\rho \vec{q})' \cdot \hat{n} + \rho \vec{q} \cdot \dot{\hat{n}} + (\vec{V} \cdot \nabla (\rho \vec{q})) \cdot \hat{n} \right) ds
\end{aligned} \tag{A.8}$$

Eq. (A.8) is Eq. (4.10) of the main text.

VITA

Kaveh Ghayour was born in Tehran, Iran, on January 1, 1968. After finishing high school in 1985, he entered the Civil and Structural Engineering Department of Sharif Institute of Technology, Tehran, Iran. In 1988, he left Iran due to the ongoing war between Iran and Iraq. In 1990, he resumed his studies in England and managed to finish his BEng. and MSc. degrees in Aeronautical Engineering from Imperial College of Science and Technology, London, UK, in 1994. In 1996, he joined the PhD program of the Aerospace Engineering Department of Old Dominion University, Norfolk, VA and finished his doctorate in 1999.